The CFD simulation of an axial flow fan

by

Frederick Nicolaas le Roux

Master of Science in Mechanical Engineering

Thesis presented in partial fulfilment of the requirements for the degree of Master of Science in Mechanical Engineering at Stellenbosch University

Department of Mechanical and Mechatronic Engineering,
University of Stellenbosch,
Private Bag X1, Matieland 7602, South Africa.

Supervisor:	Mr. S.J. van der Spuy
Co-supervisor:	Prof. T.W. von Backström

March 2010

Declaration

By submitting this thesis electronically, I declare that the entirety of the work contained therein is my own, original work, that I am the owner of the copyright thereof (unless to the extent explicitly otherwise stated) and that I have not previously in its entirety or in part submitted it for obtaining any qualification.

Signature: .....
F.N. le Roux

Date: .....

Copyright © 2010 Stellenbosch University
All rights reserved.

Abstract

The CFD simulation of an axial flow fan

F.N. le Roux

Department of Mechanical and Mechatronic Engineering,
University of Stellenbosch,
Private Bag X1, Matieland 7602, South Africa.

Thesis: MScEng (Mech)

March 2010

The purpose of this project is to investigate the method and accuracy of simulating axial flow fans with three-dimensional axisymmetric CFD models. Two models are evaluated and compared with experimental fan data. Verification data is obtained from a prototype fan tested in a facility conforming to the BS 848 standards. The flow field over the blade surfaces is investigated further with a visualization experiment comprising of a stroboscope and wool tufts. Good correlation is found at medium to high flow rates and recommendations are made for simulation at lower flow rates as well as test guidelines at the fan test facility. The results and knowledge gained will be used to amend currently used actuator disc theory for axial flow fan simulation.

Key words: CFD, NUMECA, axial flow fan, flow visualization

Uittreksel

Die BVD simulasie van 'n aksiaalwaaier

("The CFD simulation of an axial flow fan")

F.N. le Roux

Departement Meganiese en Megatroniese Ingenieurswese,
Universiteit van Stellenbosch,
Privaatsak X1, Matieland 7602, Suid Afrika.

Tesis: MScIng (Meg)

Maart 2010

Die doel van hierdie projek is om die metode en akkuraatheid om aksiaalvloeiwaaiers met drie-dimensionele BVM modelle te simuleer, te ondersoek. Twee modelle word geëvalueer en met eksperimentele waaiertoetse vergelyk. Verifikasie data is verkry vanaf 'n prototipe waaier wat in 'n fasiliteit getoets is en wat aan die BS 848 standaarde voldoen. Die vloeiveld oor die lemoppervlaktes word ondersoek met 'n visualisering eksperiment wat uit 'n stroboskoop en wolletjies bestaan. Goeie korrelasie word gevind vir medium tot hoë massavloeie en aanbevelings word gemaak vir die simulasie by laer massavloeie met riglyne vir toetswerk in die toets-fasiliteit. Die resultate en kennis opgedoen sal gebruik word in die verbetering van huidige aksieskyfteorie vir numeriese aksiaalvloeiwaaier simulasies.

Sleutelwoorde: BVM, NUMECA, aksiaalvloeiwaaier, vloei visualisering.

Acknowledgements

I would like to express my sincere gratitude to the following people and organisations:

- My two supervisors for their continued support and guidance throughout the duration of the project. Thank you Mr. SJ van der Spuy for your motivation and encouragement in tiring times.

- Fluxion for their financial support.

- My family for continually pushing me and giving me the determination to finish.

- My friends for their motivation, in particular Andrew de Wet. Thank you for joining me on this journey.

- And finally my Lord the Saviour, without whom this and every achievement in my life would not be possible.

Dedications

This thesis is dedicated to my parents, for their perpetual love.

Contents

List of Figures

List of Tables

Nomenclature

Symbols

A	Cross-sectional area
b	Width
C_p	Specific heat at constant pressure
c_{b1}, etc	Empirical constants for turbulence model
D	Drag force
d	Diameter
E	Energy
e	Effectiveness
F	Force
h	Height
K	Thermal conductivity
k	Turbulent kinetic energy
L	Length, or Lift force
M	Torque
$\dot{m}$	Massflow rate
N	Rotational speed
n	Number, normal
P	Power
p	Pressure
Q	Source term, Volumetric flow rate
q	Heat flux vector
R	Universal gas constant
r	Radius
S	Magnitude of vorticity
$\tilde{S}, g, r_{sp}$	Intermediate variables for turbulence model
S_{ij}	Strain-rate tensor
T	Temperature
t	Axial thickness of the actuator disk model, time

U	Freestream velocity
u, v, w	Velocity components
u_i	Fluctuating velocity components
V	Volume
$\mathbf{v}$	Velocity vector
x, y, z	Cartesian coordinates
α	Angle of attack
β	Relative flow angle
χ	Intermediate variable for turbulence model
Δ	Differential
δ	Incremental
δ_{ij}	Kronecker delta
η	Efficiency
γ	Specific-heat ratio (C_p/C_v), Blade angle
κ	Kármán constant
μ	Viscosity
ν	Kinematic molecular viscosity
$\tilde{\nu}$	Working variable for turbulence model
ω	Angular rotation speed
ϕ	Blade setting angle
π	$= 3.141\,592\,654$
ψ	Momentum source term
ρ	Density
σ	Blade solidity, constant for turbulence model
τ	Boundary-layer shear stress
τ_{ij}	Stress tensor
ξ	Stagger angle
ε	Turbulent dissipation

Superscripts

r	Distance from axis of rotation
$+$	Law-of-the-wall variable
TM	Trademark

Subscripts

amb	Ambient
b	Blade

$bell$	Bellmouth
c	Chord
D	Drag
d	Dynamic
e	External
F	Fan
h	Hydraulic
I	Inviscid
i	Numeral index, 1,2,3...
L	Lift
m	Meridional direction
p	Pressure
w	Wall
R	Relative
r	Radial direction
ref	Reference
S	Surface
s	Static
$setl$	Settling chamber
t	Turbulent
tot	Total
V	Viscous
z	Axial direction
θ	Tangential direction
τ	Friction
1	First inner cell

Auxiliary Symbols

$'$	Fan-law scaled variable, turbulent fluctuation
$\bar{}$	Time-mean
$\vec{}$	Vector

Dimensionless Groups

$\alpha\varepsilon$	Compound calibration constant
Re	Reynolds number
C_f	Skin-friction coefficient

Acronyms

ADM	Actuator Disk Model
AGS	Abu-Ghannam and Shaw
ACHE	Air-Cooled Heat Exchanger
ACSC	Air-Cooled Steam Condenser
CFD	Computational Fluid Dynamics
CFL	Courant-Friedrichs-Levy
GUI	Graphical User Interface
MAX	Maximum
MPA	Mixing plane approach
PJM	Pressure jump method
RES	Residual
RMS	Root mean square
USB	Universal serial bus

Chapter 1

Introduction

Axial flow fans have a wide range of application in industry. Direct cooling of Air Cooled Heat Exchangers (ACHE) in the form of fan arrays is one of the largest industrial axial flow fan applications with appropriate large saving possibilities in terms of improving fan efficiencies. To illustrate this point, consider one of the world's largest forced draft dry-cooled power plants, the Matimba power plant, located in South Africa (Figure 1.1). The power plant consists of $6 \times 665\,\text{MW(e)}$ Air Cooled Steam Condenser (ACSC) units, each unit employing 48 heat exchangers (six rows of eight fans). That amounts to 288 axial flow fans, 9.145 m in diameter, each driven through a reduction gearbox by a 270 kW electrical motor (Kröger (1998) and Bredell (2005)). With fossil fuels diminishing, increasing popularity of alternative (or renewable) power generation and a constant growth in national power demand, large scale electricity savings at such power plants becomes increasingly more important. "An appropriate and well-designed cooling system can have a very significant positive impact on plant profitability" (Kröger, 1998). A rough estimation (neglecting distorted inflow conditions resulting in different fan performance from fans at the edge of the array) indicates that improving a single axial flow fan's efficiency by 5 % relates to a total power saving for the 288 fans of 5.6 MW.

Although water is a more appropriate heat sink than air, in arid regions (such as the Limpopo province of South Africa where the Matimba plant is situated) the use of air-cooled or dry-cooled systems in power plants is justified where cooling water may be insufficient and very expensive or not available at all (Kröger, 1998). The Matimba power generation plant uses single pass, forced draught ACHE's in the configuration displayed in Figure 1.2. In comparison to an induced draught ACHE (with the fan located above the heat exchanger bundle), the forced draught ACHE has the advantage of consuming less power for a given air mass flow rate since it pumps cooler air with a higher density. Since the forced draught ACHE's fan drives are located beneath the heat exchangers, they are more easily maintained and are not subjected to high air flow temperatures, allowing simpler materials for construction and a

Figure 1.1: The Matimba direct dry-cooled power plant (www.eskom.co.za).

longer fan drive lifespan. As shown in Figure 1.2, the turbine exhaust steam is piped directly to the ACSC unit where heat is rejected to the environment by means of air flow through the finned tube heat exchanger. The finned tubes are arranged in an A-frame or delta configuration in order to drain the condensate effectively, reduce the plot area of the ACSC units and reduce the duct lengths distributing the process fluid to the ACSC units. The dynamic interaction between the steam turbines and the ACSC, the difference between ambient drybulb temperature and the finned tube temperature and the flow rate delivered by the axial flow fans directly influence the efficiency of a typical air-cooled power plant (Bredell, 2005). Therefore any axial flow fan performance reducing effects should be taken under careful consideration when optimizing the efficiency of a direct air-cooled power generation plant.

One of the performance reducing effects on axial flow fan units within an ACSC is distorted inflow to the fan units. This topic has been investigated in numerous studies (Venter (1990), Thiart and von Backström (1993), Stinnes (1998) and Bredell (2005)). Causes for inlet flow distortion are the proximity to structures (turbine house, ground surface), induced cross-drafts from adjacent fans and prevailing winds surrounding the fan array. All of these factors have to be taken into account when designing an ACSC. However, since these factors vary from one fan unit to the next depending on the location within the ACSC and relative to other fan units within the fan array, it is necessary

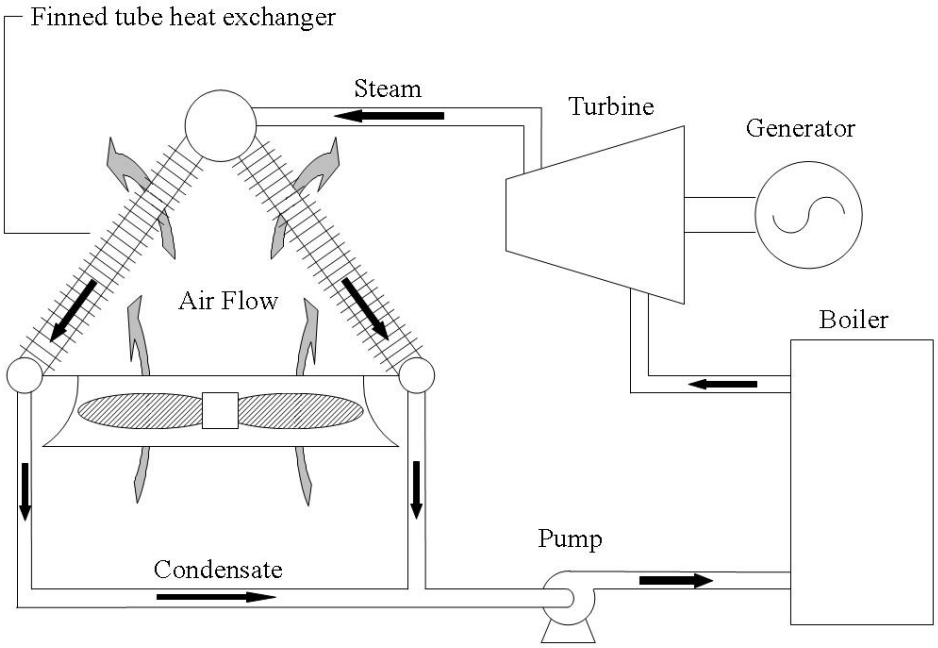

Figure 1.2: Direct air-cooled condensing system with A-frame heat exchanger configuration.

to broaden the individual fan investigation to incorporate the whole fan array. A very efficient way of investigating the design factors for such an ACSC is by means of a Computational Fluid Dynamic (CFD) analysis of the complete system. Unfortunately using a full three-dimensional computational domain becomes computationally expensive, especially if discrete fan models are used in the system.

To simplify the numerical modelling of an axial flow fan, different models have been developed, such as the constant velocity fan model, constant static pressure fan model, varying static pressure fan model and the actuator disc model (ADM) (Bredell, 2005). The latter model was extensively used in CFD analyses by Thiart and von Backström (1993), Meyer (2000) and Bredell (2005). Unfortunately the model under-predicts the fan's performance at flow rates less than the fan stalling flow rate. Another draw-back of the model is the large database that it requires, containing the airfoil characteristics over a wide range of angles of attack, Reynolds numbers and Mach numbers (Ohad and Aviv, 2005). In order to improve the model's ability to cover the complete operating range of the axial flow fan, an investigation is launched to model the fan with a full discrete model incorporating rotating solid surfaces. Bredell (2005) recommends a full three-dimensional modelling approach for "effective

and realistic modelling of wind-effects", and mentions the use of improved fan blade lift and drag characteristics and including the modelling of radial forces in the ADM, as possible areas of improvement.

This thesis is motivated by the hypotheses that a detailed investigation of the flow field around the blades of an axial flow fan, in a geometrically correct setup, incorporating the radial flow effects due to centrifugal forces present on the blade, will provide more accurate lift and drag coefficients for implementation in the ADM. The lift and drag coefficients in the ADM, used by Meyer (2000) and Bredell (2005), are verified only to empirical data from two-dimensional flow experiments, where this dissertation takes a three-dimensional approach.

To ensure that realistic flow conditions are enforced on the rotating blades, the CFD model should resemble a test facility used for characterising fan performance. Such a facility currently exists at Stellenbosch University and conforms to the British Standards test codes (BS 848 standards, 1980). This facility has been extensively used for testing scale model fans utilized in air-cooled power plants (Venter (1990), Bruneau (1994) and Stinnes (1998)).

The B2-fan rotor analysed in this thesis, was designed by Bruneau (1994), and used in investigations by Stinnes (1998), Meyer (2000) and Bredell (2005). It is a $\frac{1}{6}^{th}$ scale prototype model of a typical fan unit in an air-cooled power plant with a hub-to-tip ratio of 0.4. The B2-fan was selected for the CFD analysis because of the large amount of ADM analyses previously done on this fan by Meyer (2000) and Bredell (2005). To verify the integrity of the CFD results, the CFD results are compared with experimental data from the test facility. Unfortunately the original blades developed by Bruneau (1994) no longer exist and another experimental dataset had to be produced for the new set of blades manufactured form the original moulds.

The overall objective of this project would be a recommendation regarding the application and accuracy of CFD to model axial flow fans and to produce a fan performance dataset for the new B2-fan blades.

An outline of the thesis chapters and a brief discussion on each follows:

- Chapter 2 gives a literature review of previous work done in developing the ADM, and the design and utilisation of the fan test facility.

- Chapter 3 provides a detailed outline of the numerical techniques employed in developing a full three-dimensional CFD model. The simulation steps of grid generation, setting up various computational parame-

ters and post processing are discussed.

- Chapter 4 discusses the fan test facility, fan rotor setup, experimental procedure and results.

- Chapter 5 illustrates the validation of the CFD results with the experimental results. The flow visualisation experiment performed on the fan blades in the fan test facility is described and discussed.

- Chapter 6 renders a conclusion on developing a three-dimensional CFD model for amending the ADM and lists recommendations for future work.

Chapter 2

Literature survey

2.1 Introduction

The scope of this thesis is two-fold: Simulating an axial flow fan numerically using CFD code and verifying the accuracy of the numerical predictions with experimental results. The literature survey discusses the previous work done within these two fields and finishes off with a summary on the main findings.

2.1.1 Simulation of an axial flow fan

The ideal method with which to simulate an axial flow fan in CFD would be to use a fully discrete model. The amount of detail included in a CFD model is however limited by the capability of the computation resources. When simulating special cases like large ACSC's, a simpler CFD model is required that consumes less computational resources (Van Staden, 1996).

A number of previous projects have been done, using different simple CFD models to simulate an axial flow fan or propeller.

Pericleous and Patel (1986) developed a mathematical model for the simulation of tangential and axial agitators in chemical reactors. The different impellers were represented as a quadratic source of momentum in the tangential and/or axial directions (depending on the type of impeller); while the other geometries, such as the baffles, were represented as sinks of momentum. The lift and drag coefficients from experimental data of the blade cross-sectional airfoil profiles were used to calculate the blade forces. The momentum contributions from these forces were then introduced as appropriate momentum sources and sinks in the Navier-Stokes equations and solved using a control volume formulation. Good agreement was found, but the model showed some inadequacy in modelling turbulence.

Pelletier and Schetz (1986) and Schetz *et al.* (1988) investigated the three-dimensional flow in close vicinity of a propeller. This three-bladed propeller typically represents push-prop arrangements on aircraft. In this case the propeller was modelled as an actuator disk of thickness roughly equal to the physical thickness of the propeller. The thrust and torque were constant in the tangential direction, but allowed to vary radially. The three-dimensional, Reynolds-averaged, steady-state, Navier-Stokes equations were solved by a penalty function finite element method. Turbulence modelling was achieved through a generalization of an integrated turbulence-kinetic-energy model. The general-purpose finite element fluid dynamics program FIDAP was used to program the turbulence model. Good agreement was found in comparison with wind tunnel measurements for the prediction of velocity and pressure profiles along the radial axis.

Pelletier *et al.* (1991) developed a new model to compute the axisymmetric viscous throughflow past propellers. This was an effort to remove the limitations (of the previous numerical work on propellers) of relying on experimental values of thrust and torque to be introduced as momentum sources/sinks in the actuator disk. An analysis of the kinematics of the rotor provides the thrust, torque and power input to (or extracted from) the flow. Both a mixing and a penalty function finite element method were used to solve the time averaged Navier-Stokes equations. Turbulence was modelled by a simple mixing length equation and programmed by CADYF (a finite element based computer program for solving steady state, incompressible fluid flow problems). Again good agreement was found in comparison with wind tunnel measurements for the prediction of velocity and pressure.

Lötstedt (1992) developed a model for the computation of the time-averaged flow field produced by an aircraft propeller over a nacelle and wing. He used the panel method and a slip-stream model based on classical propeller theory. The panel method was amended to handle the vertical flow behind the rotating propeller and had the advantage of being easy to use and relatively computationally inexpensive. The time-averaged flow behind the propeller was generated by a system of vortices of which the strength was determined by combined momentum-blade element theory.

Later Lötstedt (1995) expanded this model for a full aircraft and replaced the propeller with an actuator disk. The blade forces were still approximated by combined momentum-blade element theory. Three simplifications were implemented to reduce the computational complexity: inviscid flow assumption, a thin propeller disk and using time-averaged variables. The unknown values at the disk, placed between two layers of cells in the grid, were extrapolated from the upstream and downstream cells adjacent to the disk. The calculations performed using the panel method were compared to a one-dimensional

Euler code and wind-tunnel experiments. The Euler solution provided better agreement with the wind-tunnel tests at higher Mach numbers, but required a much finer grid. The panel method was deemed faster and easier to use for subsonic flows, but Lötstedt (1995) preferred the Euler method due to its ability to capture the shape of the slipstream automatically.

Thiart and von Backström (1993) developed an actuator disk model for a low solidity/low hub-to-tip ratio axial flow fan. The Navier-Stokes equations were solved with the aid of a $k-\varepsilon$ turbulence model and the SIMPLEN method. The thrust forces and torque applied on the air flow by the fan blades were determined by blade element theory and the effect of distorted inflow conditions were investigated. Empirical correlations were used to determine the lift and drag coefficients of the blade elements. The method developed by Pericleous and Patel (1986) was followed, hence the lift and drag coefficients of the blade elements were used to calculate the lift and drag forces exerted by that specific element on the flow. These forces were then included in the Navier-Stokes equations as body forces. Good agreement with experiments were found but the increased power associated with distorted inflow conditions was under predicted.

Van Staden (1996) integrated a fan performance model into a CFD model for the performance prediction of a complete air-cooled condenser. Experimental fan performance curves were used to obtain the momentum source term of the fan in the axial direction, which was added to the Navier-Stokes equation as a source term in the CFD model. Good agreement was found with experimental data at ideal conditions, but for non-ideal conditions (such as distorted inflow) the model required the fan performance curves at these adverse conditions.

Meyer (2000) and Bredell (2005) utilized the actuator disk model of Thiart and von Backström (1993) for their numerical investigations of air-cooled heat exchangers. As mentioned in the introduction chapter, this model under-predicts the fan performance at low flow rates (see Figure 2.1). This can be attributed to the model only taking the axial and tangential velocity components into consideration for calculating the relative inflow vector, neglecting the radial component. The radial component of velocity and the Corriolis effect, associated with rotation, become more prominent at lower flow rates and induce a delay in boundary-layer separation that results in retarded stall (Ohad and Aviv (2005)).

Most of the literature involving axial flow fans/propellers/impellers revolve around stirred tanks, propeller propulsion (such as ships and helicopters) and wind turbines. The latter two cases differ from the work presented here since they involve air flow over unducted fan blades. No previous research in literature could be found for discrete simulation of ducted axial flow fans used

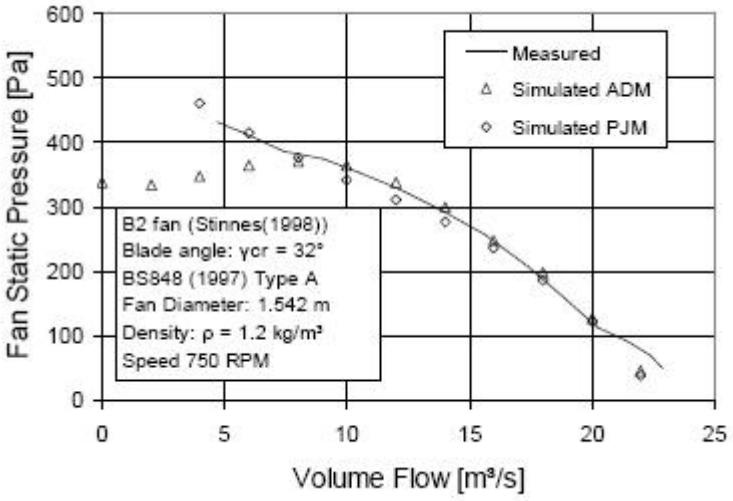

Figure 2.1: ADM compared to experimental data (Van der Spuy *et al.* (2009)).

in forced-draught heat exchangers. Based on the available literature it can be concluded that the ADM remains the preferred method for simulating the effect of an axial flow fan on air flow through ACSC's. The most recent work on the simulation of a stirred tank and one other case of ducted axial fan simulation is presented next.

A complete three-dimensional CFD model was used by Ramasubramanian *et al.* (2008) to analyse the fiber diffusion process in the manufacturing of wet-laid nonwovens. The three-bladed impeller and baffles were modelled in FLUENT™ by using the MIXSIM user interface and incorporating the multiple reference frame model. This meant that for the impeller a rotating reference frame was used and for the baffles and tank, a stationary reference frame was used. The impeller has a diameter of 0.2 m and rotates at 350 rpm. A standard $k - \varepsilon$ turbulence model was used for the flow solution. The simulation was compared to experimental work on a mixing tank with baffles and an impeller located in the center of the tank. The effect of a rectangular and triangular cross section on dispersion quality was predicted by the CFD model. The baffles in this application reduce the recirculating flow by effectively breaking up the large central vortices produced by the impeller. The authors found the model useful to predict the location, source and mechanism behind the formation rope and log defects.

Kelecy (2000) predicted the fan performance of a four-bladed axial flow propeller over a range of flow rates and compared the results with wind tunnel data. The blade has a rotational speed of 2000 rpm and a diameter of 0.11 m. The rotating reference frame method of FLUENT™ was used to simulate the

rotation of the $\frac{1}{4}^{th}$ axisymmetric fan model. The flow equations were solved in the rotating reference frame. A zero velocity was imposed on the blade surfaces and shaft, while the outer walls of the tunnel were rotated at the specified speed in the opposite direction when viewed from a stationary reference frame. He observed the sensitivity of the flow solutions to initial conditions, significant pressure gradients from the blades to the inlet at lower flow rates as well as radial outflow from the fan as the flow rate decreases.

2.1.2 Experimental

The accuracy of the CFD model is verified with experimental results. To ensure confidence in a set of experimental data, the data set needs to conform to certain air performance test methods (standards), in this case for industrial fans. These standards aim to provide a specified environment where the fans can be tested. When comparing different fan designs for a certain application, the fan test results all need to adhere to similar conditions, standardized setup and testing procedures to eliminate any uncertainties in the comparison. The fan test standards, extensively used at the low speed fan test facility at Stellenbosch University for previous work as well as in this dissertation, is the British Standards, BS 848 : Part 1 : 1980. The Type A standard installation type is used, with free inlet and outlet. The fan exhausts into open atmosphere. The characteristics required for fan performance set forth in the BS 848 standards 1980, are the fan static pressure rise, the fan power and fan static efficiency (a relation of the aforementioned two).

Venter (1990) designed the test facility according to the BS 848 standards 1980 for testing axial flow fans. The facility was used to investigate the performance of axial flow fans in ACSC's. He looked at the influence of flow distorting factors (such as support structures and heat exchanger configurations) and fan design parameters (such as blade tip clearance and hub plates) on the performance of a typical industrial cooling fan that he referred to as the V-fan.

From Venter (1990)'s research it became apparent that the V-fan suffered from a large amount of recirculating flow in the hub region. Bruneau (1994) set out to resolve this issue and improve on the efficiency, while maintaining the original fan pressure rise and volumetric flow rate, by designing two prototype fans with a higher hub-tip ratio than the V-fan. The B1-fan utilizes the Clark-Y aerofoil profile and the B2-fan incorporates the NASA LS series. Bruneau (1994) mentions that the choice of the NASA LS series blade profile was motivated by the particular profile's exceptional lift/drag characteristics, good off-design performance and its tolerance to inlet flow distortion. The blades were designed with the use of simple radial equilibrium equations. The two fans compared favourably with the fan from Venter (1990) over the entire fan operating envelope. The fan performance characteristics of the B2-fan with

the NASA LS series airfoil profile serves as reference data for the experimental work carried out in this thesis.

An incident occurred in which the V-fan was destroyed and it was replaced by Stinnes (1998) with the geometrically similar S-fan. Stinnes (1998) investigated the effect of a cross-flow component at the inlet on the performance of axial flow fans. For this he incorporated the prototype B1-fan and B2-fan of Bruneau (1994) along with the S-fan and in addition provided a thorough guideline for performing experimental tests on the test facility at Stellenbosch University. Furthermore he measured the flow field immediately up- and downstream of the fan with a 5-hole probe and developed a prediction model to predict local flow patterns for cases that where not examined with the 5-hole probe experiments. The method of the prediction model is similar to the actuator disc theory and takes fan blade and local flow patterns at various radial stations and circumferential positions into account to determine global fan performance.

Meyer (1996) experimentally investigated a number of component and geometrical changes to ACHE's in order to determine the effect of these changes on the ACHE performance characteristics. Two of the changes that are of particular interest were the use of different fan types and fan sizes, and the variation in the fan rotor axial position within the shroud. The necessity to investigate these two parameters led to another data set of fan performance characteristics for the B2-fan for possible use as reference regarding the experimental work within this thesis. Meyer (2000) also performed experimental verification of his axial flow fan model with the B2-fan designed by Bruneau (1994).

The fan test facility stood dormant for five years, after which it was recommissioned by Esterhuyze (2006). Unfortunately Esterhuyze (2006) had an incident where the original B2-fan was destroyed and a new set of blades from the same mould designed by Bruneau (1994) was manufactured by another student (Dippenaar, 2007).

The main fan rotor dimensions and set-up of the facility is shown in Figure 2.2. Changing the fan axis position (in an upstream direction) had no discernible effect on the fan performance characteristics (Meyer, 1996); therefore the fan axis position was kept constant throughout the experiments. The blade stagger angle (ξ) is set relative to the plane perpendicular to the axis of rotation (see Figure 2.3). To set the blades at a prescribed blade stagger angle, a blade setting angle (ϕ) was used in conjunction with a digital projector fixed onto a blade angle setting jig. The B2-fan specifications are given in Table 2.1 (Bruneau, 1994).

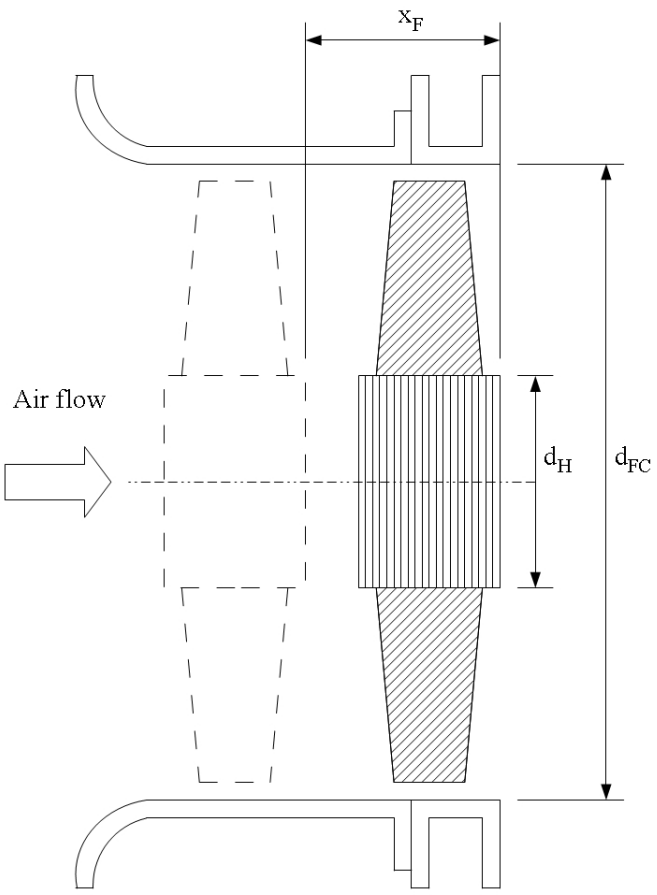

Figure 2.2: Main fan rotor dimensions and set-up, adapted from Meyer (1996).

Table 2.1: B2-fan specifications

Number of blades	8
Hub diameter (d_H) [m]	0.617
Fan casing diameter (d_{FC}) [m]	1.542
hub-tip ratio	0.4
Fan axis position (x_F) [m]	0
Tip clearance [mm]	3
Average chord length [m]	0.167

2.2 Summary of main findings

The ADM model provides a means to effectively simulate a complete ACHE consisting of multiple fan units, without using a discrete fan model. This ap-

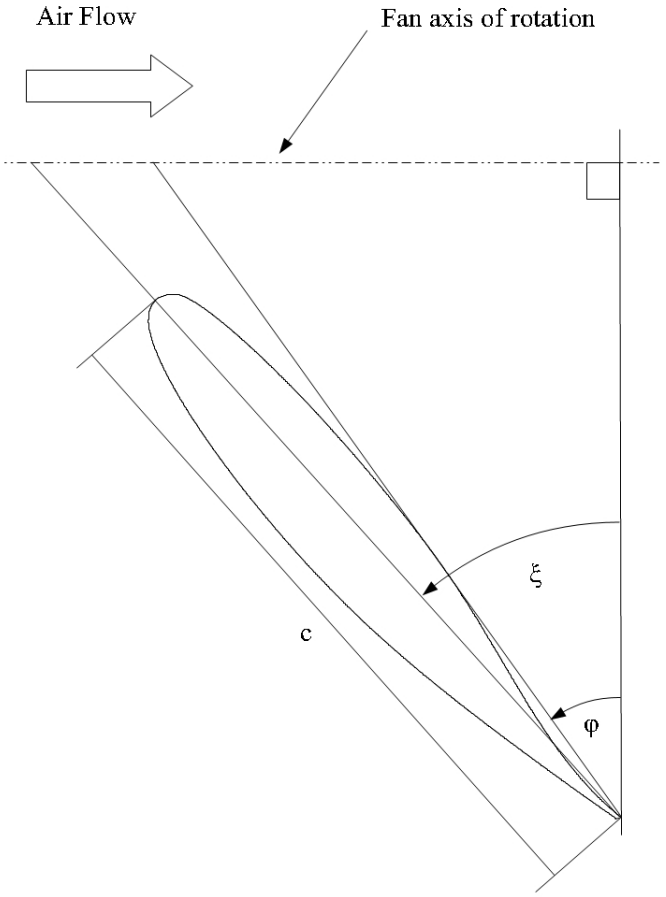

Figure 2.3: Blade stagger angle and blade setting angle.

proach saves computational grid complexity and computer processing power, resulting in reduced time required to obtain a solution. Unfortunately this model under-predicts the fan performance at very low flow rates (Ohad and Aviv (2005) and Van der Spuy *et al.* (2009)). This necessitates a detailed investigation of flow over the fan blade surfaces in order to amend the existing ADM model with the appropriate source terms. Although excellent experimental tests (in particular by Stinnes (1998)) were performed on the B2-fan in the past, replacement of the B2-fan blades warrants a new fan performance data set. The data from Stinnes (1998) did not include fan performance tests at 3 mm tip clearance as referenced by Bruneau (1994). The new fan performnce data set would include both tip clearances for reference with previous work.

Chapter 3

Numerical modelling

3.1 Introduction

The analysis of CFD problems generally involve three steps:

- Discretization of the flow domain
- Setting up and initiating the flow computation
- Visualizing the results

For these three steps NUMECA has developed three software systems. The discretization is performed in an **Auto**mated **Grid** generator for turbomachinery systems (AutoGrid™) and/or in an **I**nteractive **G**eometry modeller and **G**rid generation system for multiblock structured grids (IGG™). The second step is executed by the flow solver EURANUS (**EUR**opean **A**erodynamic **NU**merical **S**imulator), which is a three-dimensional multiblock flow solver that is able to simulate Euler or Navier-Stokes (laminar or turbulent) flows. The final step is performed with a highly interactive **C**omputational **F**ield **V**isualization software system (CFView™). All three software systems have been integrated into NUMECA's **F**low **IN**tegrated **E**nvironment (FINE™), which is a user friendly GUI, that operates on a project basis eliminating the need for file manipulation in the consolidation of the three steps. Detailed discussions of the three steps follow.

3.2 Fan blade data

All analyses were performed on what Bredell (2005) referred to as the B-fan. The B-fan is actually the B2-fan designed by Bruneau (1994). The reason for choosing the B2-fan is based on the availability of original design data for the fan. In order to compare a full three-dimensional CFD simulation of the axial flow fan to the experimental results, the same data for the blade profile

had to be used. Bruneau (1994) designed the blade with a linear decrease in blade thickness of 13 % (thickness/chord ratio) at the hub down to 9 % at the tip. To define the change in blade properties from hub to tip, the blade was divided into several two-dimensional sectional blade profiles at different radial stations. To calculate the blade profile co-ordinates the chord length and stagger angle at each radial station is needed. After scaling the chord length at the hub and tip radius, Bruneau (1994) used linear interpolation to determine the chord length at the intermediate radial stations. The stagger angle is determined from the difference between the inlet relative flow angle and the angle of attack. The angle of attack for each radial station was interpolated from a C-spline fitted through experimentally determined angle of attack versus lift coefficient data, for the particular airfoil profile used in the fan blade design. Figure A.1 in Appendix A shows the distribution of chord length and stagger angle radially across the blade length.

Bruneau (1994) used the General Aviation (Whitcomb)-number two (GA(W)-2) airfoil designed by McGhee *et al.* (1977), as a profile for the blades of the B2-fan. The GA(W)-2 is a 13 % thick airfoil derived from the 17 % thick GA(W)-1 airfoil originally designed for propeller driven light aircraft. The 13 % thick GA(W)-2 airfoil is obtained by linearly decreasing the mean thickness distribution of the 17 % thick GA(W)-1 airfoil with a ratio of $\frac{13}{17}$.

McGhee *et al.* (1977) produced an airfoil profile data set, as used by Bruneau (1994), of 39 points per surface. Using this data set rendered a coarse mesh, observed after generating the mesh in IGG™. Further investigation revealed that a whole family of airfoils emerged from the GA(W)-1 airfoil with a new designation, resulting in the GA(W)-1 airfoil becoming the LS(1)-0417 and the GA(W)-2 airfoil becoming the LS(1)-0413 airfoil. According to McGhee *et al.* (1979) the LS(1) designates low speed (first series); the first two digits specify the airfoil design lift coefficient in tenths, while the last two digits indicate the airfoil thickness in percent chord. McGhee *et al.* (1979) produced a finer airfoil profile data set of 45 points per surface. Figure A.2 displays a plot of the GA(W)-2 profile and the LS(1)-0413 profile from the different data sets.

Seven airfoil profile data sets were produced at different radial stations from the 45-point-per-surface data. These radial station blade co-ordinates were used in the mesh modelling by importing the data set into IGG™ and fitting a C-spline through the data. From this C-spline 200 data points per surface were exported to a data file for use in the three-dimensional blade generation process in AutoGrid™. Table A.1 displays the fan blade data set for the hub profile. A close-up view of the grid resolution at the blade leading edge is illustrated in Figure 3.1.

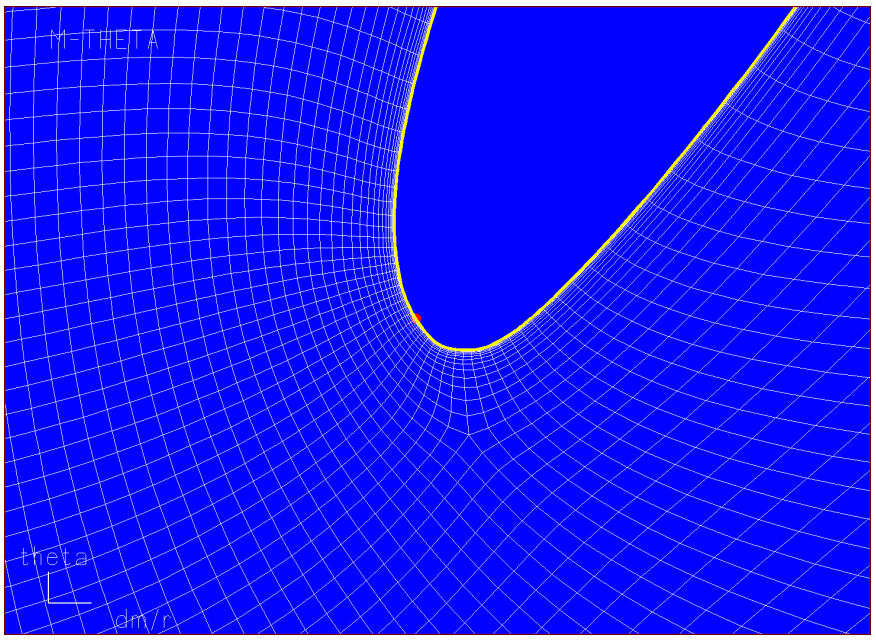

Figure 3.1: Leading edge grid point distribution.

3.3 Computational domain

A $\frac{1}{8}^{th}$ discrete three-dimensional computational grid for an axial flow fan was developed using a combination of the AutoGrid™ and IGG™ software from NUMECA. The AutoGrid™ software facilitates fully automated grid generation for turbomachinery blades, while the IGG™ software is a powerful structured grid generator. The model consists of three segments, namely the inlet, blade and outlet segments. Both the inlet and outlet segments were created in IGG™, while AutoGrid™ was used for creation of the more complex blade geometry. Once all three segments were completed separately, they were combined within AutoGrid™ with the use of three-dimensional technological effects to form a single model. Three-dimensional technological effects in AutoGrid™ include all effects defined by three-dimensional surfaces or three-dimensional curves whose meshes were created manually in IGG™. This single model was reopened in IGG™ for the final specification of the rotor-stator interface between the blade segment and the inlet segment on one side as well as the outlet segment on the other side.

3.3.1 AutoGrid™

The approach stipulated in the user manual (AutoGrid™ Manual, 2007a) was followed for semi-automatic three-dimensional blade generation. This included:

1. Definition of the geometry. This includes specification of the blade pro-

file surfaces from the imported data of Table A.1 in Appendix A, as well as specifying the hub and shroud surfaces of revolution. Additional information such as tip clearance (3 mm in this case) is also specified.

2. Generation of meridional flow paths. These paths act as meridional traces for the surfaces of revolution on which the three-dimensional mesh is built.

3. Generation and control of the two-dimensional mesh on the surfaces of revolution. This allows the manipulation of the mesh topology and grid clustering. The grid quality can be checked at different radial stations.

4. Generation of the final three-dimensional mesh. The three-dimensional mesh is generated by using conformal mapping between the three-dimensional Cartesian space and the two-dimensional meshes on the surfaces of revolution that follows the meridional flow paths.

The AutoGrid™ interface allows checking of the mesh quality at any level, radially between the hub and the shroud. The mesh quality is measured according to the following criteria:

- Orthogonality, the measure of the skewness of the cells and is determined by the minimum angle between the edges of the cell. It has a range of 0° to 90°.

- Angular deviation, the measure of the angular variation between two adjacent cells in all directions. It has a range of 0° to 180°.

- Aspect ratio, the measure of how thin (ratio of width to length of the cells) a cell is. It has a range of 1 to 50000.

- Expansion ratio, the measure of the size variation between two adjacent cells in a specific direction. It has a range of 1 to 100.

- Cell width, i.e. the height of the cell measured in all directions. It has a range of 0 m to 1 000 000 m.

A check for negative cells is also performed at this stage.

The mesh quality can be improved by controlling the selected topology. AutoGrid™ has three predefined topologies. The HHOHH (O4H) topology allows for full automatic meshing for all kinds of turbomachinery geometries; while the HOH and H&I topologies ensure very high quality grids, but according to the user manual (AutoGrid™ Manual, 2007a) are not suitable for all applications. In the generation of the three-dimensional mesh for the axial flow fan the default O4H topology is used. The O4H topology allows control of five blocks (referring to Figure 3.2):

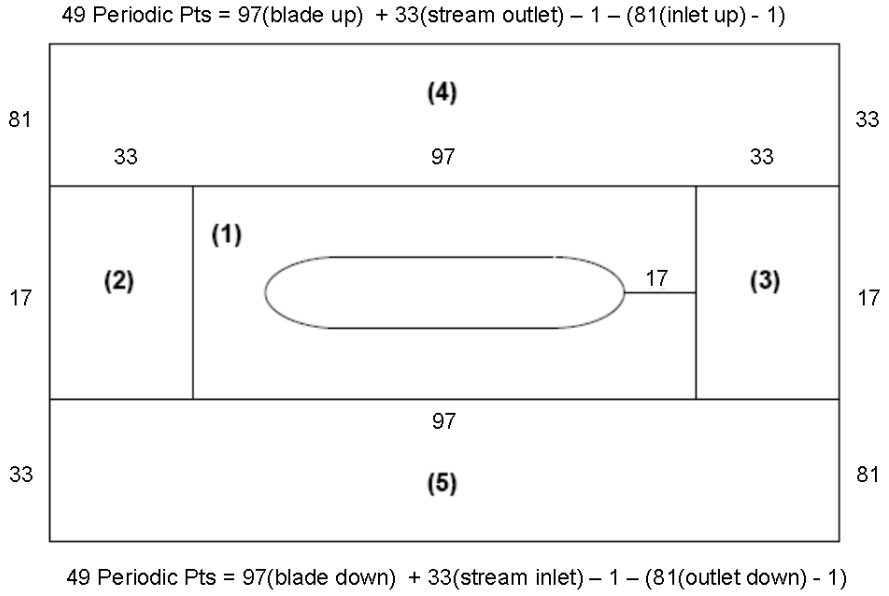

Figure 3.2: O4H topology blocks and grid points, (AutoGrid™ Manual, 2007a).

1. an O-block around the blade called the skin block
2. an H-block upstream of the blade leading edge called the inlet block
3. an H-block downstream of the blade trailing edge called the outlet block
4. an H-block above the blade section called the up block
5. an H-block below the blade section called the down block

By altering the number of grid points in the different blocks the mesh quality can be improved accordingly. Once the required mesh quality is achieved, the AutoGrid™ file is saved, allowing for automatic regeneration of the blade with the specified grid points at a later stage if needed.

3.3.2 IGG™

Both inlet and outlet segments were created by projecting blocks from a surface geometry. These projected blocks were revolved 45° around the Z-axis to create a $\frac{1}{8}^{th}$ axisymmetric model. The number of grid points in all three directions was specified at this stage. Once the required mesh quality is achieved, the clustering of cells near surfaces to be defined as walls was attempted. IGG™ (IGG™ Manual, 2007c) uses the same mesh quality criteria as AutoGrid™ (AutoGrid™ Manual, 2007a). The clustering of cells specifies the cells distribution

in any direction normal to a surface. To achieve low y^+ values, dense cell distribution (clustering) close to a wall surface is necessary. The IGG™ interface allows the creation of segment groups with the same clustering to ease and automate the process of adjusting cell clustering. Some clustering near the fan exit was implemented where high velocity gradients were expected. This step requires the mesh quality to be checked again, since the blocks need to be regenerated to accept the clustering changes.

After completing the geometry block generation and setting the periodicity for eight blades the various boundaries were specified. This includes outlet, inlet as well as solid wall boundaries. At this stage the connecting surfaces surrounding the bellmouth blocks on the inlet segment were changed to solid wall surfaces to accommodate attaching the bellmouth inlet to the fan segment.

3.3.3 Domain specifications

The complete computational domain consists of three main sections, namely the inlet to the fan, the fan rotor and the outlet. The inlet and outlet sections consist of a structured mesh generated in IGG™, including all boundary conditions and periodicities. The blade and the endwalls (hub and shroud) forming the fan rotor part of the model, were generated in AutoGrid™, including setting the periodicities. All three complete sections were integrated into a single model for the complete CFD simulation of the fan test facility by adding the inlet and outlet to the fan blade model in AutoGrid™. Saving this file creates an *.igg file (which can be manipulated within IGG™) that is integrated in the FINE™ interface to be coupled with the EURANUS flow solver. A detailed discussion of the three sections follows.

Essentially two computational domains were evaluated. Both domains shared the same inlet and blade section, but utilized different outlet sections. The first CFD model contains a pinched outlet section and will be addressed as Approach-1. The second model with an open outlet will be addressed as Approach-2. The two models consists of the same amount of grid cells, namely 4728631 cells. Figure 3.3 displays an azimuthal view of the first model with the general grid dimensions. An isometric view of the complete computational domain for the first model is illustrated in Figure 3.4. Figure 3.5 presents the general grid dimensions of the second model and an isometric view of the second model is presented in Figure 3.6. The fan diameter is denoted by d_F.

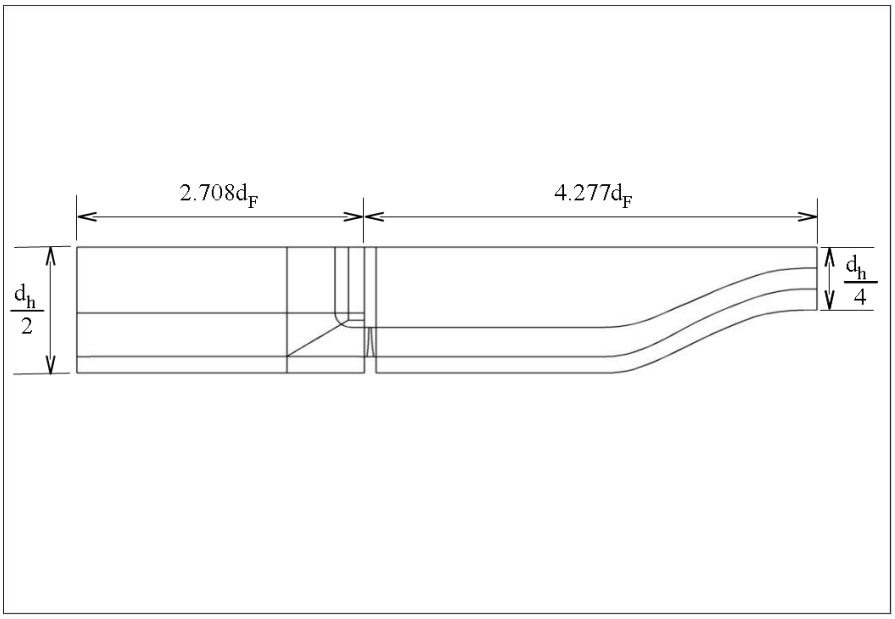

Figure 3.3: Azimuthal view of computational domain dimensions, Approach-1.

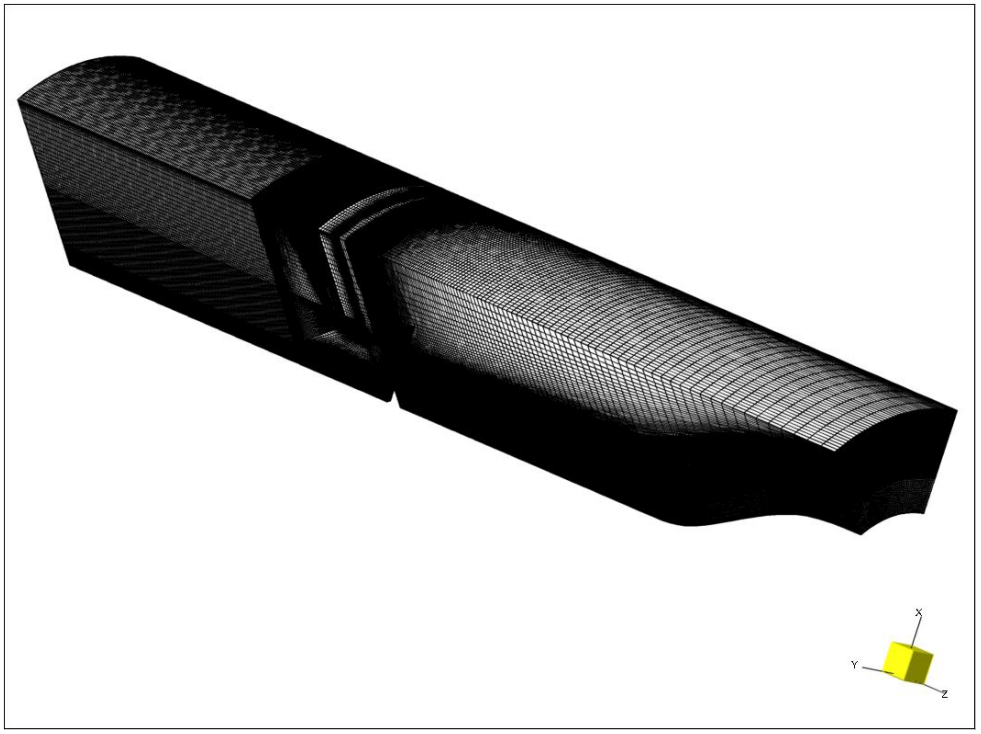

Figure 3.4: Isometric grid view of computational domain, Approach-1.

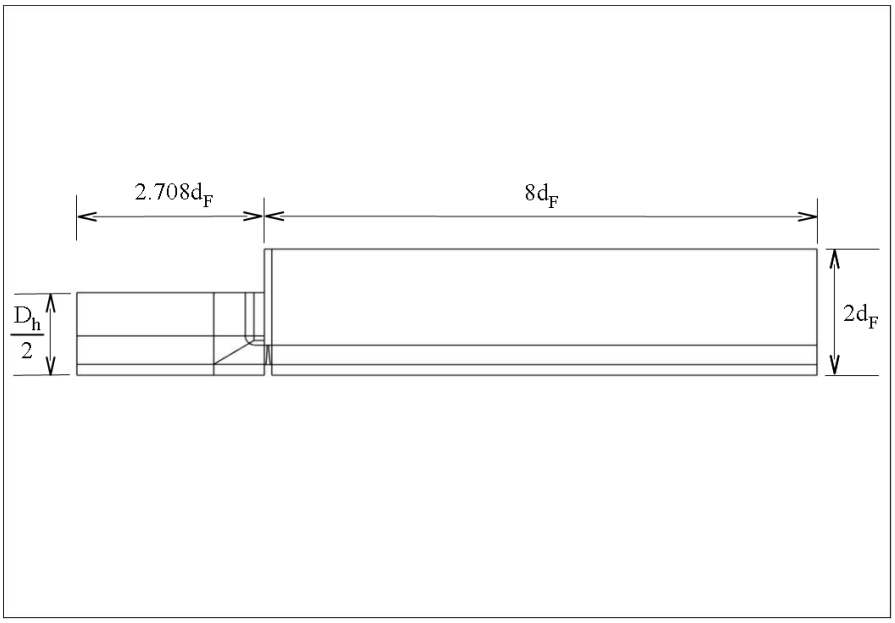

Figure 3.5: Azimuthal view of computational domain dimensions, Approach-2.

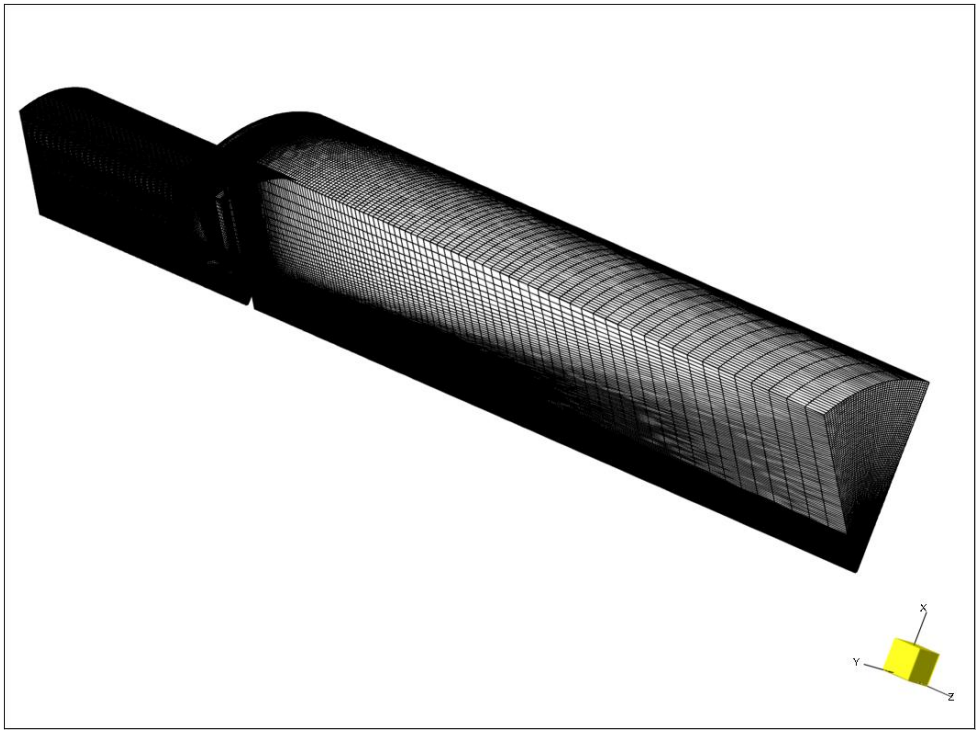

Figure 3.6: Isometric grid view of computational domain, Approach-2.

3.3.3.1 Inlet

The inlet section of the computational domain is geometrically true to the test facility dimensions beyond the mesh screens inside the settling chamber and includes the bellmouth inlet to the fan. Instead of modelling the settling chamber with a square inlet the hydraulic diameter of the settling chamber walls was calculated and used. This option is implemented to coincide with the eight-segment axisymmetric nature of the CFD model. Equation (3.3.1) shows the calculation of the settling chamber hydraulic diameter based on the principle of equal flow area. An isometric view of the inlet section, containing 1483560 cells, is illustrated in Figure 3.7. Non-rotating solid wall boundaries are specified for all walls, except at the 0.05 m inner radius, where an Euler (zero-shear) wall is used. According to White (2006) for a fixed Euler wall the no-slip condition is dropped and the tangential velocity allowed to slip. These solid wall boundaries can be seen in Figure 3.8. The inlet boundary is massflow imposed and a rotor-stator interface is assigned to the patch that is coupled with the fan rotor section. The remaining boundaries are set to periodic boundaries for a $\frac{1}{8}^{th}$ axisymmetric model.

$$\begin{aligned} d_h &= \sqrt{\frac{4\,b\,h}{\pi}} \\ &= \sqrt{\frac{(4)(3.7)(3.7)}{\pi}} \\ &= 4.175\,\mathrm{m} \end{aligned} \tag{3.3.1}$$

3.3.3.2 Blade

The grid point distribution on the O4H-topology is shown in Figure 3.2. This leads to a total of 1106311 grid points for the fan blade, hub and shroud. A tip-gap of 3 mm is incorporated in the fan blade section. A fully generated blade is displayed in Figure 3.9. The cell blocks containing the tip gap is not shown.

In order to capture the high gradients of velocity within the boundary layer, an adequate amount of cells should be placed within the boundary layer. The wall variable commonly used to evaluate this is the y^+ value. The y^+ value associated with the first node off the wall is given in equation (3.3.2), according to the FINE™/Turbo Manual (2007*b*).

$$y_1^+ = \frac{\rho\,u_\tau\,y_\mathrm{w}}{\mu} \tag{3.3.2}$$

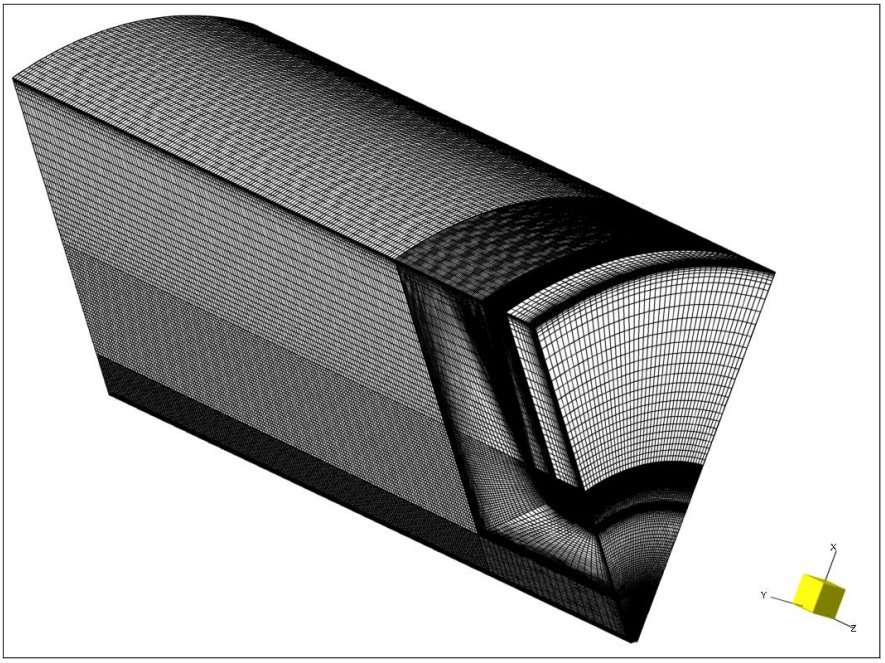

Figure 3.7: Isometric grid view of computational domain inlet section.

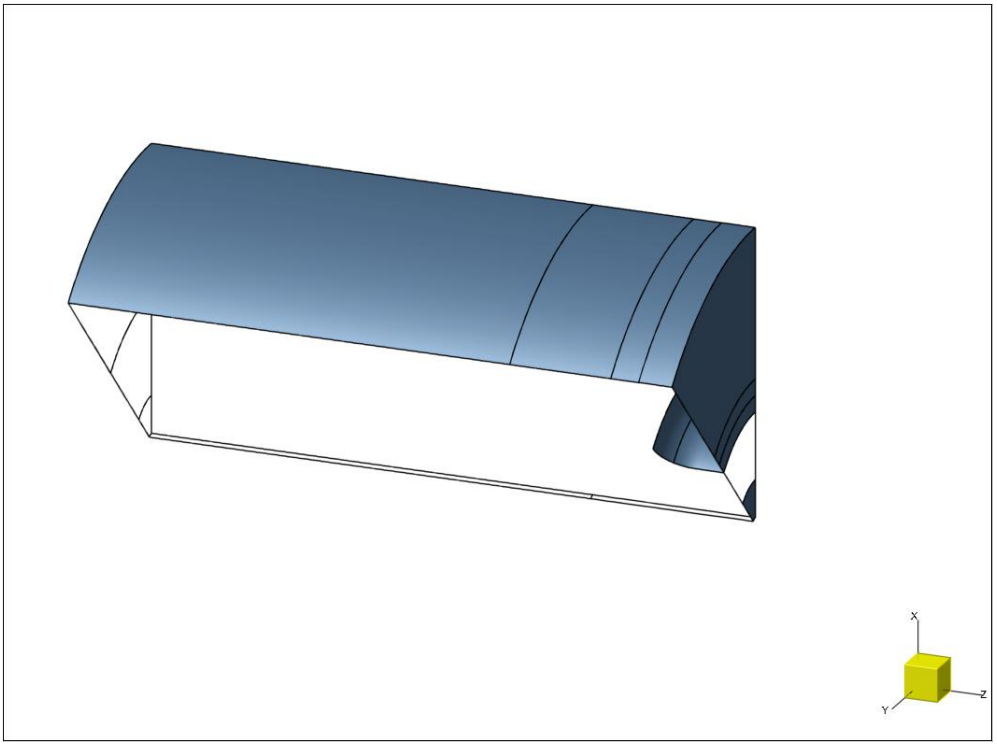

Figure 3.8: Isometric grid view of computational domain inlet section solid boundaries.

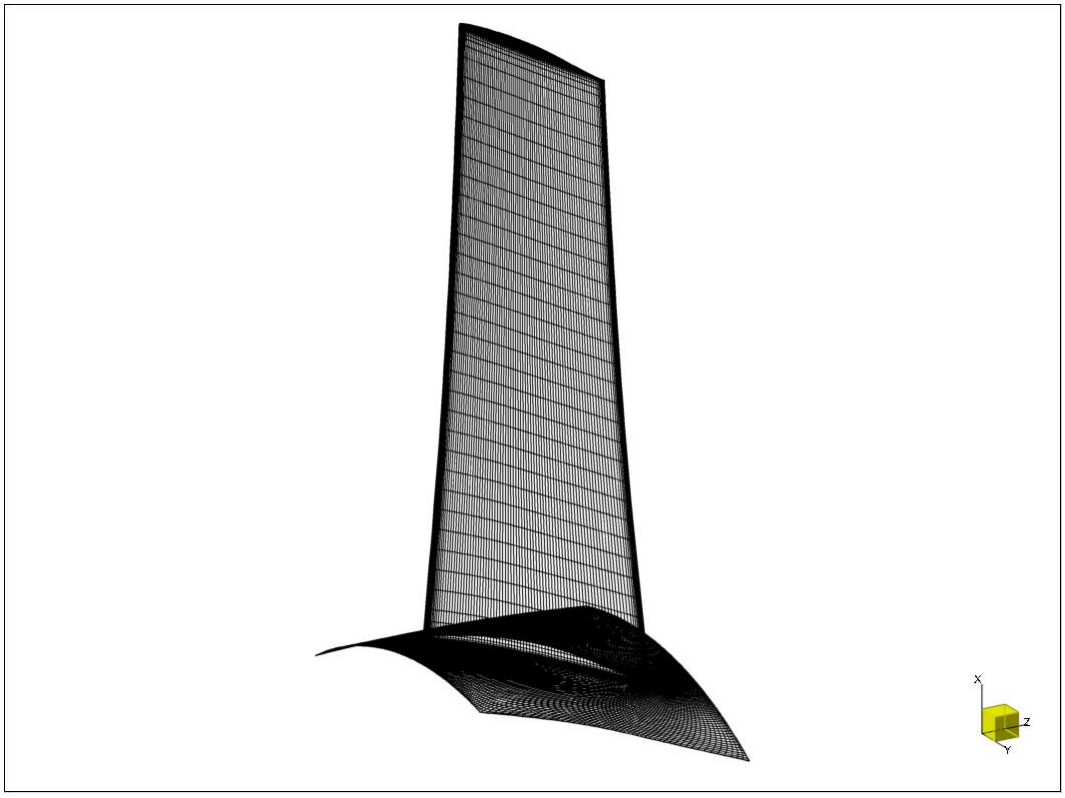

Figure 3.9: A single blade generated in AutoGrid™.

Here y_w is the height of the first grid node off the wall and u_τ is the friction velocity defined by

$$u_\tau = \sqrt{\frac{\tau_w}{\rho}} = \sqrt{\frac{1}{2} U_{ref}^2 C_f} \tag{3.3.3}$$

with τ_w the wall shear stress, U_{ref} the reference velocity and C_f the shear coefficient.

Different turbulence models for Low- and High-Re number flows require different ranges of y_1^+ values to accurately predict the boundary layer. To achieve this, the correct range of y_1^+ values per turbulence model need to be obtained. The FINE™/Turbo Manual (2007*b*) specifies that for Low-Re turbulence models solving the *viscous sublayer* ($y_1^+ \leq 5$, White (2006)), y_1^+ values between 1 and 10 is acceptable. The FINE™/Turbo Manual (2007*b*) also recommends using a Low-Re turbulence model if separation is expected, since the logarithmic function does not apply for separated flow. Since the y_1^+ value depends on the value of y_w, according to equation (3.3.2), it can be used to control the corresponding y_1^+ values based on the truncated series solution of the Blasius

equation (FINE™/Turbo Manual, 2007b):

$$\begin{aligned} y_{\mathrm{w}} &= 6\left(\frac{U_{ref}}{\nu}\right)^{-\frac{7}{8}}\left(\frac{L_{ref}}{2}\right)^{\frac{1}{8}} y_1^+ \\ &= 6\left(\frac{1.5}{1.511\times10^{-5}}\right)^{-\frac{7}{8}}\left(\frac{0.167}{2}\right)^{\frac{1}{8}} \quad (5) \\ &= 9.335{\times}10^{-4} \end{aligned} \tag{3.3.4}$$

where U_{ref} can be taken as the average inlet velocity, ν the kinematic viscosity and L_{ref} the reference length (taken as the blade chord length). The y_1^+ value for the blade is well within the 1 to 10 range ($y_1^+ \leq 9.551$), and only reaches the limit of 10 near the tip gaps (Figure 3.10). This was deemed sufficient since the tip clearance flow consists of highly accelerating fluid and is different from a normal boundary layer.

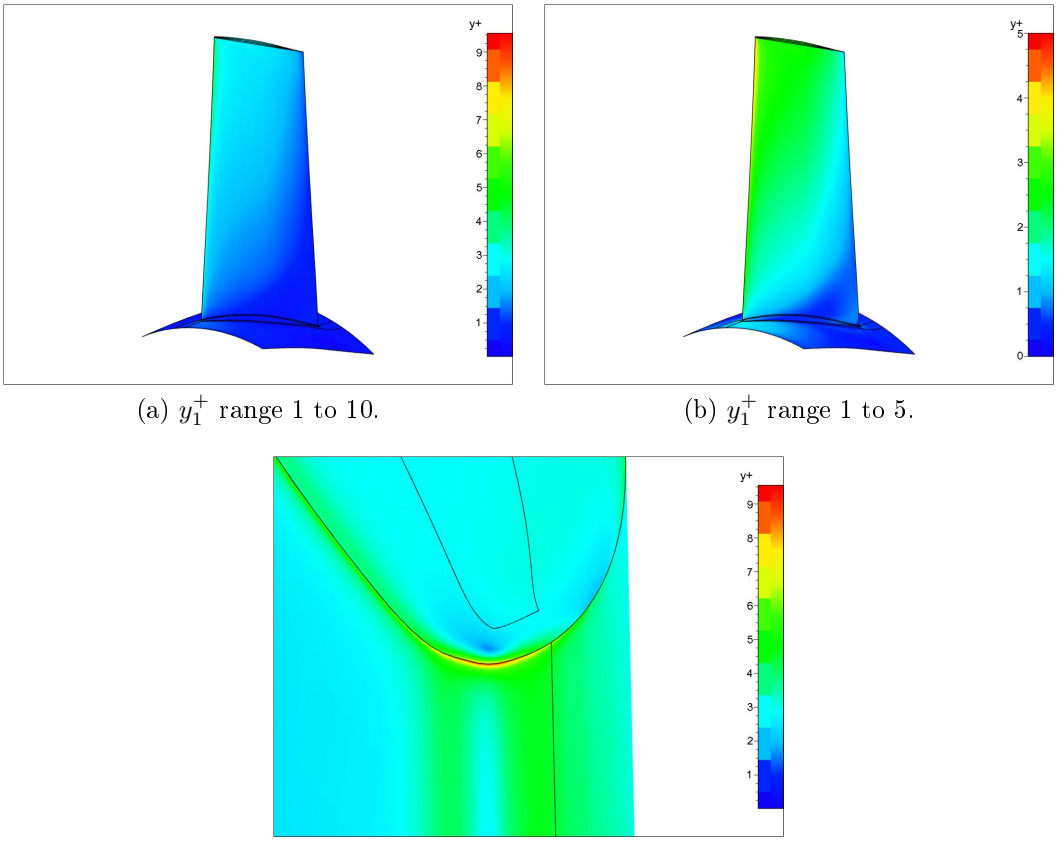

(a) y_1^+ range 1 to 10.

(b) y_1^+ range 1 to 5.

(c) y_1^+ near tip gap.

Figure 3.10: y_1^+ values for the blade section.

Non-rotating solid wall boundaries are specified for the shroud. The blade and hub are assigned solid surfaces rotating at 750 rpm. The patches connecting

the inlet and outlet sections to the fan rotor sections are specified as rotor-stator interfaces. The remaining boundaries are set to periodic boundaries for a $\frac{1}{8}^{th}$ axisymmetric model. Figure 3.11 gives an indication of the axisymmetric nature of the CFD model.

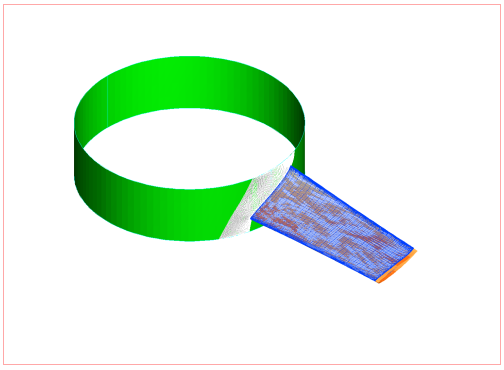

(a) $\frac{1}{8}^{th}$ axisymmetric model, without repetition.

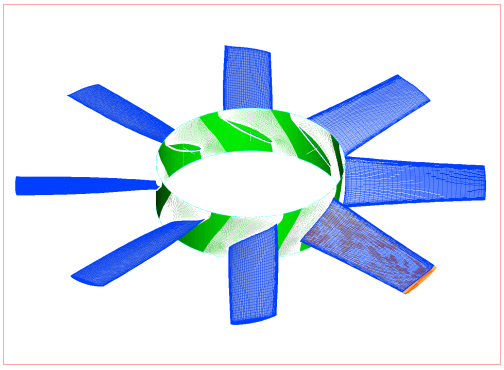

(b) $\frac{1}{8}^{th}$ axisymmetric model, with repetition.

Figure 3.11: Axisymetric nature of CFD model.

3.3.3.3 Outlet

The fan test facility on which the computational domain is based, houses a fan that exhausts into the open atmosphere. Defining such an "open atmosphere" outlet within a computational domain is problematic. To keep the integrity of the model intact would require outlet patches in both the axial and radial directions. This opens the possibility for a large amount of backflow to enter the domain at the outlet boundary and severely destabilize the simulation. The support team at NUMECA strongly advised against using such an "open" outlet and deemed any results obtained from such simulations untrustworthy. To resolve this issue the outlet is pinched for Approach-1, some distance away from having an influence on the fan performance. The only objective of the pinching is to increase the local velocity in this region and to restrict the backflow over the outlet. The static outlet pressure is not taken at the pinched outlet, but rather averaged over a series of surfaces, on the constant z-plane, before the pinching in the model commences. The static pressure value of each surface is an averaged value for the static pressure over the particular area. Figure 3.12 shows a plot of these surfaces. To resolve the radial outflow issue, Euler walls are implemented at the endwalls of the outlet. With the no-slip condition removed for Euler walls, they only prohibit the flow from exiting the model, thus aiding the pinching effect. The Euler walls are placed sufficiently

far away from the fan rotor.

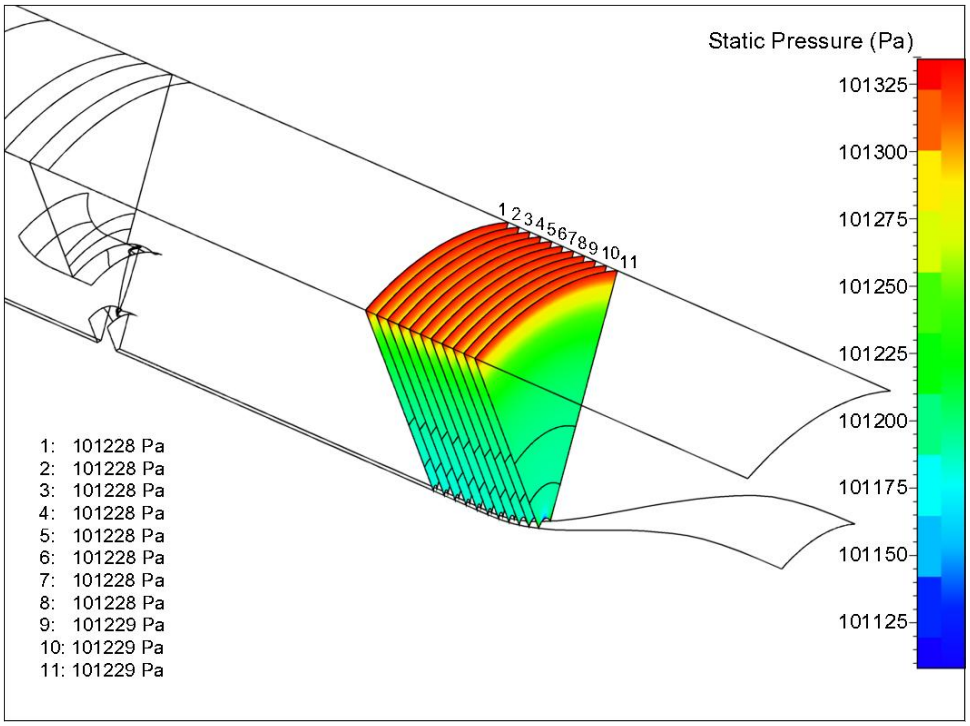

Figure 3.12: Averaged surfaces for obtaining outlet pressure.

Similar to the inlet, the patch connecting the outlet section with the fan rotor is specified as a rotor-stator patch. The patch coinciding with the outside wall of the settling chamber is defined as a solid wall. The remaining patches are assigned Euler walls, referring to the discussion earlier. A radial equilibrium static pressure is enforced at the outlet patch with atmospheric pressure imposed at the outer circumference. The complete computational domain, of 2138760 cells, is illustrated in Figure 3.13.

The outlet section for Approach-2 avoids the use of a pinched outlet and zero-shear Euler walls. The circumferential outlet patch employs a static pressure boundary condition. The outlet patch on the plane normal to the fan axis imposes a radial equilibrium static pressure boundary condition, similar to the outlet section of Approach-1. Both outlet sections contain the same amount of cells and are connected to the fan rotor via a rotor-stator interface. The complete computational domain is presented in Figure 3.14.

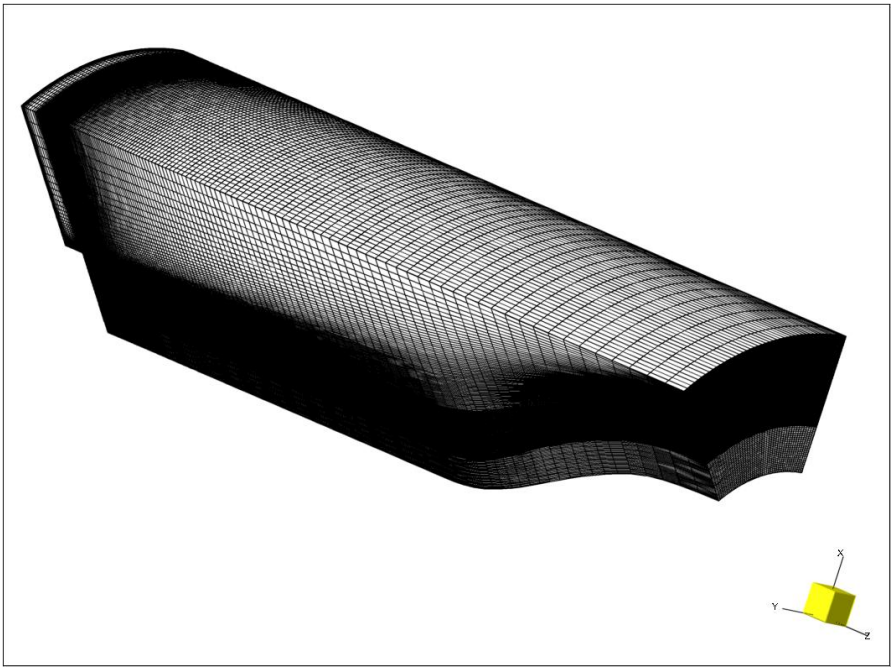

Figure 3.13: Isometric grid view of computational domain outlet section, Approach-1.

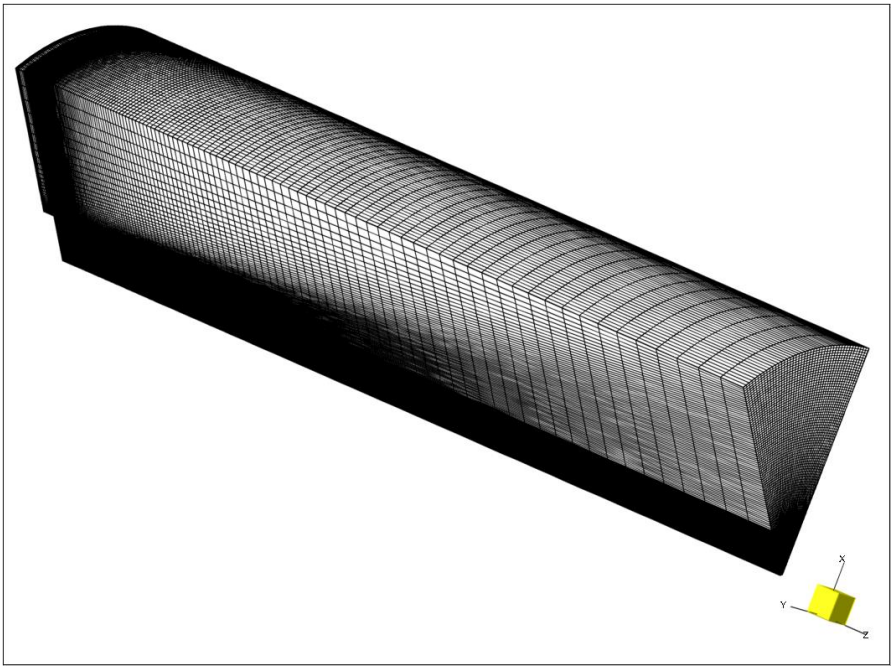

Figure 3.14: Isometric grid view of computational domain outlet section, Approach-2.

3.4 Computational parameters

All the parameters necessary to set up and facilitate a steady-state flow simulation are discussed in detail.

3.4.1 Fluid Model

Within FINE™ it is possible to choose a fluid type from a pre-defined database or create a new fluid type. The pre-defined database contains the following types of fluids: perfect gas, real gas, incompressible gas or liquid and condensable fluid.

After researching the user manual it became apparent that FINE™'s real gas is actually a thermally perfect gas and the perfect gas a calorically perfect gas. According to Anderson (1990) a true real gas has an equation of state that takes compressibility effects, variable heat capacity, Van Der Waals forces, non-equilibrium thermodynamic effects and issues with molecular dissociation and elementary reactions into account. This is a very extensive analysis and various simpler gas laws exist. The ideal gas law simplifies the real gas by assuming a compressibility factor of one. White (2006) stipulates that "all common gases follow with reasonable accuracy, at least in some finite region, the so-called ideal or perfect gas law". Furthermore a perfect gas can be defined as one where the intermolecular forces of the real gas are neglected to simplify calculations. Anderson (1990) states that this perfect gas simplification can be further simplified and classified as a thermally perfect gas and a calorically perfect gas.

The thermally perfect gas assumes that the gas is in thermodynamic equilibrium, not chemically reacting and that internal energy, enthalpy, and specific heats are functions of temperature only. The calorically perfect gas enforces all the assumptions of the thermally perfect gas, but assumes constant specific heats. In FINE™ the perfect gas model assumes constant specific heat (C_p) and constant specific-heat ratio (γ).

For the incompressible fluid type the density can either be constant or a pre-defined function of the pressure. Using air as an incompressible gas in the default FINE™ setting, the density law is defined by the Boussinesq law, in which case the density is kept strictly constant. With no terms in the mass and momentum equations depending on the temperature, these conservation equations are decoupled from the energy conservation equation.

Relative stable fluid temperature meant that the use of the real gas (thermally perfect gas) fluid type was not considered. The perfect gas (calorically perfect gas) and incompressible fluid types were investigated and a fan static pressure

rise error amongst the two fluid types of less than 3 % was found. However the incompressible fluid type required almost double the amount of iterations to give answers that correlate with the perfect gas fluid type. Therefore the perfect gas model was used for the axial flow fan model.

3.4.2 Flow Model

For this model steady flow is assumed and time independent flow calculations are solved. This investigation considers a one-equation turbulence model, namely Spalart-Allmaras (Spalart and Allmaras, 1994). The Spalart-Allmaras turbulence model is NUMECA's default model, providing good convergence for common turbomachinery applications (FINE™/Turbo Manual, 2007b). The Spalart-Allmaras turbulence model performs considerably better than the algebraic turbulence models, such as the Baldwin-Lomax model, especially in mapping the performance of separated flow (Ashford and Powell, 1996). The model is also more robust, computationally less expensive and requires less memory than the two-equation $k - \varepsilon$ turbulence model (Ashford and Powell (1996). Both models employ constant Prandtl numbers.

3.4.3 Rotating Machinery

FINE™ allows the user to specify rotating blocks and rotor-stator interfaces to accommodate rotating and non-rotating sections within a domain. In this mesh the blocks were all set to be rotating while the relevant solid surfaces, such as the shroud and settling chamber walls, were kept stationary. This approach is somewhat similar to that used by Kelecy (2000) who kept the blades and shaft stationary, while maintaining an angular velocity at the outer walls in the opposite direction from the supposed blade rotation.

An attempt was made to utilize the classic turbomachinery simulation approach where only the blocks containing the rotor were allowed to rotate, keeping the remaining blocks stationary. In this instance two rotor-stator interface types, the mixing plane approach and the frozen rotor, were investigated:

- With the mixing plane approach circumferentially averaged flow quantities (such as mass, momentum and energy fluxes) are exchanged at the rotor-stator interface. According to the FINE™/Turbo Manual (2007*b*) a more strict global conservation through the interface is achieved when using a flux based approach instead of exchanging the classical primitive variables. Thus any blade wake or separation is mixed circumferentially before entering the downstream component, resulting in a circumferentially uniform pressure distribution as well as uniform velocity components at the interface. The static pressure distribution over the rotor-stator can be viewed in Figure 3.15.

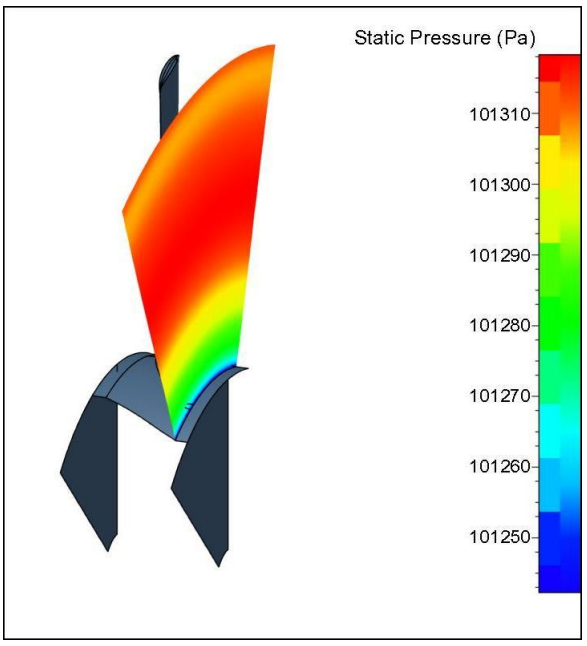

Figure 3.15: Static pressure distribution over the mixing plane approach rotor-stator interface.

- With the frozen rotor approach no mixing of the flow solution at the interface occurs. Instead the rotor movement is neglected and the upstream and downstream components can be seen as being literally connected. Thus the continuity of the velocity components and pressure is imposed on the interface. The governing equations for the rotor are solved in a relative reference frame, and that of the stator in an absolute reference frame. The flow solution is thus dependent on the relative position of the rotor and stator sections. The static pressure distribution over the rotor-stator can be viewed in Figure 3.16.

Unfortunately neither of the aforementioned methods provided satisfactory results. For Approach-1 the mixing plane approach delivered the closest results compared to the experimental data with a 28.7 % error in fan static pressure rise at the design operating point. This was only achieved after 18234 iterations with a very unstable simulation. The frozen rotor approach was more stable, but could only achieve a 53.82 % error in fan static pressure rise compared to experimental data. The aforementioned results were produced with a zero-order extrapolation of flow quantities from inner cells to the rotor-stator interface. Using first-order extrapolation provided somewhat better results at a 111-grid-level (coarser mesh), but it was too unstable at a 000-grid-level (finest mesh) and the simulations could not complete more than 1000 iterations before diverging, for both cases.

One of the problems with using the aforementioned approach, is the mixing

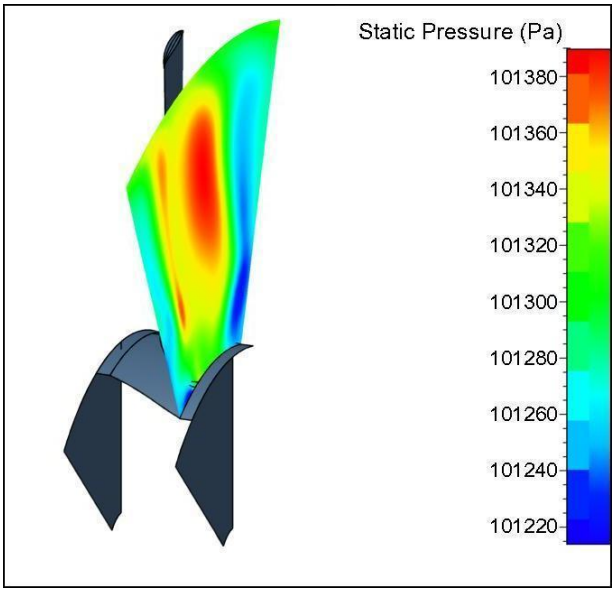

Figure 3.16: Static pressure distribution over the frozen rotor rotor-stator interface.

losses introduced at the rotor-stator interfaces due to the flow being forced to mix out in a short distance, where normally it would have had an infinite distance to do so. The mixing losses over the rotor-stator interface can range anywhere from 10 Pa to 100 Pa; which is small enough to be neglected in turbomachinery applications with a big pressure rise. However, in this application it is an order of magnitude of the pressure capability of the axial flow fan and influences the fan performance considerably.

Another issue unique to the axial flow fan is the amount of backflow observed at the rotor-stator interface. The backflow increases significantly at lower flow rates and is a major source of unsteadiness in the simulation. With the mixing plane approach the azimuthal averaged flow quantities on the downstream side of the blade outlet rotor-stator interface contains backflow and is different from the flow quantities on the upstream side. To resolve this issue the rotor-stator interface would need to be placed far enough downstream to avoid having backflow over the interface. This would also allow the flow to mix out naturally before reaching the interface, therefore eliminating mixing losses. In effect this is what has been done in the current model, where the rotor-stator interfaces have essentially been moved all the way to the inlet and outlet boundaries. Having no stator-like structures in the geometry of the axial flow fan, neglecting the need for a rotor-stator interface in the flow domain, the error introduced by allowing all the blocks to rotate is small.

The aforementioned simulation approach is commonly used for three-dimensional

wind turbine simulations (Sezer-Uzol and Long, 2006).

3.4.4 Boundary Conditions

FINE™ allows the specification of five different types of boundary conditions: inlet, outlet, solid walls, periodic and external (far field).

The use of a mass flow and static temperature imposed inlet boundary and static pressure outlet boundary for the axial flow fan was advised per email correspondence with the NUMECA support team and mentioned as the advisable setup for compressible or low-speed flows in the FINE™/Turbo Manual (2007*b*). According to the manual this setup stabilizes the flow calculations and provides better initial solutions for multistage calculations.

At the inlet boundary the mass flow is imposed through a specified control surface consisting of related patches grouped together. With this boundary condition the velocity vector and temperature is imposed on the same control surface. For the velocity vector either the swirl and the direction of the velocity vector in the meridional plane or the direction of the absolute velocity vector can be imposed. The latter was enforced since no swirl is expected at the inlet boundary which coincides with the exit of the mesh screens in the settling chamber of the fan test facility. The absolute velocity vector is specified in the axial direction: $\left(\frac{U_z}{\mid U \mid} = 1\right)$. The static temperature can either be specified as a constant or as a relation between the inlet static pressure and the average static pressure along a specified outlet. The latter option is not applicable to the current setup as it requires the massflow imposed at both inlet and outlet boundaries. Furthermore, the turbulent viscosity μ_t for the Spalart-Allmaras turbulence model need to be specified at the inlet boundary. All specified values are absolute quantities.

Imposing static pressure at the outlet boundary can be done with three different methods:

1. Imposing a uniform static pressure across the control surface. For this case the static temperature and velocity components at the boundary are extrapolated from the nearest control volumes.

2. Imposing an average pressure across the control surface. The average static pressure is specified and instead of a uniform pressure distribution the pressure profile is extrapolated from the inner cells and translated to ensure the average pressure value that was specified is met at the control surface.

3. Using radial equilibrium. Since this model has a cylindrical outlet with mesh lines at constant radius the static pressure can be imposed at a constant radius (the outer radius in this case). The hub-to-shroud pressure profile is then calculated by integrating the radial equilibrium equation (3.4.1) in the spanwise direction with pitchwise averaged values of v_θ and r.

$$\frac{\partial p}{\partial r} = \rho \cdot \frac{v_\theta^2}{r} \tag{3.4.1}$$

The option of using radial equilibrium provided the best results.

The velocity and thermal conditions for solid wall patches are defined using the solid wall boundary type. The boundary can be either defined as zero-slip or zero-shear. The settling chamber walls, shroud and bellmouth surfaces are defined as zero-slip walls with a zero rotational velocity. All the rotating surfaces consisting of the blade and hub surfaces are defined as zero-slip walls with a rotational velocity of 750 rpm. All zero-slip walls are defined as adiabatic.

All rotating surfaces are utilized to compute the force and torque of the system. For the cylindrical axial flow fan model the axial thrust is defined as the projection of the global force on the rotation axis and the couple exerted by the global force, around the rotational axis of the fan, as the torque. The axial thrust is computed from the pressure and velocity fields of the fluid acting on the blade surfaces according to equation (3.4.2):

$$\sum_S \vec{F} \cdot \vec{n_z} \tag{3.4.2}$$

The projection of the torque along a given direction $\vec{z}$ is given by equation (3.4.3).

$$\left(\sum_S \vec{r} \times \vec{F} \right) \cdot \vec{z} \tag{3.4.3}$$

3.4.5 Numerical Model

Three computational parameters allow the user to improve the convergence rate of the simulation:

- CFL number
- Multigrid parameters
- Preconditioning parameters

3.4.5.1 CFL number

The Courant-Friedrichs-Levy (CFL) number scales the time-step sizes that are used for the time-marching scheme of the flow solver. A higher CFL number leads to faster convergence but can lead to divergence and unstable simulations (FINE™/Turbo Manual, 2007b). The inverse of this is also applicable where choosing a smaller CFL number in an unstable simulation improves convergence. At the low flow sections of the fan performance curve, a lower CFL number was chosen to improve the convergence of the simulation.

3.4.5.2 Multigrid parameters

For efficiency and fast convergence the EURANUS flow solver uses a multigrid strategy in solving the flow equations on different grid levels. To complement this, a Full Multigrid Strategy option is also available wherein the solution of a coarser grid level is used as an initial solution for the next level of finer grid.

With the flow solver automatically coarsening the initial mesh from IGG™ an option is available to run simulations on several sub-meshes. The coarsest grid level that can be achieved with any mesh depends on the number of times the grid can be coarsened along each of the (I, J, K) directions. This number would be represented by "n" in equation (3.4.4)

$$cell\ size = 2^n \tag{3.4.4}$$

For example, if a grid size is defined by $8 \times 16 \times 16$ cells in the I, J, K directions respectively, the mesh can be coarsened to 3,4,4 grid levels in the respective directions. Figure 3.17 displays grid level coarsening in one direction. The same effect on the hub grid distribution around the fan blade can be viewed in Figure 3.18. However, using a hybrid grid level structure as described above may deform the mesh in a preferential direction upon coarsening. This might increase the aspect ratio for instance and effectively reduce the quality of the overall mesh. In setting up a mesh in IGG™ care should be taken to keep a uniform grid level distribution. The finest grid level is denoted by a 0 in any (I, J, K) direction and the coarser grid levels follow in a numerical order: 0,1,2... (see Table 3.1 for a grid level display of the previous example). In the axial flow fan model three grid levels 222, 111 and 000 were used to obtain a flow solution.

With the Multigrid Strategy the flow calculation is performed on all the grid levels simultaneously in order to speed up convergence. The EURANUS flow solver implements an explicit multi-stage Runge-Kutta time marching scheme. The number of times the Runge-Kutta operator is applied (number of sweeps) can be specified for each grid level. The coarse grid level to fine grid level sweep of the multigrid cycle is initiated once a solution of the coarsest mesh is

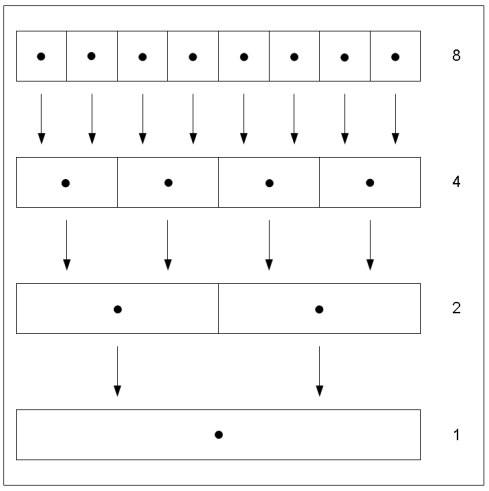

Figure 3.17: Mutigrid Strategy.

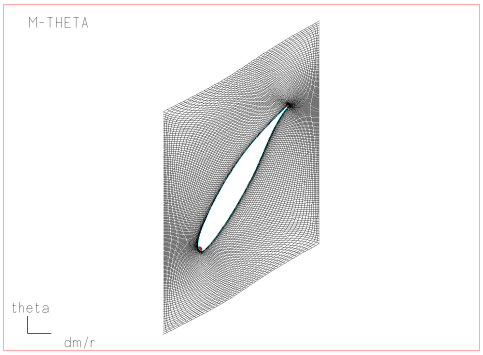

(a) Finest mesh resolution, 000.

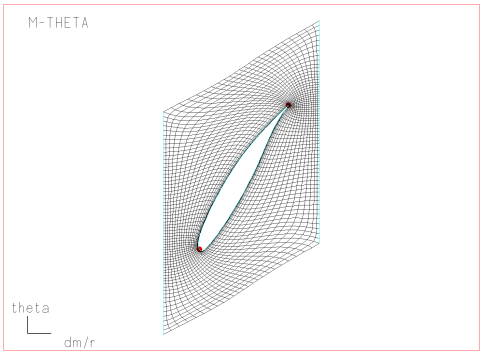

(b) Coarser mesh resolution, 111.

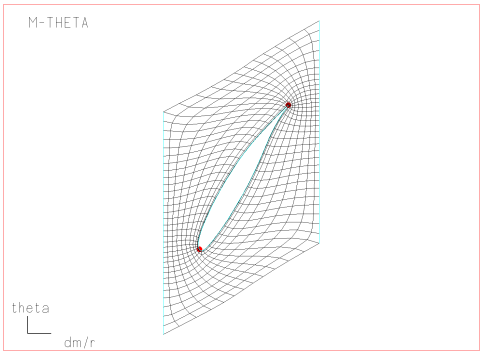

(c) Coarsest mesh resolution, 222.

Figure 3.18: Multigrid resolution for the blade hub.

achieved and smoothed. The current solutions on finer grids are updated with the solution on the next coarser grid level. This approach leads to an efficient and fast convergence (FINE™/Turbo Manual, 2007b).

Table 3.1: Grid level distribution.

Grid level notation	Grid points in I, J, K direction	Number of grid points
0 0 0	9×17×17	2601
1 1 1	5×9×9	405
2 2 2	3×5×5	75
3 3 3	2×3×3	18
3 4 4	2×2×2	8

The option of using a Full Multigrid Strategy provides a good initial solution. A preliminary multi-stage Runge-Kutta explicit scheme is started on the coarsest grid level, but the solution will not be interpolated to the next finer grid level, until a specified convergence is achieved. This solution is then applied as an initial solution on the finer grid level for further iterations. The cycle is repeated until the finest grid level is reached. The grid level at which the preliminary run should be initiated (level 222 or 111) as well as the number of iterations to be performed on the corresponding grid level (if convergence is not achieved) can be specified for each grid. It was found that if convergence on coarser grid levels were not obtained it resulted in divergence of the simulation on finer grid levels. For the axial flow fan model care was taken to ensure a good level of convergence was achieved before initializing the next finer mesh with the previous solution. The larger cell size of the coarsest mesh leads to a fast convergence, which provides a good initial solution and allows a more robust simulation on the finest grid level.

3.4.5.3 Preconditioning parameters

Within FINE™ preconditioning is automatically utilized for incompressible flows and serves as a viable option for other low Mach number fluid types to improve the convergence rate.

According to the FINE™ user manual "when the magnitude of the flow velocity becomes small in comparison with the acoustic speeds, time marching compressible codes converge very slowly". This problem is addressed with the use of a low speed preconditioner. A preconditioning matrix is multiplied with the time derivatives of the unknowns that arise in the flow equations when time marching algorithms are used to solve steady state applications. These time derivatives have no physical meaning and can be modified without altering the final steady state solution. This results in reduced round-off errors at low Mach numbers (caused by the use of absolute pressure in the momentum equations) by the introduction of reduced flow variables such as the dynamic

pressure and the dynamic enthalpy. Also, by using a pseudo-wave speed in order of magnitude of the fluid speed, instead of the acoustic wave speed, the difference between the convective and the acoustic eigenvalues are lessened.

For the axial flow fan model Merkle preconditioning was used. The Merkle preconditioner is amongst the most popular used perconditioners and has been extended, from a very efficient preconditioner for two-dimensional low Mach number flows, to also solve three-dimensional flows (Turkel *et al.* (1997), Zhonghua *et al.* (2007) and Vigneron *et al.* (2008)).

3.4.6 Initial Solution

FINE™ allows, amongst other, the option to either initialize a computation from constant values or from an initial solution file. In the former case physical values need to be specified that are used uniformly in all the blocks except on the boundaries. The variables for these values are static pressure, static temperature and the velocity components. This method of initialization was used for the coarsest (222) grid level. For the intermediate grid level (111) coarse grid initialization was used where the 111-grid-level computation was automatically started from the 222-grid-level computation after a few iterations. The 111-grid-level computation was allowed to converge to provide an initial solution file to be used in the latter initialization method mentioned earlier. The finest grid level (000) computation was started from this initial solution file. Using this approach accelerated the convergence rate and removed the risk op having a solution diverging at a finer grid level due to starting from an unconverged initial solution from a coarser grid level. Using this hybrid approach is especially beneficial at very low flow rates where a lower CFL number is needed. The 222- and 111-grid-level computations can still be solved with a higher CFL number, for faster convergence, and with the switch to the finest grid level (000), a lower CFL number is chosen to stabilize the computation.

3.4.7 Output

In order to have efficient memory usage and still retain all the flow quantities of immediate interest, FINE™ allows specifying the necessary flow quantities to be saved and lets the post-processing package CFView™ calculate the derived quantities. The flow quantities can either be calculated at all the mesh nodes or along the solid wall boundaries.

3.4.8 Computation Steering and Monitoring

FINE™ allows multi-process analyses where the convergence histories of multiple computations can be viewed simultaneously. Utilizing the MonitorTurbo

interface the default quantities for a turbomachinery computation can be viewed independently. The residuals relative to the transport equations are also made available.

The residuals are calculated as a flux balance of the fluxes summed on all the faces of each cell:

$$RES = \sum fluxes \tag{3.4.5}$$

The root mean square and the maximum of the residuals are calculated according to the following relations:

$$RMS_{RES} = log\left(RMS\left(\frac{RES}{cell\ volume}\right)\right) \tag{3.4.6}$$

$$MAX_{RES} = log\left|MAX\left(\frac{RES}{cell\ volume}\right)\right| \tag{3.4.7}$$

For the axial flow fan model a decrease of three orders with stabilization in the RMS residual curve was considered to be good convergence, along with a difference of less than 5 % between massflow at inlet and outlet.

3.5 Governing Equations

The basic Reynolds-Averaged Navier-Stokes equations solved in the EURANUS flow solver, as defined in the FINE™/Turbo Manual (2007*b*) are presented in this section.

3.5.1 General Navier-Stokes Equations

The general Navier-Stokes equations can be expressed in a Cartesian frame of reference as:

$$\frac{\partial}{\partial t}\vec{X} + \nabla\vec{F}_I + \nabla\vec{F}_V = \vec{Q} \tag{3.5.1}$$

$\vec{X}$ is the vector of the conserved variables:

$$X = \begin{bmatrix} \rho \\ \rho\vec{v} \\ \rho E \end{bmatrix} \tag{3.5.2}$$

$\vec{F}_I$ and $\vec{F}_V$ are the respective flux vectors:

$$F_{Ii} = \begin{bmatrix} \rho v_i \\ \rho v_1 v_i + p\delta_{1i} \\ \rho v_2 v_i + p\delta_{2i} \\ \rho v_3 v_i + p\delta_{3i} \\ (\rho E + p) v_i \end{bmatrix} \tag{3.5.3}$$

and

$$-F_{Vi} = \begin{bmatrix} 0 \\ \tau_{i1} \\ \tau_{i2} \\ \tau_{i3} \\ q_i + \mathrm{v}_j \tau_{ij} \end{bmatrix} \tag{3.5.4}$$

The stress and heat flux components are obtained from:

$$\tau_{ij} = (\mu + \mu_t) \left[\frac{\partial \tilde{\mathrm{w}}_i}{\partial x_j} + \frac{\partial \tilde{\mathrm{w}}_j}{\partial x_i} - \frac{2}{3} (\nabla \vec{\mathrm{w}} \delta_{ij}) \right] \tag{3.5.5}$$

and

$$q_i = (K + K_t) \frac{\partial}{\partial x_i} \tilde{T} \tag{3.5.6}$$

The source terms are contained within Q:

$$Q = \begin{bmatrix} 0 \\ \rho \vec{f}_e \\ \mathrm{W}_f \end{bmatrix} \tag{3.5.7}$$

$\vec{f}_e$ expresses the external force effects and W_f the work performed by those external forces, according to the following relation:

$$\mathrm{W}_f = \rho \vec{f}_e \cdot \vec{\mathrm{v}} \tag{3.5.8}$$

3.5.2 Time averaging of quantities

Time averaging is applied to the Navier-Stokes equations. The instantaneous value of the density and pressure is time averaged according to the following relation:

$$q = \bar{q} + q' \tag{3.5.9}$$

$\bar{q}$ is the time averaged (mean) value, q' the fluctuating part and the mean fluctuation

$$\bar{q}' = 0 \tag{3.5.10}$$

The energy, temperature and velocity components are density weighted averages following the relation:

$$\tilde{q} = \frac{\bar{\rho q}}{\bar{\rho}} \tag{3.5.11}$$

3.5.3 Treatment of turbulence in the equations

For treating turbulence a first-order closure model based on the Boussinesq assumption for the turbulent shear is used:

$$-\overline{\rho \mathrm{w}_i'' \mathrm{w}_j''} = \mu_t \left[\frac{\partial \mathrm{w}_i}{\partial x_j} + \frac{\partial \mathrm{w}_j}{\partial x_i} - \frac{2}{3}(\overrightarrow{\nabla \tilde{\mathrm{w}}})\delta_{ij} \right] - \frac{2}{3}\bar{\rho} k \delta_{ij} \tag{3.5.12}$$

In this case w_i is the x_i component of the relative velocity and k the turbulent kinetic energy defined as:

$$k = \frac{1}{2}\frac{\overline{\rho \mathrm{w}_i'' \mathrm{w}_i''}}{\bar{\rho}} \tag{3.5.13}$$

The contribution of the turbulent kinetic energy to the static pressure and total energy is defined as:

$$\bar{p^*} = \bar{p} + \frac{2}{3}\bar{\rho} k \tag{3.5.14}$$

and

$$\tilde{E} = \tilde{e} + \frac{1}{2}\tilde{\mathrm{w}}_i \tilde{\mathrm{w}}_i + k \tag{3.5.15}$$

There is no term for the angular velocity in equation (3.5.15), however it is accounted for in the source term. When assuming stationary flow, the term for the angular velocity should correspond to the last term in equation (3.5.19).

3.5.4 Formulation in rotating frame for the relative velocity

The time averaged Navier-Stokes equations for the relative velocity components in the relative rotating frame of reference are defined as:

$$X = \begin{bmatrix} \bar{\rho} \\ \bar{\rho}\tilde{w}_1 \\ \bar{\rho}\tilde{w}_2 \\ \bar{\rho}\tilde{w}_3 \\ \bar{\rho}\tilde{E} \end{bmatrix} \tag{3.5.16}$$

$$F_{Ii} = \begin{bmatrix} \bar{\rho}\tilde{w}_i \\ \bar{p^*}\delta_{1i} + \bar{\rho}\tilde{w}_i\tilde{w}_i \\ \bar{p^*}\delta_{2i} + \bar{\rho}\tilde{w}_i\tilde{w}_i \\ \bar{p^*}\delta_{3i} + \bar{\rho}\tilde{w}_i\tilde{w}_i \\ \left(\bar{\rho}\tilde{E} + \bar{p^*}\right)\tilde{w}_i \end{bmatrix} \tag{3.5.17}$$

$$-F_{Vi} = \begin{bmatrix} 0 \\ \tau_{i1} \\ \tau_{i2} \\ \tau_{i3} \\ q_i + \tilde{w}_j\tau_{ij} \end{bmatrix} \tag{3.5.18}$$

The shorthand notation, i, in the expression for $-F_{Vi}$ denotes derivatives with respect to x_i.

The source term vector that contains the contributions of the Coriolis and centrifugal forces is defined as:

$$Q = \begin{bmatrix} 0 \\ -(\bar{\rho})\left[2\vec{\omega} \times \vec{w} + (\vec{\omega} \times (\vec{\omega} \times \vec{r}))\right] \\ \rho\vec{w}\,\vec{\nabla}\left(0.5\omega^2 r^2\right) \end{bmatrix} \tag{3.5.19}$$

The angular velocity in the relative reference frame is denoted by ω.

3.5.5 Formulation in rotating frame for the absolute velocity

Normally the governing equations for rotating systems are solved for the relative velocity components in the relative frame of reference. However, as described in Chapter 5, Section 5.4, the excess artificial dissipation in the far field region is lessened by solving the absolute velocity components in the relative reference frame.

The Reynolds stresses now become:

$$-\overline{\rho v_i'' v_j''} = \mu_t\left[\frac{\partial v_i}{\partial x_j} + \frac{\partial v_j}{\partial x_i} - \frac{2}{3}(\overrightarrow{\nabla\tilde{v}})\delta_{ij}\right] - \frac{2}{3}\bar{\rho}k\delta_{ij} \tag{3.5.20}$$

Here v_i is the x_i component of the absolute velocity.

The flux vectors mentioned earlier are decomposed into Cartesian components:

$$\begin{aligned} F_I &= f_{I1}\vec{1_x} + f_{I2}\vec{1_y} + f_{I3}\vec{1_z} \\ F_v &= f_{v1}\vec{1_x} + f_{v2}\vec{1_y} + f_{v3}\vec{1_z} \end{aligned} \tag{3.5.21}$$

The resulting time averaged Navier-Stokes equations for the absolute velocities in the relative rotating frame of reference are defined as:

$$X = \begin{bmatrix} \bar{\rho} \\ \bar{\rho}\tilde{v_1} \\ \bar{\rho}\tilde{v_2} \\ \bar{\rho}\tilde{v_3} \\ \bar{\rho}\tilde{E} \end{bmatrix} \tag{3.5.22}$$

$$F_{Ii} = \begin{bmatrix} \bar{\rho}\tilde{w_i} \\ \bar{p^*}\delta_{1i} + \bar{\rho}\tilde{w_i}\tilde{w_i}\tilde{v_1} \\ \bar{p^*}\delta_{2i} + \bar{\rho}\tilde{w_i}\tilde{w_i}\tilde{v_2} \\ \bar{p^*}\delta_{3i} + \bar{\rho}\tilde{w_i}\tilde{w_i}\tilde{v_3} \\ \bar{\rho}\tilde{E}\tilde{w_i} + \bar{p^*}\tilde{v_i} \end{bmatrix} \tag{3.5.23}$$

$$-F_{Vi} = \begin{bmatrix} 0 \\ \tau_{i1} \\ \tau_{i2} \\ \tau_{i3} \\ q_i + \tilde{v_j}\tau_{ij} \end{bmatrix} \tag{3.5.24}$$

The shorthand notation, i, in the expression for $-F_{Vi}$ denotes derivatives with respect to x_i. Both the relative and absolute velocity vectors are involved in this expression.

The source term vector is defined as:

$$Q = \begin{bmatrix} 0 \\ -\bar{\rho}(\vec{\omega} \times \vec{\tilde{v}}) \\ 0 \end{bmatrix} \tag{3.5.25}$$

When equation (3.5.25), is compared to equation (3.5.19) one can see the relative velocity component being multiplied to the squared angular velocity has now been removed, thus eliminating the excess artificial dissipation in the far field region (where the angular velocity that is squared can become very large).

Lastly the stress tensor is now given by

$$\tau_{ij} = (\mu + \mu_t)\left[\frac{\partial \tilde{v_i}}{\partial x_j} + \frac{\partial \tilde{v_j}}{\partial x_i} - \frac{2}{3}(\nabla\vec{v}\delta_{ij})\right] \tag{3.5.26}$$

Chapter 4

Experimental evaluation

4.1 Introduction

The aim of the work detailed in this chapter is to produce a data set of fan performance characteristics of the new fan blades that replicate the axial flow fan used by Bruneau (1994) and Stinnes (1998). This new data set would then provide reference experimental work for future analytical and computational design work. It also provided the student with fan performance data for his own computational analysis of the B2-fan. The fan test facility, experimental setup and processing procedures are discussed in this chapter.

4.2 Fan Test Facility

The measurement of fan performance characteristic was carried out in a fan test facility that conforms to the specifications of the British Standards, (BS 848 standards, 1980). This facility was designed by Venter (1990), for type A tests with a free inlet and outlet to the fan. A schematic layout of the fan test facility can be seen in Figure 4.1.

The mass flow rate through the facility is measured by means of an inlet bellmouth with a diameter of 1.008 m (1). This is accomplished by measuring the difference in static pressure in the bellmouth relative to that of the atmosphere. A throttling device (3) with six opposed blades is used to control the volume flow rate. Flow straighteners are installed upstream (2) and downstream (4) of the throttling device to aid in smoothing the air flow. To neutralize the pressure losses due to all the various components in the flow system, a six-bladed auxiliary fan (5) is installed. The auxiliary fan has an outside diameter of 1.540 m and a set of flow straighteners (6) is installed downstream to eliminate swirl introduced by the fan rotor. To distribute the air flow more uniformly, flow guide vanes (7) are installed at the inlet of the settling chamber (8). In-

side the settling chamber (dimensions 3.7 m × 3.7 m × 7 m) three stainless steel mesh screens (9), which differ in coarseness, are installed to provide a uniform flow velocity profile to the inlet of the test fan (10). The fan test facility at the University of Stellenbosch differs from the (BS 848 standards, 1980) fan test code in the sense that the hydraulic motor (11) that drives the fan is situated on the outside of the settling chamber instead of inside. This setup provides the opportunity to use a stable motor mount that is rigid enough to eliminate most of the deviations at the design speed and allows for fine tip clearances to be used on the test fans. Meyer (1996) showed that the change in the position of the hydraulic motor has no discernible effect on the fan performance characteristics.

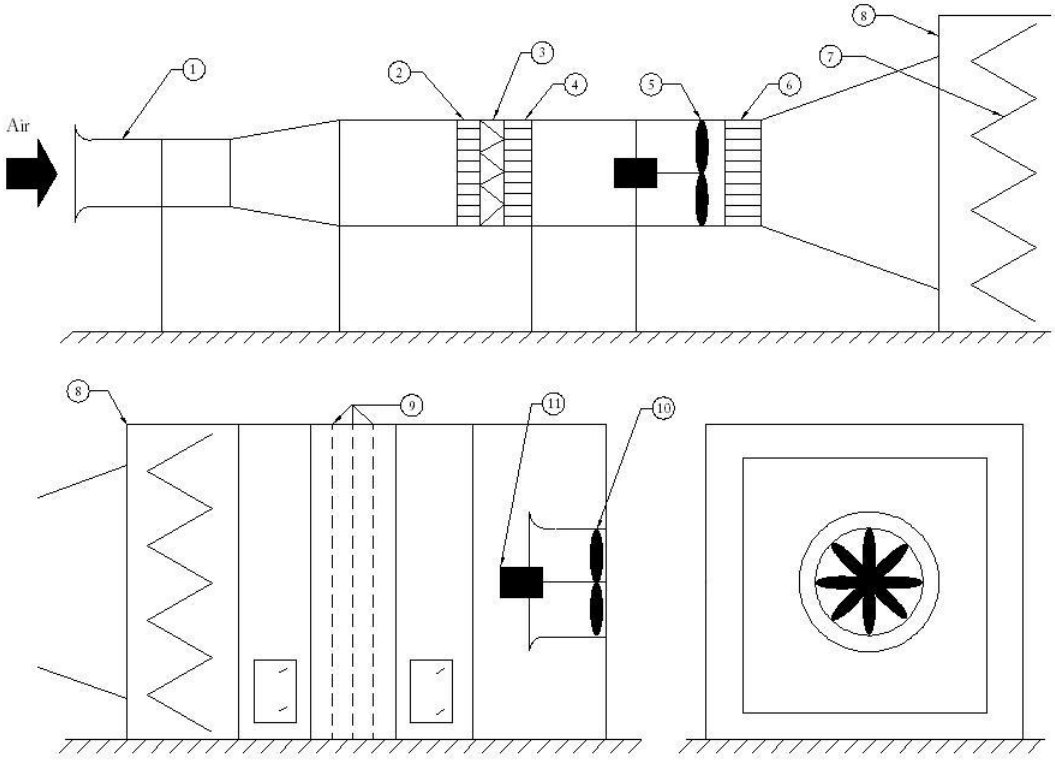

Figure 4.1: BS 848 Fan Test Facility, Stinnes (1998).

4.3 Experimental setup parameters

Bruneau (1994) found no significant difference in fan performance between using a hemispherical nose cone and a flat plate to cover the front of the hub. For simplicity in the numerical model it was decided to complete the experimental work with a flat plate attached to the hub. This flat plate extends upstream

to the face of the shroud flange, such as the one used by Stinnes (1998) and consists of a cardboard disk covering the spokes of the hub, such as used by Bruneau (1994). Special attention was paid to the following parameters:

4.3.1 Fan axis position

This experimental setup utilized the same frame used by Bruneau (1994), Meyer (1996) and Meyer (2000). The axial position of the fan inside the shroud was unchanged, with the inlet face of the hub flush with the inlet face of the shroud annulus. Changing the fan axis within a distance range from 0 m to 0.075 m, Meyer (1996) noted no effect on the fan static pressure rise for flow rates higher than $8\,m^3/s$. For lower air flow rates a slight decrease in the static pressure rise accompanied with a decrease in fan power resulted in unchanged fan static efficiencies. After every blade angle and/or tip clearance adjustment the fan was centred circumferentially inside the shroud.

4.3.2 Blade angle

The blade stagger angle was set using a custom-made jig that held a digital projector in place that measured the blade setting angle. This custom jig would be placed at the root of the blade and the blade angle would be set with the fan installed in the test facility. The B2-fan was originally designed with on-site blade angle adjustment in mind. The blade setting angle was defined relative to the blade chord at a 4.2° offset from the stagger angle, as described in Appendix D Section D.6. With reference to Bruneau (1994) the blades were set at an angle from the plane perpendicular to the axis of rotation. Stinnes (1998) used the complementary angle to this that coincided with Venter (1990), although Venter set the blade angle at the tip of the blade.

To set the blade angle the corresponding blade was locked into a horizontal position with the clamping device. After loosening both the lock nut and the grub screw the fan was tilted until the correct reading from the digital projector was obtained. Using a digital projector allowed very fine blade angle adjustment up to 0.1°. The position was locked by first tightening the grub screw and then the lock nut. This order was followed to prevent the blade shaft from turning when the lock nut is tightened.

4.3.3 Tip clearance

The tip clearance is set with the use of a feeler gauge propped in-between the blade and the shroud. The process of setting the tip clearance with the B2-fan can be accomplished with high accuracy due to the design of the B2-fan hub. A threaded collar protrudes from the hub and presses against a small lip on the root of the blade. This collar is adjusted until the desired tip clearance is

achieved. The collar is locked in place with a lock nut.

After setting the tip clearance of all the blades the shaft was released from the locking device and the tip clearance was checked at various positions around the shroud. This ensures that the fan shaft is centred in the shroud. If there were any deviations from the desired tip clearance the process was repeated.

An attempt was made to run experiments at the 1 mm to 1.5 mm tip clearance used by Stinnes (1998), but the fan blades interfered with the shroud in the upper right sector of the shroud. This was due to the frame oscillating at higher speeds, as a result of the frame not being stable enough to limit rotor circumferential movement. It is believed that the frame that Stinnes (1998) used was more rigid. The experiments were carried out at a tip clearance of 3 mm, with reference to Bruneau (1994). The experiments were carried out at 700 rpm, which was found to be the maximum safe rotational speed at which the oscillation of the motor frame did not cause the blades to touch the shroud.

4.3.4 Root seals

Bruneau (1994) provided data illustrating an increase in fan static pressure rise and an accompanying higher fan static efficiency when root seals were applied in contrast to not using root seals between the blade and the hub. In order to provide firm root seals and keep some flexibility for when blade angles were set, expandable foam was used to construct the root seals. The foam adhered to both the base of the blade surface and the hub surface, thereby giving a 100 % closed seal from the leading edge to the trailing edge. After allowing the foam to dry and set, excess foam was carefully removed and the root seal was shaped to the contour of the blade. The outside surface of the shaped foam was given a silicone layer to further seal the microscopic gaps and provide a smoothed closed seal. The 1° angle adjustment in both directions from 59° (the angle at which the foam was applied) was small enough for the flexibility of the foam to allow the adjustment without shearing loose. It should be mentioned that setting the blade at any greater angle would result in the expandable foam shearing at either the hub or bottom of the blade surface.

4.4 Experiment

Experiments were performed to measure static pressure (at the inlet bellmouth and at the settling chamber), rotational speed and the fan shaft torque. Different blade angles as well as tip clearances were evaluated. To asses very low volumetric flow rates (particularly with numerical work in mind), the throttling device was closed beyond the lowest setting point. This provided experimental data at a volumetric flow rate point of about 1.1 m^3/s, well beyond

the $\pm$ 3.6 m^3/s value of Bruneau (1994) and Stinnes (1998). Special care has been taken in all cases of instrumentation calibration. Pressure transducer calibration was repeated at different time periods yielding almost no difference in calibration value. To account for the speed fluctuating when no load is applied during calibration, a wooden brake was applied to the shaft. Again no discernible differences were noted. The torque transducer was calibrated numerous times and the calibration constant of $M = 27.325\,\mathrm{V} - 0.026$ corresponds well with that of Stinnes (1998), being $M = 27.527\,42\,\mathrm{V}$. In addition leakage tests were done on all the tubes connecting the pressure transducers and no leaks were found.

To aid investigation of the velocity profile over the blade surfaces, small tufts were attached to the suction side surface of one of the blades. The effect of the air flow over the blade surface on these tufts was captured by camera. The details of this investigation and results thereof are discussed further in Chapter 5.

4.5 Data Processing

Fan static pressure rise, fan power consumption and the fan static efficiency against volumetric flow rate are used to produce curves of the results for the performance mapping of the axial flow fan.

The BS 848 standards (1980) defines the fan static pressure rise as the static pressure at the outlet minus the total pressure at the inlet:

$$\begin{aligned} p_{Fs} &= p_{amb} - (p_{s_{sett}} + p_{d_{sett}}) \\ &= \Delta p_{s_{sett}} - p_{d_{sett}} \end{aligned} \tag{4.5.1}$$

4.6 Results

4.6.1 Repeatability

Providing good repeatable experimental results creates trust in the ability of the experimental facility to reproduce accurate experimental results when reinstating experimental setups. In terms of repeatability, excellent agreement was found for each of the three fan performance characteristics, as can be seen in Figures 4.2, 4.3 and 4.4, respectively.

Comparative figures for blade angles 59°, 58° and 60° can be found in Appendix F.

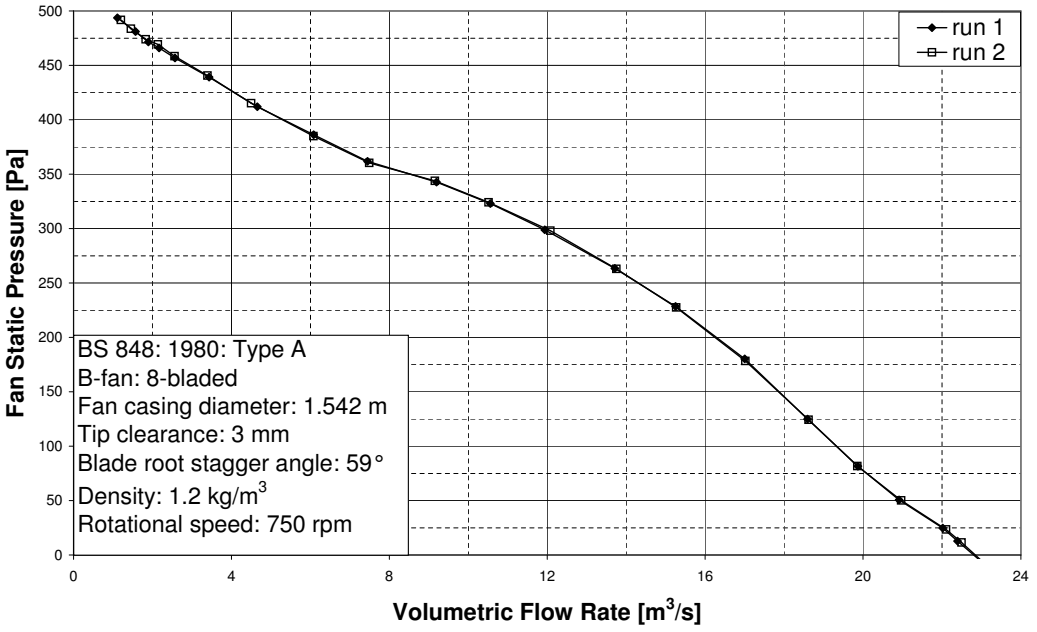

Figure 4.2: Fan static pressure rise, repeatability.

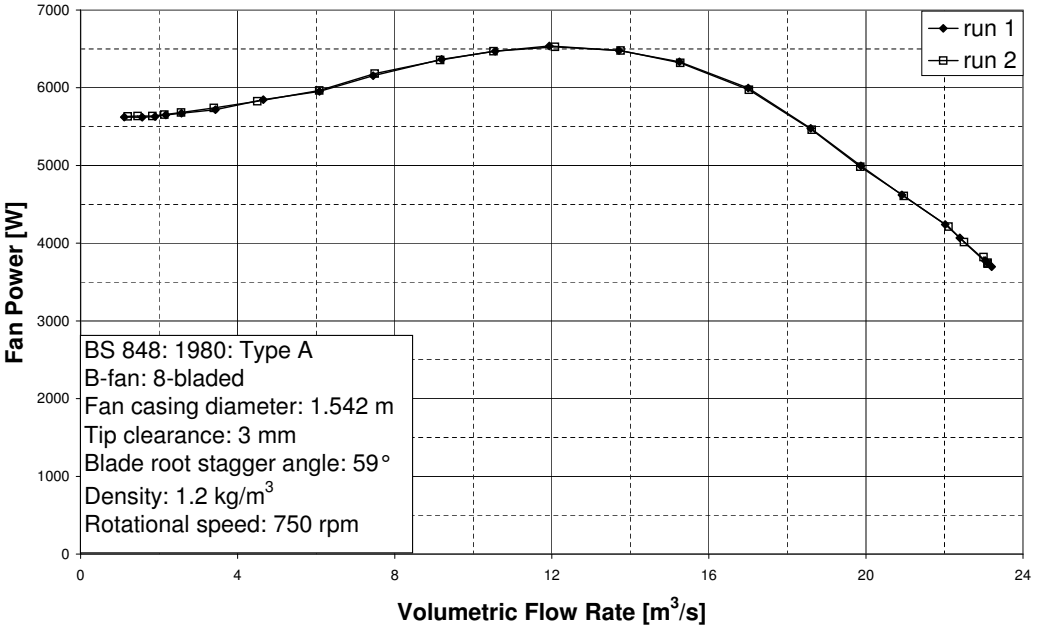

Figure 4.3: Fan power, repeatability.

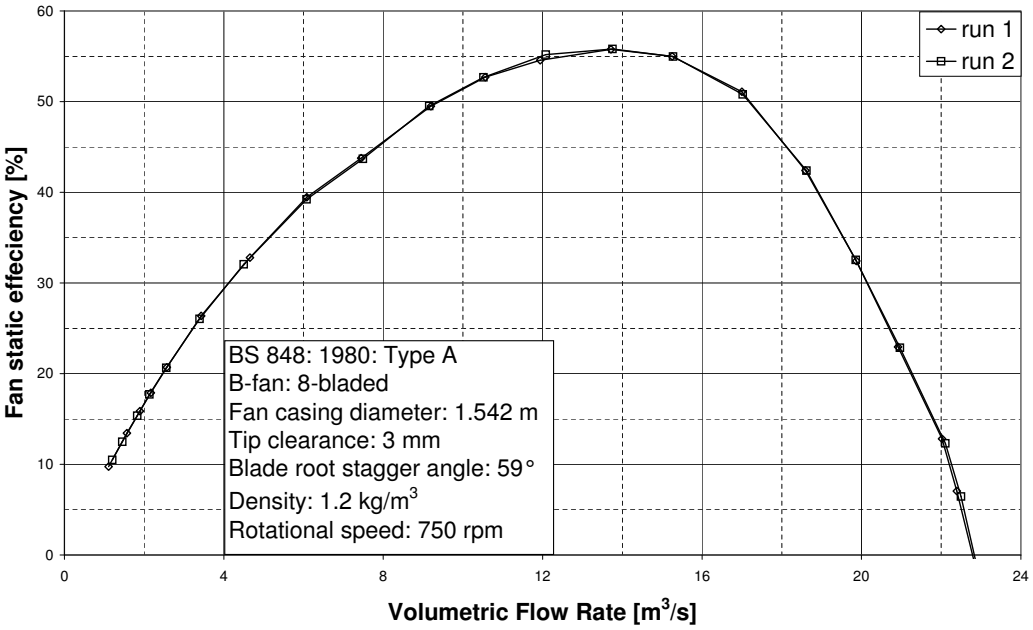

Figure 4.4: Fan static efficiency, repeatability.

4.6.2 Comparison with previous work

A comparison of the performance mapping for the fan characteristic static pressure rise, power and static efficiency is illustrated in Figures 4.5, 4.6 and 4.7, respectively.

In comparing the fan performance characteristics to that of Stinnes (1998) fair agreement is found. Stinnes (1998) did measure higher fan static pressure rise as well as a lower fan power input, which resulted in higher fan static efficiency. By examining Figure 4.5 it is clear that there is an almost constant difference between the corresponding angles. For the data range between $10\,m^3/s$ and $14\,m^3/s$ the data from this investigation seem to have a 1° off-set from the data of Stinnes (1998). If this was the case, then beyond this range (to the lower and higher flow rates) the static pressure rise of Stinnes (1998) would seem to decrease. Looking at Figures F.4, F.7 and F.10 it can be seen that the curve shape of Stinnes (1998) is not as uniform and smooth as that of this investigation.

Figure 4.6 shows that the values for fan power at corresponding angles do agree, albeit only at very high volumetric flow rates, with the deviation in fan power increasing at lower volumetric flow rates.

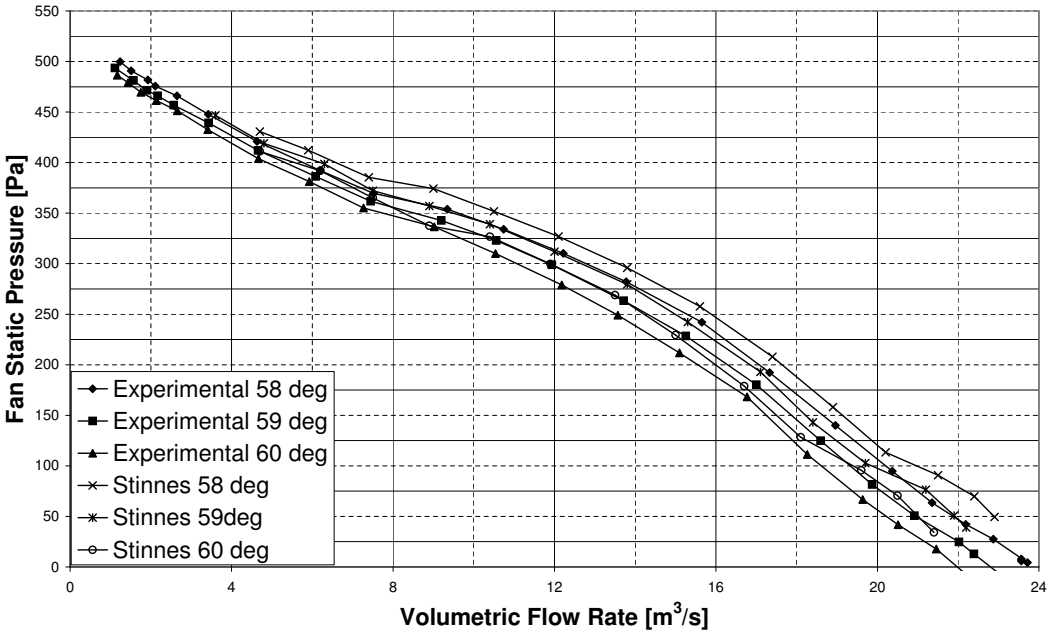

Figure 4.5: Fan static pressure rise, comparison with Stinnes (1998).

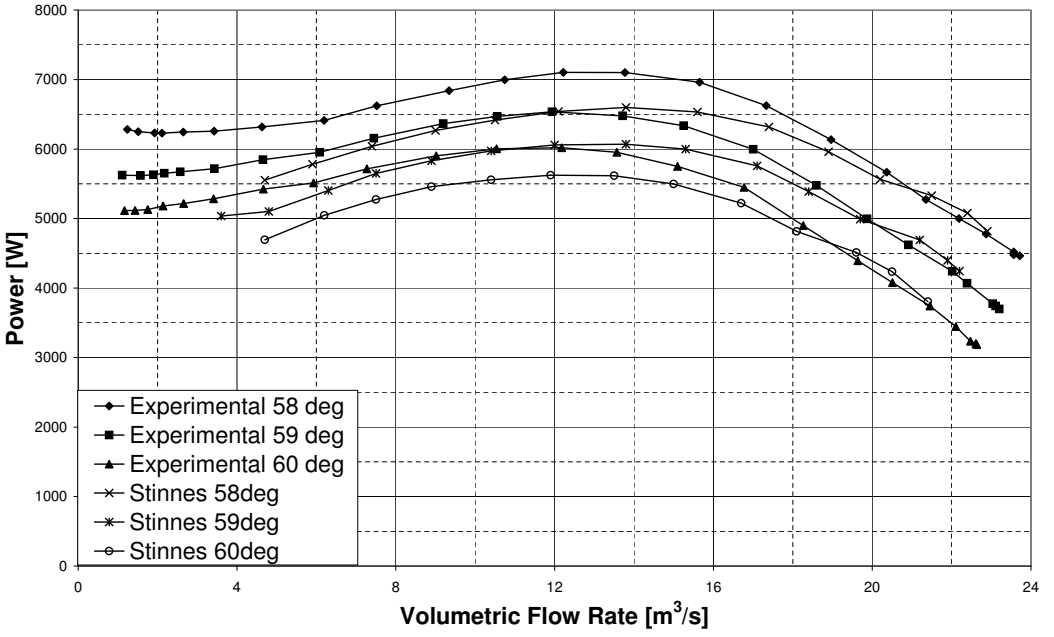

Figure 4.6: Fan power, comparison with Stinnes (1998).

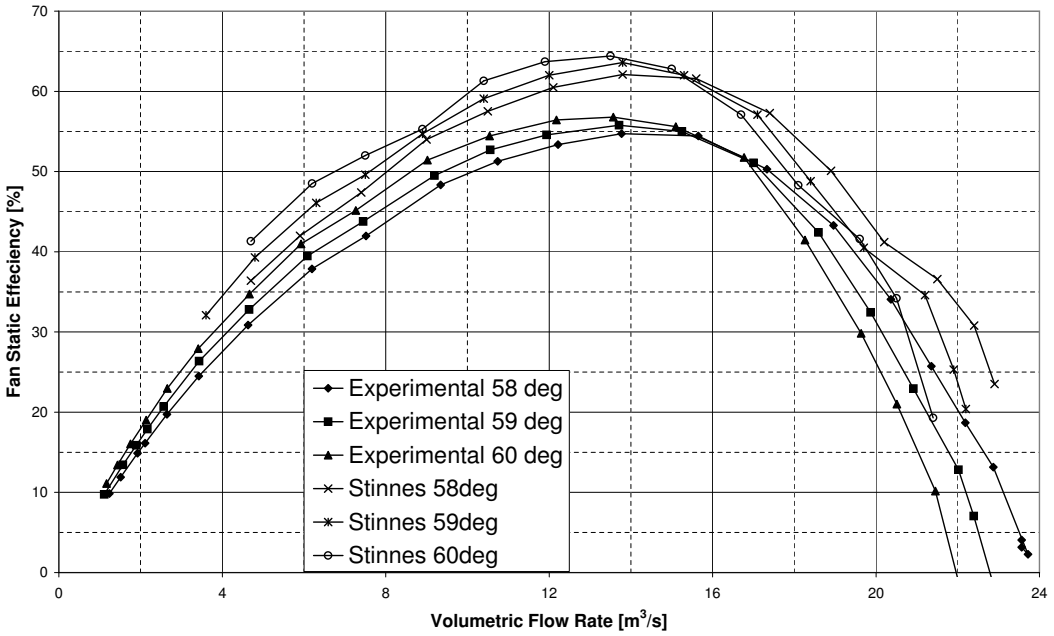

Figure 4.7: Fan static efficiency, comparison with Stinnes (1998).

The aforementioned discrepancies of lower static pressures and higher fan power lead to lower fan static efficiencies than that of Stinnes (1998). A test was carried out with a tip clearance of 1.5 mm which provided very good agreement with that of Stinnes (1998), but the tests where carried out too late in the day resulting in poor repeatability in torque readings due to higher temperatures. The results where discarded. Further attempts to test at this small tip clearance resulted in the fan blades interfering with the shroud. In order to protect the fan blades it was decided not the run any further tests at this small tip clearance and further tests were carried out at a 3 mm tip clearance. From the discussion above and the resulting figures it is fair to assume that the increased fan performance characteristics of Stinnes (1998) is due to his experiments being carried out at a 1 mm to 1.5 mm tip clearance. The 1.5 mm tip clearance results can be viewed in Appendix F.

Figures of the fan performance characteristics for the three different blade angles mentioned above without comparison to Stinnes (1998), giving a better view of the shape of the curves can be found in Appendix F.

4.7 Conclusion

The aim of gaining knowledge of the fan test facility and collecting data of the B2-fan for use in computational analysis was achieved. Unfortunately whether this provides good reference experimental work for future analysis and computational design work remains debatable. Only fair agreement was obtained when comparing the fan performance characteristics to that of Stinnes (1998). The trend of the curves are more uniform and smooth than those of Stinnes (1998), but the quantitative results are below the reference fan performance characteristics.

There are some factors that cannot be neglected when comparing the results to previous work:

- A different, less sturdy frame than that of Stinnes (1998) was used. The frame used by Stinnes (1998) had the additional benefit that the machined shroud was secured to the frame, preventing any independent movement of the shroud from that of the frame as is the case with the current frame. This allowed Stinnes (1998) to test at a very small tip clearance of 1 mm to 1.5 mm. Before the blades interfered with the shroud, good agreement with the results of Stinnes (1998) were found when tests were carried out at 1.5 mm tip clearance, confirming the importance of tip clearance effect on fan performance characteristics.

- The fan blades used in this experimental setup are not the same fan blades used by Bruneau (1994), Stinnes (1998) and Meyer (1996). Sadly, that set of blades was destroyed before this project was initiated, resulting in a different set of blades that had to be produced to be used in the test facility. It should however be noted that the new blades were produced from the same moulds as the previous blades.

- The new blades have a rougher surface finish than the previous blades. This adds to performance losses due to surface drag as well as irregularities on the blade surface that may induce early stall at some volumetric flow rates.

Chapter 5

CFD validation with experimental data

5.1 Introduction

The aim of this chapter is to compare the outcome of the CFD analysis of an axial flow fan with the performance curve obtained from a fan test facility conforming to the BS 848 standards (1980) as well as discuss relevent findings on different simulation techniques. Additional work was done to visualize the flow field across a single blade surface at four different flow settings by using black wool tufts. This experiment is discussed in detail and results are provided.

5.2 Fan performance curve

The fan performance curve obtained from the fan test facility provides a means to verify and validate the accuracy and integrity of the CFD simulation. This was done firstly to produce a new data set for the newly manufactured fan blades and secondly to afford the student more insight into the operation of the axial flow fan in practical use, especially in terms of the manner in which the air flow exits the fan rotor. This knowledge was deemed important in analysing the streamlines of the CFD computations.

Two CFD models are compared with experimental data. The first model incorporates a pinch at the outlet boundary to reduce the amount of backflow over the boundary by effectively increasing the axial velocity. A zero-shear wall is used for the circumferential boundary surface at the outlet. This model is referred to as Approach-1. The second model has no pinch at the outlet boundary and the zero-shear wall boundary is replaced by a second outlet boundary. This model is referred to as Approach-2.

Figure 5.1 shows the comparison of fan static pressure rise between the CFD analysis and the experimental data. The two different approaches are compared side by side with experimental data obtained at 3 mm tip clearance. Both outlets give exceptional agreement at the design operating point (16 m^3/s) with the experimental data obtained by the student. The CFD results also compare very well at higher flow rates and the deviation between the two models is small. At lower flow rates the models deviate from each other as well as from the experimentally measured data. At the lower flow rates Approach-1 over-predicts contrary to Approach-2. Near 10 m^3/s, close to blade stall, Approach-2 compares more favourably than Approach-1. In the range of 4 m^3/s to 6 m^3/s Approach-2 is extremely unstable, to such an extent that the simulation diverged. The data point for 8 m^3/s, although not diverging, did not converge fully.

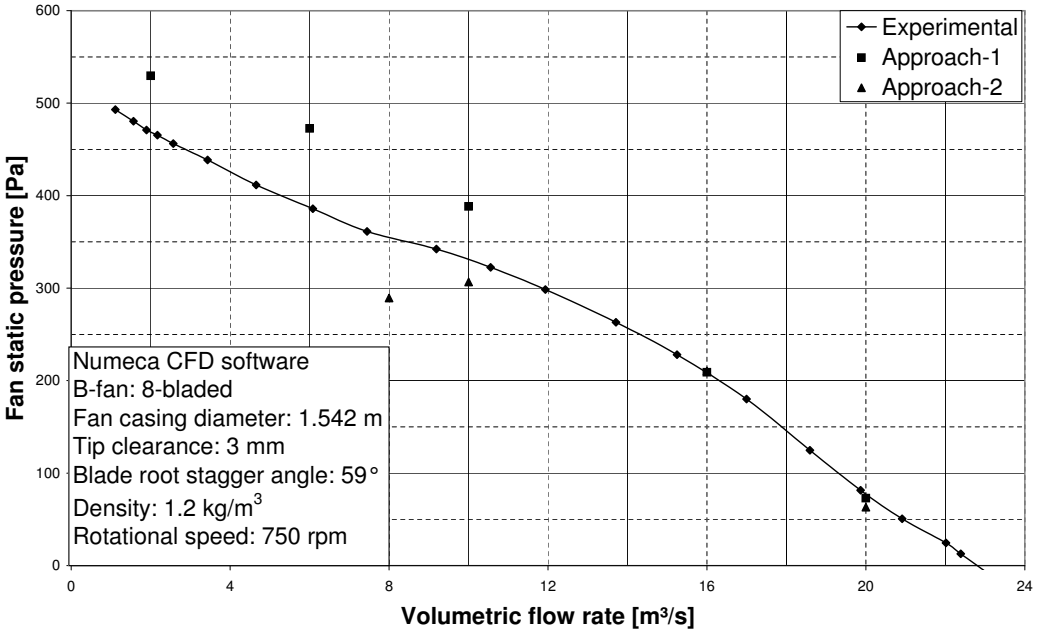

Figure 5.1: Fan static pressure rise, CFD verification.

Figure 5.2 shows the comparison of fan power between the CFD analysis and the experimental data. The deviation of the CFD results for both models from experimental data can be attributed to the fact that the CFD models cannot accommodate frictional losses from fan shaft bearings. Even though a no load torque test was performed in the calibration stage, this was a static test and the frictional forces from the bearings due to axial loading of the fan rotor during operation is not accounted for. Both CFD models show exceptional trendline

agreement to the experimental data measured by the student at volumetric flow rates higher than 16 m^3/s, albeit at a constant difference.

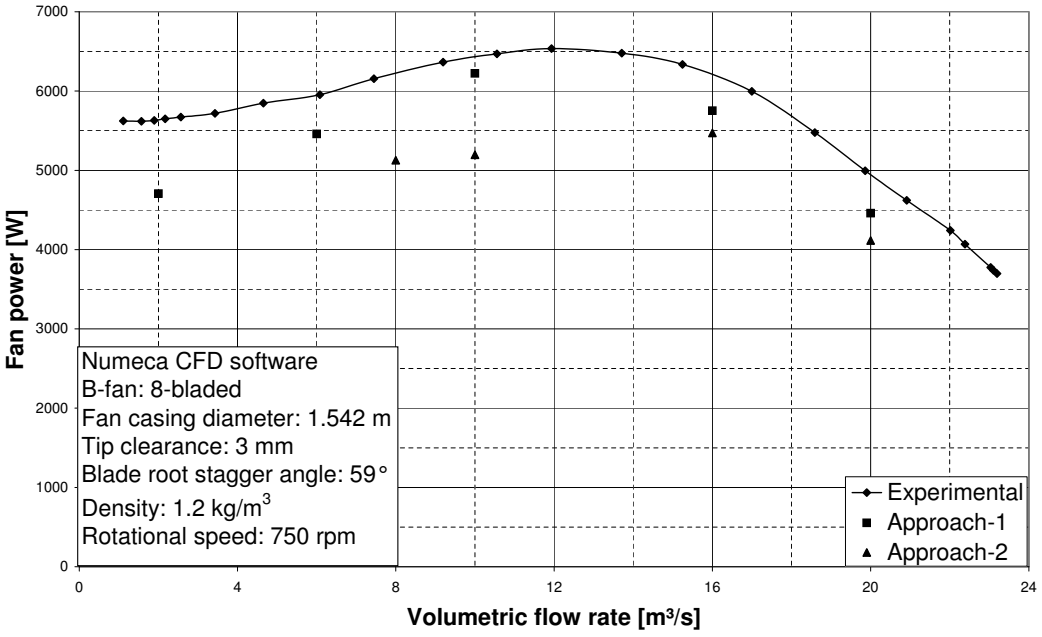

Figure 5.2: Fan power, CFD verification.

Figure 5.3 shows the comparison of fan static efficiency between the CFD analysis and the experimental data. The fan static efficiency is a direct function of the fan static pressure rise and fan power. Thus the deviations from the experimental data as discussed above are directly transferred to the fan static efficiency. The CFD results agree favourably with the experimental results as measured by the student at 20 m^3/s and show good trendline agreement at a volumetric flow rate of 10 m^3/s to 16 m^3/s.

Tables providing the data obtained through the simulation of the two CFD models are presented in Appendix G.

5.3 Transition

A boundary layer starting as laminar flow and converting to fully turbulent flow goes through a stage in the flow process called transition. According to White (2006) transition can take place through any of the following three processes: natural transition, bypass transition and separated-flow transition. Transition

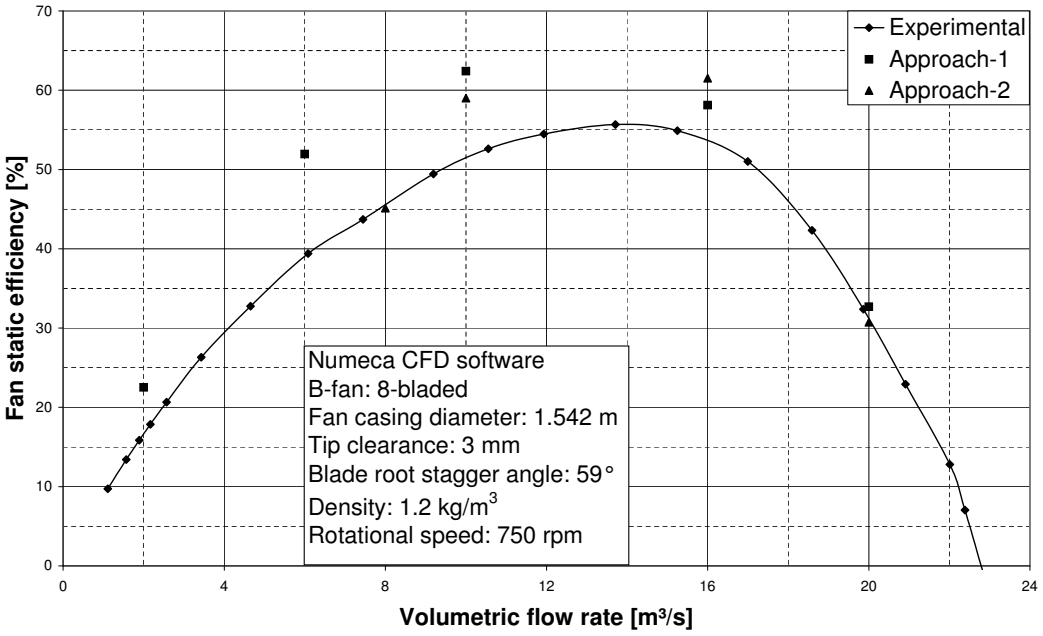

Figure 5.3: Fan static efficiency, CFD verification.

is a very complicated phenomenon typically influenced by the Reynolds number, free stream turbulence intensity, surface roughness, shape factor and the pressure gradient over the surface. White (2006) also mentions that no fundamental theory for transition exists and that the prediction of transitional onset is carried out through experiments and correlations.

FINE™ allows the user to add a transition model to the Spalar-Allmaras turbulence model. The onset of transition can either be user defined by an educated guess or predicted by the Abu-Ghannam and Shaw (AGS) model. Since accurately predicting the onset of transition is beyond the scope of this thesis, the latter option was employed. The turbulence model applied by FINE™ uses an intermittency factor. The intermittency factor defines the time during which the flow over any point on the surface is fully turbulent and has a range from zero, for fully laminar flow, to one for fully turbulent flow. The intermittency is calculated at every point on the surface, at each iteration (FINE™/Turbo Manual, 2007b). The transitional model is incorporated into the Spalart-Allmaras turbulence model by multiplying the turbulence production term with the intermittency factor.

The AGS model uses empirical relations derived from experimental data for transition on a flat plate with pressure gradients. The model predicts the onset of transition at a "momentum thickness Reynolds" number that is exponen-

tially dependent on a function of a dimensionless pressure gradient. The sign of the dimensionless pressure gradient depends on whether the pressure gradient is adverse or favourable. For an adverse pressure gradient the transition is promoted and for a favourable pressure gradient the onset of transition is retarded.

Incorporating the transition model for the Spalart-Allmaras model had no discernable effect on fan performance prediction of either the design operating point or at a very low flow rate. The investigation on the effect of the transition model on fan performance for the latter case was spawned from the indication that the fan blade operates in a Reynolds number range of 200 000 to 700 000. At 16 m^3/s the difference in fan static pressure rise for the Spalart-Allmaras model with and without transition is 0.019 % and at 2 m^3/s the difference is 0.427 %.

5.4 Investigation of streamline distribution

Investigating the streamline distribution along the domain length indicates whether the CFD analysis gives a true representation of the actual flow field produced by the fan blade. Figure 5.4 shows the streamline distribution at the design operating point for Approach-1. The extent of radial flow depicted here is not realistic, since during the experimental work no air flow is experienced when standing adjacent the fan exit at the design operating point. Large recirculation cells can clearly be seen in the flow outlet domain of the fan.

The governing equations for rotating systems are usually solved for relative velocity components in the relative reference frame. Solving the absolute velocity components in the relative reference frame should lead to the same flow solution. However it was found that by rather solving the latter case for the axial flow fan greatly improved the streamline distribution. The problem with the former case is that at far field locations the relative velocity may become very high, creating excess artificial dissipation. According to the FINE™/Turbo Manual (2007*b*) this excess artificial dissipation leads to non-physical rotational flow in the far field region. Figure 5.5 shows the improvement on the streamline distribution of the inlet for the simulation where the absolute velocity is solved in the relative reference frame. No recirculation cells are present in the inlet upstream of the bellmouth as would be expected from the uniform inflow provided by the mesh screens and settling chamber design of the fan test facility. Unfortunately the unrealistic radial outflow distribution is still evident.

A vast improvement in streamline distribution is apparent from Figure 5.6, which shows the streamline distribution at the design operating point for Approach-2. The streamlines are evenly spaced and no radial outflow from

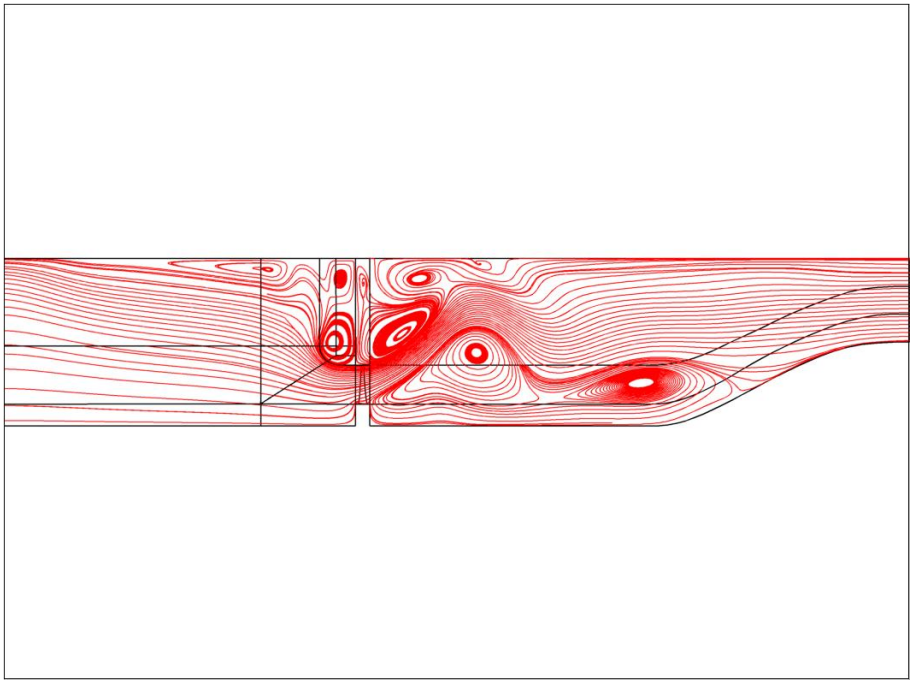

Figure 5.4: Streamline distribution, 16 m^3/s, Approach-1, relative velocity solution.

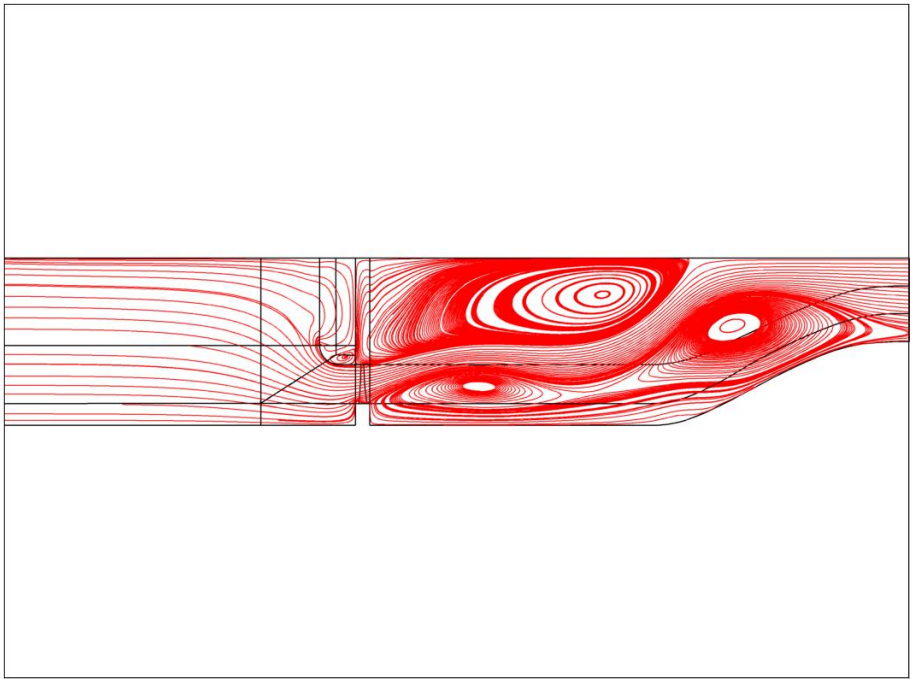

Figure 5.5: Streamline distribution, 16 m^3/s, Approach-1, absolute velocity solution.

the fan rotor is evident at the fan outlet, which agrees with the actual setup. Air inflow from the circumferential outlet boundary can also be seen.

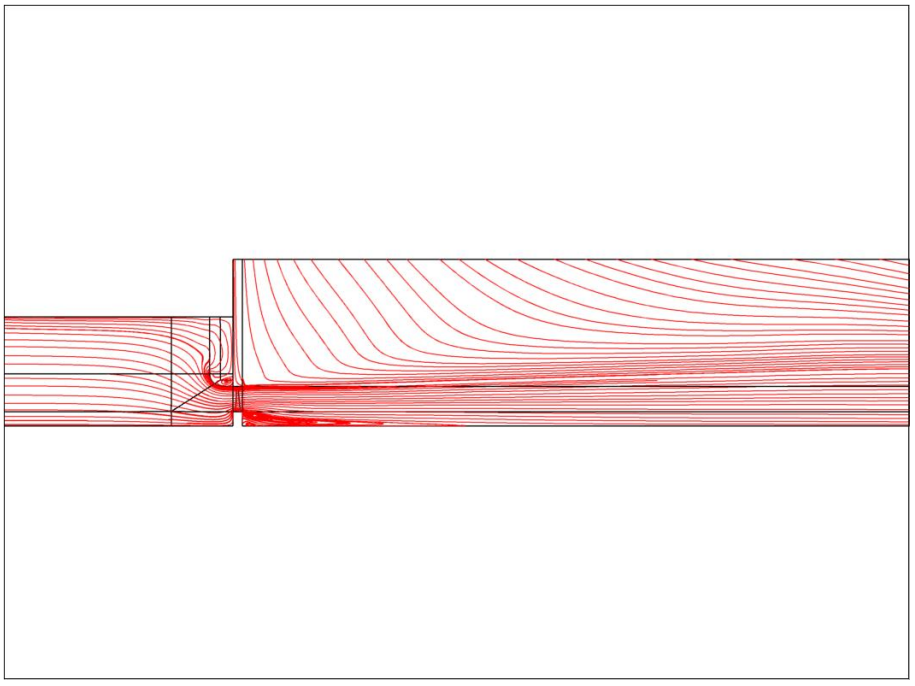

Figure 5.6: Streamline distribution, 16 m^3/s, Approach-2, absolute velocity solution.

Figure 5.7 gives a close-up view of the streamline distribution across the blade for both CFD models. The uncharacteristically high radial outflow of Approach-1 is in clear contrast to the axial outflow of Approach-2. The streamline distribution is an important aspect that will be used in the investigation of the inlet relative velocity for the two-dimensional profile sections employed in the ADM. At the design operating point the ADM compares very well with experimental data, while employing no radial flow component in the momentum source terms. The "no radial flow assumption" of the ADM correlates favourably with the streamline distribution of Figure 5.7(b).

It is assumed that the instability of the $8\,m^3/s$ simulation is largely due to the recirculation cells at the inlet to the blade towards the tip radius, the large separation at the hub inlet to the fan blade and the large amount of back flow at the trailing edge of the fan blade near the hub (Figure 5.8). The amount of turbulence produced by the recirculation cells near the tip radius is the most probable cause of unsteadiness of this particular simulation.

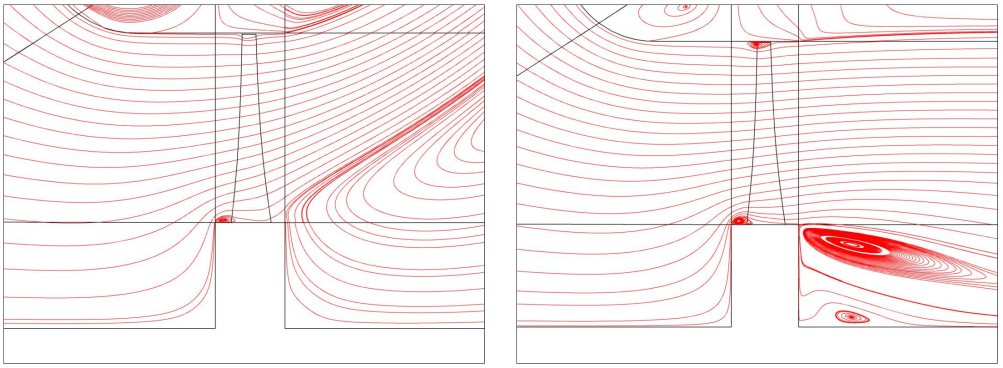

(a) Streamline distribution, 16 m^3/s, Approach-1, close-up.

(b) Streamline distribution, 16 m^3/s, Approach-2, close-up.

Figure 5.7: Streamline distribution close-up views for Approach-1 and Approach-2.

The streamline distribution diagrams for the remaining CFD data points on Figures 5.1 to 5.3 are presented in Appendix H.

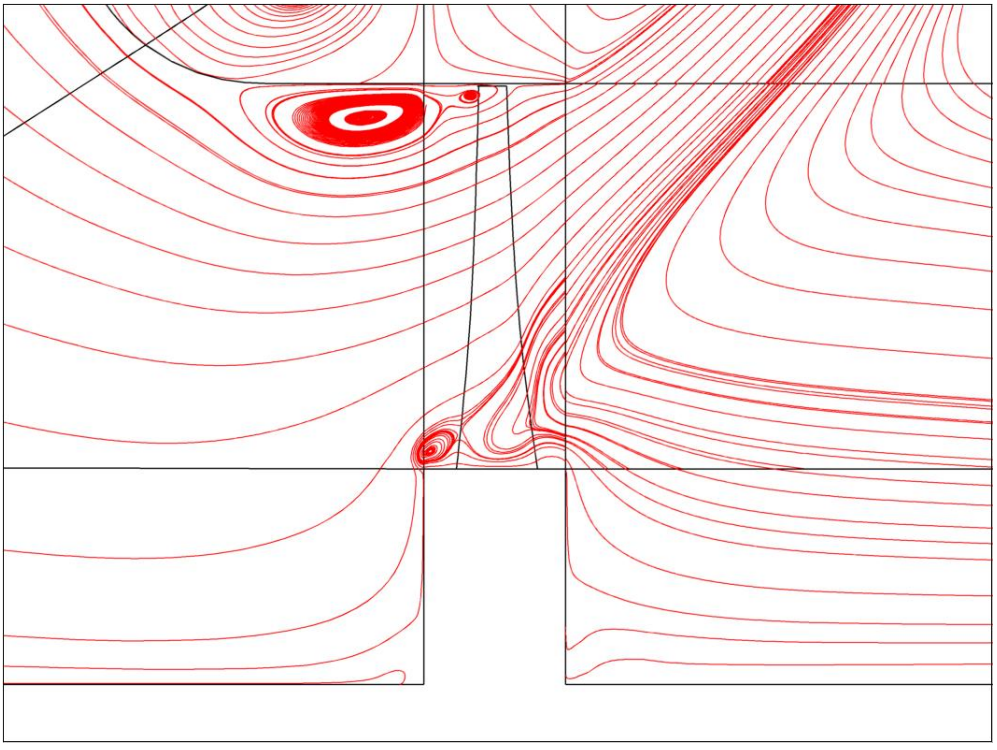

Figure 5.8: Streamline distribution, 8 m^3/s, Approach-2, close-up view.

5.5 Flow pattern visualization

Additional work has been performed by investigating the flow pattern across the blade length. This is essential for future inquiry into the shape of the two-dimensional profile section to be used in the ADM. It is assumed that at lower flow rates the increase in radial flow requires the two-dimensional profile to slant radially and align itself with the inlet relative velocity. In doing this the chord length of the particular profile is effectively lengthened, which would result in different momentum source terms, contrary to the linearly decreasing chord lengths of the vertically aligned radially stacked profiles used by current ADM's.

To validate the flow pattern output from the CFD model, small tufts of wool were used to capture the flow pattern on the experimental blades. The blade surface was divided (radially) into ten rows containing five tufts each. A very light and thin string of wool was used to construct the tufts, which were attached as close as possible to each other. Care was taken to ensure that no tufts interacted with one another. Since the tufts indicated an outwards deflection due to the centrifugal force exerted on them, only the change in deflection was considered when evaluating the occurrence of stall on the fan blades. A Lucas Dawe Ultrasonics Stobotorch (stroboscope) was used to visually slow down one blade and keep it stationary for an opportunity to take a photo of the fan blade flow pattern. To provide a good contrasting background for the stroboscope the particular blade containing the black tufts was lightly spray painted white and the experiment was carried out at night time. The flow pattern visualization experiment was carried out at 700 rpm, since at this stage there had already been an incident with blades connecting the shroud and the decision was made to run at a lower speed to avoid another accident that might result in a loss of the fan blades.

Figure 5.9(a) shows the flow pattern of a fully stalled blade. Towards the blade trailing edge there is no flow over the blade surface, as can be seen by the tufts only subjected to its own centrifugal force. The trailing edge of the blade is completely stalled from hub to tip. The flow over the leading edge is very unstable, typical of turbulent flow. It is not apparent from the photo, but while the experiment was undertaken at this point, one could clearly see the tuft at the hub near the leading edge flipping around to the pressure side of the blade and then back again. This is due to the presence of reverse flow at this point. The "stagnant" region on the blade surface indicated by the tufts is mirrored in Figure 5.9(b) by the flow field representation from the CFD analyses. The CFD does not predict stalling of the complete trailing edge. This means that a larger part of the blade surface is still effectively performing work on the fluid, according to the CFD. Once separation occur the lift force is restricted and the drag force increased (White, 2006). This would explain the higher fan

static pressure rise at lower flow rates predicted by the CFD model with the pinched outlet (Approach-1).

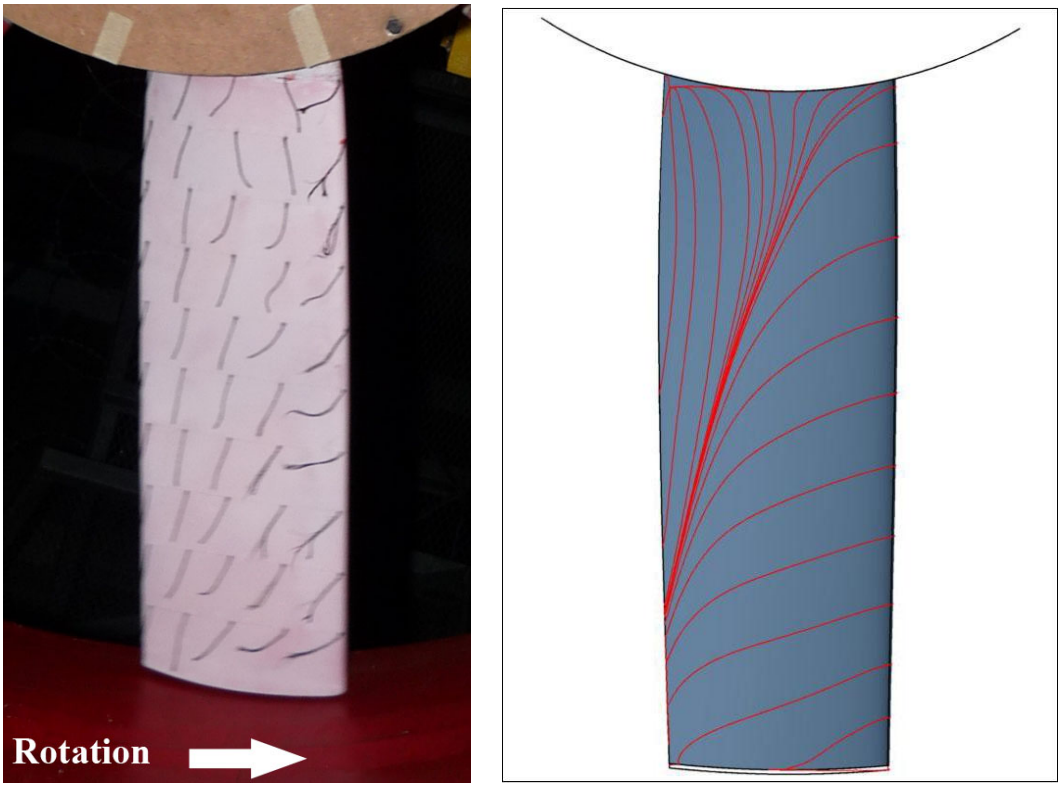

(a) Experimental fan blade flow pattern with throttle device closed.

(b) CFD fan blade flow pattern at 2 m^3/s (Approach-1).

Figure 5.9: Flow pattern visualization at 2 m^3/s.

In the operating range where it is assumed that fan blade stall begins, it is clear from Figure 5.10(a) that the blade starts stalling at the hub and towards the trailing edge. Between the hub radius and mean radius roughly 60 % of the blade is stalled. The CFD models replicate the stall region visible from the experiments. Comparing Figures 5.10(b) and 5.10(c) it is evident that the CFD model with the open outlet (Approach-2) predicts a larger stalled region. This explains the lower predicted pressure rise of Approach-2 as discussed in the previous paragraph.

(a) Experimental fan blade flow pattern at 10 m^3/s.

(b) CFD fan blade flow pattern at 10 m^3/s (Approach-1).

(c) CFD fan blade flow pattern at 10 m^3/s (Approach-2).

Figure 5.10: Flow pattern visualization at 10 m^3/s.

Figure 5.11(a) shows that at the design operating point, only a small portion of the blade near the hub trailing edge stalls. The stalled region is again replicated by the two CFD models. There is very little discrepancy between Figures 5.11(b) and 5.11(c). This is in line with the 0.684 % difference in predicted fan static pressure rise between the two models.

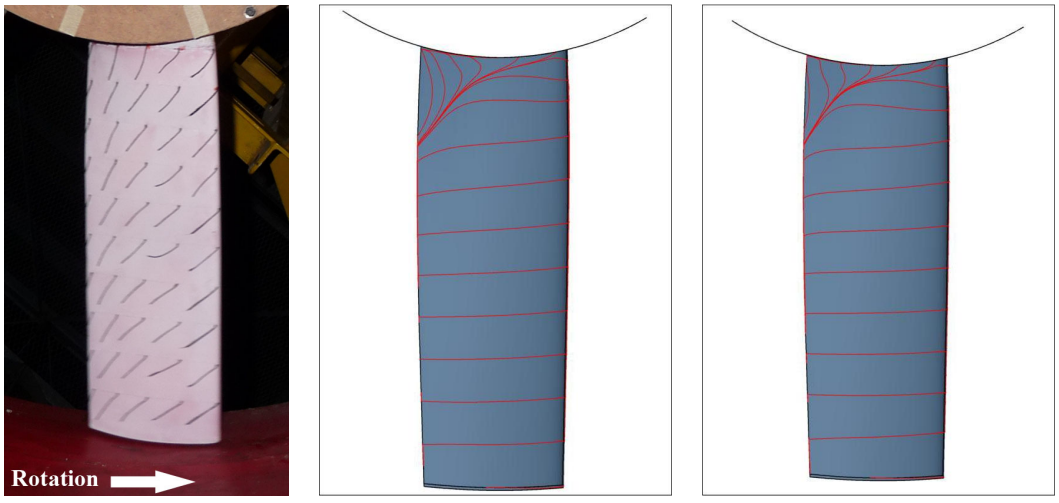

(a) Experimental fan blade flow pattern at 16 m^3/s.

(b) CFD fan blade flow pattern at 16 m^3/s (Approach-1).

(c) CFD fan blade flow pattern at 16 m^3/s (Approach-2.)

Figure 5.11: Flow pattern visualization at 16 m^3/s.

There is no stalling of the blade for the throttling device in the fully open position (Figure 5.12(a)). Figures 5.12(b) and 5.12(c) indicate that only the small region adjacent to the hub experiences separated airflow.

(a) Experimental fan blade flow pattern with throttle device fully open.

(b) CFD fan blade flow pattern at 20 m^3/s (Approach-1).

(c) CFD fan blade flow pattern at 20 m^3/s (Approach-2).

Figure 5.12: Flow pattern visualization at 20 m^3/s.

Chapter 6

Conclusion and recommendations

6.1 Motivation for study

Axial flow fans are rotary machines designed to provide a relatively low pressure rise at high flow rates. Their applications range from small scale building air ventilation and gas extraction to large scale process fluid cooling or condensation at power plants. The axial flow fan considered in this thesis is a $\frac{1}{6}^{th}$ scale version of the typical axial flow fans employed in direct air cooled heat exchangers at power generation plants, such as Matimba. These fans are utilized in arrays beneath the finned tube heat exchangers in an A-frame construction. The process fluid is cooled or condensed by the difference in temperature between the ambient temperature of the air flow that is moved through the heat exchanger bundles (by the axial flow fans) and the temperature of the finned tubes.

Efficient design of forced draught dry-cooled steam condenser sites result in large cost savings, considering the annual total power consumption of the axial flow fans. The Matimba power plant employs 288 axial flow fans, 9.145 m in diameter. CFD is a fast and relatively low cost design tool to investigate the system effects for such ACSC units. Unfortunately simulating the axial flow fans with full discrete rotating surfaces when numerically modelling the entire plant is computationally very expensive and simpler methods have been successfully used for ideal environments and system effects (Van Staden, 1996). The actuator disc method is commonly applied for such investigations. However, the ADM under-predicts fan performance at lower flow rates since it does not incorporate the effect of radial flow across the blade.

The aim of this dissertation is to model a single axial flow fan with three-dimensional rotating surfaces to capture the effects of radial flow over the fan blade at low flow rates. The knowledge gained will be utilized to amend the ADM. Verification with experimental work enforce confidence in the CFD

results. The dissertation aimed to produce a new database of fan performance data for the newly manufactured B2-fan blades.

6.2 Research findings

A new database of fan performance data was produced for the B2-fan. The experimental research results and main findings are discussed in Section 6.2.1. A discrete three-dimensional CFD model was produced and simulated with NUMECA CFD software. The numerical research results and main findings are discussed in Section 6.2.2.

6.2.1 Experimental

Extremely good repeatability was found between subsequent tests. A fan static pressure rise of 207.4 Pa at the design flow rate of 16 m^3/s was achieved. Stinnes (1998) achieved a higher fan static pressure rise at the design operating point, but tested the fan at a tip clearance of 1 mm to 1.5 mm. This was achieved by using a sturdier frame limiting the radial movement of the fan blades when the fan shaft starts to oscillate. In an attempt to recreate the fan performance data for a tip clearance of 1.5 mm the fan blades interfered with the shroud annulus. To preserve the fan blades the tip clearance was set back to 3 mm, which was deemed safer since a different frame to that used by Stinnes (1998) was utilized. The one set of fan performance characteristics obtained at 1.5 mm tip clearance compared well with the results obtained by Stinnes (1998) (Figures F.13 to F.15).

Most of the work done by the blade on the air is performed near the tip radius. The higher pressure on the pressure side of the blade causes the flow to leak through the tip clearance towards the lower pressure suction side along a flow path of least resistance. This phenomenon is termed a tip vortex, i.e. the air loss or leakage around the fan blade tip. Larger tip clearances leading to larger tip vortexes result in loss of performance in terms of pressure rise capability and airflow (Hudson Products Corporation, 2000).

The proposed method of Venter and Kröger (1992) for determining the effect of tip clearance on fan performance was used to establish the proposed fan static pressure rise achievable at a tip clearance of 1.5 mm. This method predicted a fan static pressure rise of 212 Pa, which correlates well with the measured fan static pressure rise of 216 Pa at 1.5 mm tip clearance.

All fan performance data curves follow a smooth trend line with no discernible irregularities observed throughout the volumetric flow rate range. This range is extended beyond the range of flow rate points tested by Bruneau (1994)

and Stinnes (1998). The importance of ambient temperature on the torque readings became apparent only after extensive calibration and recalibration of all experimental instrumentation. Testing in the early hours of the morning (typically two hours before sunrise) when there is no change in ambient temperature and no heating of the settling chamber by direct sunlight and radiation from surrounding window panes, vastly improved the repeatability of the torque readings and as such the fan power characteristic. Arriving at this conclusion involved at lot of testing and re-testing the B2-fan in the test facility.

Additionally an experiment was carried out to visualize the flow field over the fan blade suction side surface. This was achieved by running the fan at the different volumetric flow settings during the evening and letting one of the blades "become stationary" with the aid of a stroboscope. Photographs and videos were taken of the blade with a digital SLR camera. Good agreement was found in visualizing the stalled region in the flow field over the blade surface. With reference to the CFD streamline representation, the black wool tufts does not give a good indication of the flow field distribution in terms of flow angle, due to the effect of centrifugal forces. The strength and advantage from the tuft representation experiment lies in the ease of setting up the experiment and acquiring an indication of the extent of stall occuring on the blade surface. The examination of the difference between the tuft representation of the flow field and the flow field predicted by the CFD models provided better understanding of the difference in fan static pressure rise predicted at lower flow rates. From Figure 5.9(b) the large degree of radial flow experienced over the blade is evident. This confirms the need to amend the ADM to incorporate the effects of radial flow at lower flow rates.

6.2.2 Numerical Simulation

A $\frac{1}{8}^{th}$ axisymmetric model of the B2-fan was constructed using structured grid cells. The model developed from a learning curve that started with just modelling the fan blades in an annular pipe section and progressed to incorporate the full dimensions of the settling chamber as well as the bellmouth inlet to the fan rotor. Two different outlets were compared to correctly simulate a fan rotor exhausting into open atmosphere. Both models compared exceptionally well at the design operating flow rate as well as higher flow rates.

Approach-1 was developed based on the recommendations of the NUMECA support team to pinch the flow domain at the outlet boundary. The model is only allowed an outlet boundary on a plane normal to the fan axis. This method constricts the amount of backflow over the outlet boundary and improves the stability of the simulation. The fan performance curve obtained with this model deviated from experimental data at lower flow rates. The

streamline distribution of the model along the domain is not realistic. The recirculation cells in the inlet section, comprising of the settling chamber and bellmouth, was a particular point of concern.

Switching from the method of solving the relative velocity in the relative reference frame to one where the absolute velocity is solved in the relative reference frame resolved the streamline distribution issue in the inlet section. Unfortunately this resulted in a 10.7 % decrease in the predicted fan static pressure rise. The tuning of the amount of pinch applied at the outlet boundary that successfully eliminated any backflow over the outlet boundary was also lost. Pinching the outlet even more removed the new found backflow over the boundary, but resulted in a further adverse effect on the fan static pressure rise. For both cases the recirculation cells in the outlet sections remained.

Removing the pinch from the previous model resulted in a further 2.9 % decrease in fan static pressure rise. The zero-shear walls at the circumferential boundary in the outlet section still influenced the outflow from the fan by allowing recirculation cells to form. A separate investigation into this phenomenon showed that the longer the simulation ran, the stronger these recirculation cells became (adversely affecting the fan static pressure rise).

In the final CFD model (Approach-2) the zero-shear wall as well as the pinch was removed. The recirculation cells were eliminated and the fan static pressure rise was considerably improved. This model slightly over-predicts the fan static pressure rise at the design flow rate of 16 m^3/s by 1.4 %. A uniform streamline distribution along the computational domain was achieved with no radial flow over the blade at the design operating point. Previous attempts at simulating this particular outlet when solving the relative velocity in the relative reference frame failed.

Another issue identified within this research is the mixing losses introduced at the rotor-stator interfaces. The mixing losses over the rotor-stator interface can range anywhere from 10 Pa to 100 Pa, which is an order of magnitude of the pressure capability of the axial flow fan and influences the fan performance considerably.

6.3 Recommendations for future research

All effects were investigated for producing experimental fan performance data curves. For future test work to be carried out at the test facility at Stellenbosch University care should be taken regarding the time of the day that tests are conducted. A recommendation for future test work would be to use a ther-

mocouple to measure the temperature of the air going into the fan.

To facilitate in-depth research in tip clearance beyond the minimum tip clearance investigated by Venter and Kröger (1992) of 3 mm, a more rigid fan motor frame should be used. The method of centering the fan rotor radially within the shroud annulus needs to be addressed. With the current setup the cantilever beam housing the fan shaft bearings and fan shaft is attached to and supported by the shroud annulus with three chains. By adjusting the tension in each chain independently the fan rotor is centered, however the fan rotor is constrained to move only in these three directions. If the chain setup is continued it should be replaced by four chains aligned 0°, 90°, 180° and 270° relative to the horizon, to allow more freedom of movement and centering of the fan rotor. The method of supporting the cantilever beam by attaching it to the shroud annulus with chains should be abandoned altogether, since during testing the whole settling chamber wall normal to the fan axis starts to move back and forth. The frame shroud be fixed to the settling chamber wall to prevent any independent movement.

Solving a complete performance curve for a low pressure rise, ducted turbomachinery application was attempted with CFD software primarily developed for high pressure rise, high velocity turbomachinery applications. Simulation of the fan performance curve at volumetric flow rates lower than the design operating point is constrained by instabilities in the flow solution. Recirculation cells forming at the inlet to the fan rotor produce high turbulence that the flow solver is unable to disperse.

Recommendations for future research include:

- An investigation to ascertain to what extent a transient simulation would solve the low flow rate instabilities.
- The model was unsuccessful in switching from the Spalart-Allmaras turbulence model to any of the low Reynolds $k-\varepsilon$ turbulence models (Launder-Sharma $k-\varepsilon$, Chien $k-\varepsilon$ and Extended wall-function $k-\varepsilon$), with the Yang-Shih $k-\varepsilon$ turbulence model being the only exception. At the design operating point the $k-\varepsilon$ turbulence model is less stable than the Spalart-Allmaras turbulence model and the effect of the $k-\varepsilon$ turbulence model at lower flow rates warrants future investigation.
- Implementing a grid that is dependent on the operating point specification of the fan performance curve. Kelecy (2000) mentions observing significant pressure gradients (from the inlet to the fan) at lower flow rates. To resolve this, he extended the inlet mesh an additional two fan diameters upstream from the original location, for lower flow rates. The same method of a flow-dependent mesh should be investigated.

- The knowledge gained related to the model setup and the available blade geometry data obtained should be used for future investigation into the simulation of an axial flow fan on different CFD software packages such as FLUENT™ and OpenFoam™.

Appendices

Appendix A

Fan blade data for numerical simulation

In this appendix the distribution of chord length and stagger angle radially across the blade length is illustrated. A plot to exemplify the similarity between the GA(W)-2 profile and the LS(1)-0413 profile from the different data sets is presented. The fan blade profile data set that defines the hub profile is given.

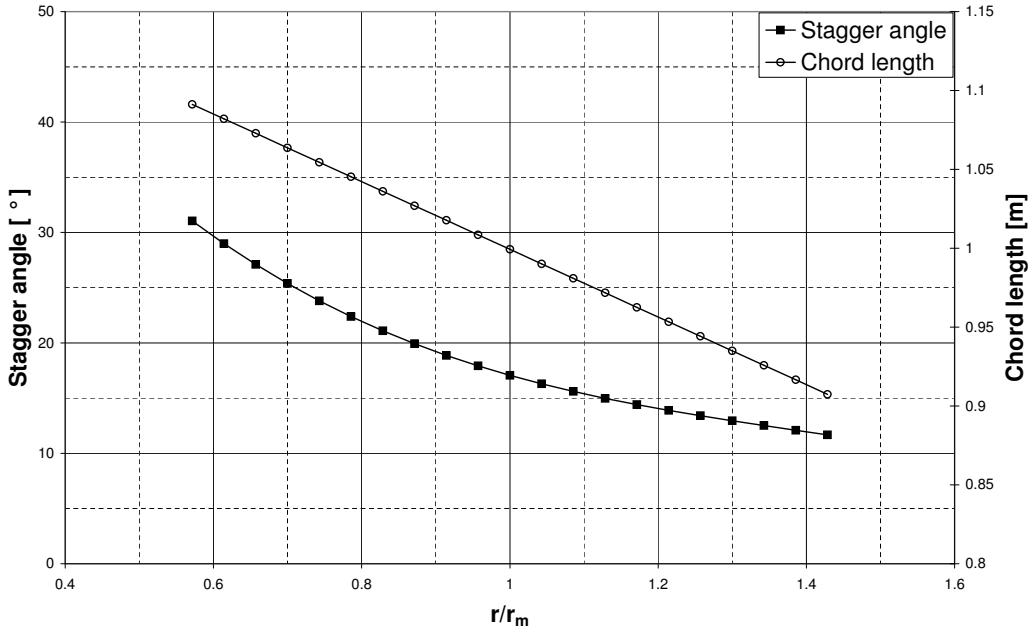

Figure A.1: Chord length and stagger angle distribution.

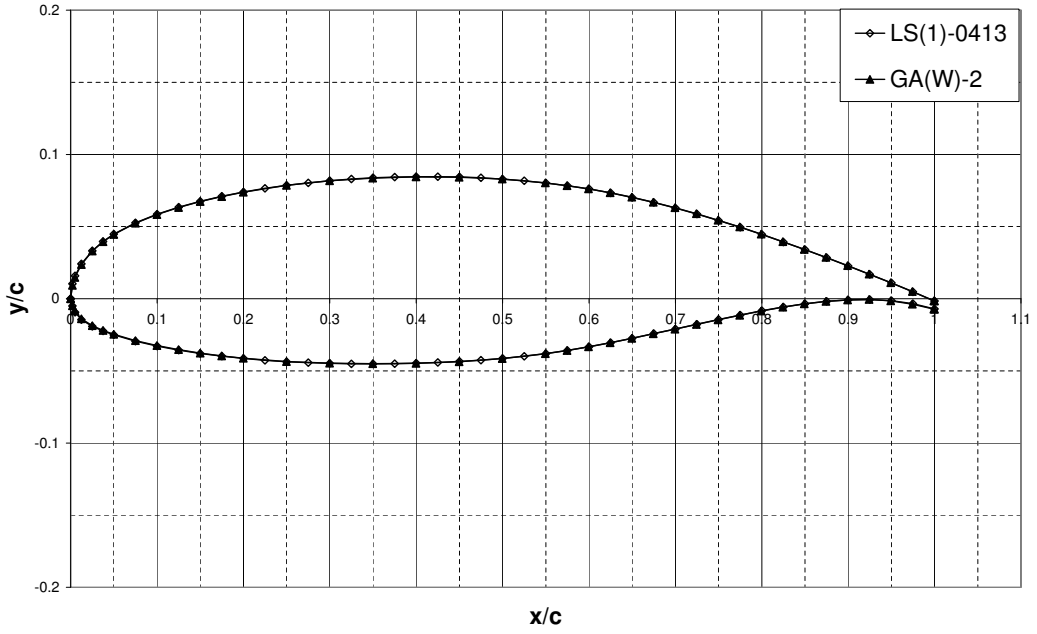

Figure A.2: A plot of the GA(W)-2 and LS(1)-0413 profiles.

Table A.1: Fan blade profile data for numerical simulation

x/c	y/c, upper	y/c, lower
0.0000	0.0000	0.0000
0.0005	0.0034	-0.0015
0.0010	0.0062	-0.0028
0.0015	0.0085	-0.0040
0.0020	0.0104	-0.0050
0.0030	0.0131	-0.0068
0.0040	0.0148	-0.0082
0.0050	0.0159	-0.0094
0.0125	0.0242	-0.0145
0.0250	0.0332	-0.0191
0.0375	0.0397	-0.0223
0.0500	0.0448	-0.0250
0.0750	0.0526	-0.0294
0.1000	0.0586	-0.0328
0.1250	0.0635	-0.0356
0.1500	0.0675	-0.0379
0.1750	0.0710	-0.0398
0.2000	0.0740	-0.0414
0.2250	0.0765	-0.0427
0.2500	0.0786	-0.0437
0.2750	0.0803	-0.0443
0.3000	0.0818	-0.0448
0.3250	0.0830	-0.0451
0.3500	0.0838	-0.0452
0.3750	0.0843	-0.0450
0.4000	0.0846	-0.0447
0.4250	0.0846	-0.0442
0.4500	0.0844	-0.0435
0.4750	0.0838	-0.0426
0.5000	0.0829	-0.0414
0.5250	0.0817	-0.0399
0.5500	0.0802	-0.0381
0.5750	0.0783	-0.0359
0.6000	0.0761	-0.0333
0.6250	0.0733	-0.0305
0.6500	0.0702	-0.0274
0.6750	0.0667	-0.0242
0.7000	0.0629	-0.0210
0.7250	0.0587	-0.0177
0.7500	0.0542	-0.0144
0.7750	0.0495	-0.0113
0.8000	0.0445	-0.0083
0.8250	0.0393	-0.0057
0.8500	0.0340	-0.0035
0.8750	0.0284	-0.0018
0.9000	0.0227	-0.0008
0.9250	0.0169	-0.0006
0.9500	0.0110	-0.0013
0.9750	0.0048	-0.0034
1.0000	-0.0016	-0.0071

Appendix B

Sample calculations for experimental data

In this appendix the sample calculations are given to illustrate how the fan performance characteristics are derived according to the BS 848 standards (1980). The B2-fan from Bruneau (1994) was used, set at a 59° stagger angle with a flat plate covering the hub.

To process the raw data points the following steps were followed:

1. The captured data points from the LabVIEW program were saved in a text file. The data points were moved from the text file into an Microsoft Excel® spreadsheet where the starting and end zero values were used to calculate the drift. The correction for the drift was made linearly between the starting and end zero values.

2. The corrected values were adjusted by the respective calibration correction as derived in Chapter E. In the case of the torque values, a further 2 Nm was deducted to account for the "no-load" torque values as discussed in Chapter E, Section E.2.

3. The fan laws with the conversion factors given in the BS 848 standards (1980), were used to scale the results for fan pressure, fan power and fan efficiency to the standardised conditions. Since the fan size remains unchanged, only the speed (750 rpm) and density (1.2 kg/m^3) conversion factors need to be applied.

4. The results were scaled and ready for representation in graphs with fan performance curves for fan static pressure rise, fan power consumption and fan static efficiency plotted against volumetric flow rate respectively.

B.1 Sample Calculations

A fan performance data set consists of twenty one data points, each of which contains the static pressure differential between the settling chamber and the atmosphere(1), the static pressure differential across the inlet bellmouth(2) , the torque transferred to the fan(3) and the rotational speed of the fan(4). Before and after each run the ambient pressure and temperature is recorded and averaged.

Table B.1: Raw experimental data

Data point	(1)Δp_{sett}	(2)Δp_{bell}	(3)M	(4)N
1	-0.004	-0.006	-0.004	-0.001
...				
10	1.699	2.639	2.58	8.252
...				
25	0.005	-0.001	-0.001	-0.001

Data points 2 to 9 and 11 to 14 have been excluded from Table B.1, since only the tenth data point will be used in the sample calculations. See Table C.2 for the complete data range. Data points 1 and 25 are taken before and after each experimental run to account for drift during the duration of the experiment. The drift is assumed to increase linearly from the zero wind still condition (data point 1) to data point 25 containing the total zero value error drift at the end of the run. The initial error in obtaining a zero value is also added to the error due to drift to be deducted from each data point. The raw data is corrected for drift by using the following relation:

$$\text{drift} = \text{data}(1) + \left(\frac{\text{number of data point} - 1}{\text{number of measurements} - 1} \right) (\text{data}(25) - \text{data}(1)) \tag{B.1}$$

The corrected values for data point 10:

$$\begin{aligned}\Delta p_{\text{sett}} &= (162.248) - \left\{(-0.531) + \left(\tfrac{9}{24}\right) \times [(0.329) - (-0.531)]\right\} \\ &= 162.457\,\text{Pa} \qquad \text{(B.2)}\\ \Delta p_{\text{bell}} &= (254.156) - \left\{(-0.127) + \left(\tfrac{9}{24}\right) \times [(0.354) - (-0.127)]\right\} \\ &= 254.102\,\text{Pa} \qquad \text{(B.3)}\\ M &= (70.472) - \left\{(-0.135) + \left(\tfrac{9}{24}\right) \times [(-0.053) - (-0.135)]\right\} \\ &= 70.577\,\text{Nm} \qquad \text{(B.4)}\\ N &= (700.162) - \left\{(-0.460) + \left(\tfrac{9}{24}\right) \times [(-0.460) - (-0.460)]\right\} \\ &= 700.622\,\text{rpm} \qquad \text{(B.5)}\end{aligned}$$

From equation (B.5) it is apparent that the speed indicator box is not affected by drift but does render the same error for zero rotation at the beginning and end of a test run. Therefore only this error value is subtracted from the measured values in agreement with Meyer (1996).

The ambient pressure was measured as 1007.6 hPa.

$$\begin{aligned}p_{\text{amb}} &= 1007.6 \times 100 \\ &= 100\,760\,\text{Pa} \qquad \text{(B.6)}\end{aligned}$$

The ambient temperature was measured as 10.6 ℃.

$$\begin{aligned}T_{\text{amb}} &= 10.6 + 273.15 \\ &= 283.75\,\text{K} \qquad \text{(B.7)}\end{aligned}$$

The sample calculations below follow the guidelines set out in the BS 848 standards (1980).

The ambient density is calculated from the perfect gas relation:

$$\begin{aligned}\rho_{\text{amb}} &= \frac{p_{\text{amb}}}{R\,T_{\text{amb}}} \\ &= \frac{100760}{287.08 \times 283.75} \\ &= 1.237\,\text{kg/m}^3 \qquad \text{(B.8)}\end{aligned}$$

The mass flow rate through the fan test facility is determined by measuring

the pressure drop across the inlet bellmouth and using the following relation:

$$\begin{aligned}\dot{m} &= \alpha\varepsilon \frac{\pi d_{\text{bell}}^2}{4} \sqrt{2\rho_{\text{amb}}\Delta p_{\text{bell}}} \\ &= 0.9803 \frac{\pi \times (1.008)^2}{4} \sqrt{2 \times 1.237 \times 254.102} \\ &= 19.614\,\text{kg/s}\end{aligned} \tag{B.9}$$

The compound calibration constant ($\alpha\varepsilon$) used here is the one determined by Venter (1990) to be 0.9803 and differs from the value of 0.985 recommended by the BS 848 standards (1980). This is due to the transformation piece between the inlet bellmouth and the remainder of the test facility being shorter (due to space limitations) than specified in the BS 848 standards.

The air density inside the settling chamber is calculated according to the ideal gas relation:

$$\begin{aligned}\rho_{\text{sett}} &= \rho_{\text{amb}} \frac{p_{\text{amb}} - \Delta p_{\text{sett}}}{p_{\text{amb}}} \\ &= 1.237 \frac{100760 - 162.457}{100760} \\ &= 1.235\,\text{kg/m}^3\end{aligned} \tag{B.10}$$

The mass flow calculated in equation (B.9) is used to determine the settling chamber's dynamic pressure component:

$$\begin{aligned}p_{d_{\text{sett}}} &= \frac{1}{2}\rho_{\text{sett}} U_{\text{sett}}^2 \\ &= \frac{1}{2}\rho_{\text{sett}} \left(\frac{\dot{m}}{A_{\text{sett}}}\right)^2 \\ &= \frac{1}{2\rho_{\text{sett}}} \left(\frac{\dot{m}}{A_{\text{sett}}}\right)^2 \\ &= \frac{1}{2 \times 1.235} \left(\frac{19.614}{16}\right)^2 \\ &= 0.608\,\text{Pa}\end{aligned} \tag{B.11}$$

The BS 848 standards (1980) stipulate the fan pressure rise as the difference between the fan static pressure at the fan outlet and the total pressure at the fan inlet. Therefore $p_{\text{Fs}} = p_{\text{amb}} - (p_{\text{s}_{\text{sett}}} + p_{\text{d}_{\text{sett}}})$, but since the measured settling chamber pressure (Δp_{sett}) is the static pressure difference between the settling chamber pressure and the atmosphere it can be seen as $\Delta p_{\text{sett}} = p_{\text{amb}} - p_{\text{s}_{\text{sett}}}$

and the fan pressure rise defined earlier can be simplified accordingly:

$$\begin{aligned} p_{\mathrm{Fs}} &= p_{\mathrm{amb}} - (p_{\mathrm{s_{sett}}} + p_{\mathrm{d_{sett}}}) \\ &= \Delta p_{\mathrm{s_{sett}}} - p_{\mathrm{d_{sett}}} \\ &= 162.457 - 0.608 \\ &= 161.849\,\mathrm{Pa} \end{aligned} \tag{B.12}$$

The fan power input is a product of the rotational speed and the torque applied to the fan shaft. 2 Nm is deducted from the applied torque to account for frictional losses as noted in Section E.2.

$$\begin{aligned} P_{\mathrm{F}} &= \frac{2\pi N M}{60} \\ &= \frac{2 \times \pi \times 700.622 \times (70.577 - 2)}{60} \\ &= 5031.427\,\mathrm{W} \end{aligned} \tag{B.13}$$

The volumetric flow rate is calculated from the mass flow through the test facility and the inlet density.

$$\begin{aligned} Q_{\mathrm{sett}} &= \frac{\dot{m}}{\rho_{\mathrm{sett}}} \\ &= \frac{19.614}{1.235} \\ &= 5.882\,\mathrm{m^3/s} \end{aligned} \tag{B.14}$$

The fan static efficiency is defined as the pressure rise per power consumed by the fan, multiplied by the volumetric flow rate through the fan test facility.

$$\begin{aligned} \eta_{\mathrm{Fs}} &= \frac{p_{\mathrm{Fs}} Q_{\mathrm{sett}}}{P_{\mathrm{F}}} \\ &= \frac{161.849 \times 15.882}{5031.427} \times 100 \\ &= 51.09\% \end{aligned} \tag{B.15}$$

The above calculated fan test parameters are scaled to a referenced air density of 1.2 kg/m^3 and a rotational speed of 750 rpm by using the fan laws as stipulated in the BS 848 standards (1980). The prime noted variables refer to

the scaled reference parameters:

$$\begin{aligned} Q' &= Q_{\text{sett}} \left(\frac{d'}{d}\right)^3 \left(\frac{N'}{N}\right) \\ &= 15.882 \left(\frac{1.542}{1.542}\right)^3 \left(\frac{750}{700.622}\right) \\ &= 17.002\,\text{m}^3/\text{s} \end{aligned} \tag{B.16}$$

$$\begin{aligned} p'_{\text{Fs}} &= p_{\text{Fs}} \left(\frac{d'}{d}\right)^2 \left(\frac{N'}{N}\right)^2 \left(\frac{\rho'}{\rho_{\text{sett}}}\right) \\ &= 161.849 \left(\frac{1.542}{1.542}\right)^2 \left(\frac{750}{700.622}\right)^2 \left(\frac{1.2}{1.235}\right) \\ &= 180.217\,\text{Pa} \end{aligned} \tag{B.17}$$

$$\begin{aligned} P'_{\text{F}} &= P_{\text{F}} \left(\frac{d'}{d}\right)^5 \left(\frac{N'}{N}\right)^3 \left(\frac{\rho'}{\rho_{\text{sett}}}\right) \\ &= 5031.427 \left(\frac{1.542}{1.542}\right)^5 \left(\frac{750}{700.622}\right)^3 \left(\frac{1.2}{1.235}\right) \\ &= 5997.31\,\text{W} \end{aligned} \tag{B.18}$$

$$\eta'_{\text{Fs}} = \eta_{\text{Fs}} = 51.09\% \tag{B.19}$$

Appendix C

Experimental Data

For 59° the experimental constants, the data from the conversion of raw voltage readings, the data from the correction for drift, the calculated performance parameters and the scaled performance parameters are given. These intermediate data sets are not provided for angles 58° and 60° and only the experimental constants and scaled performance parameters for these two angles are given.

Table C.1: Experimental data constants for 59° stagger angle

Reference density	1.2	kg/m^3
Reference rotational speed	750	rpm
Reference fan diameter	1.542	m
Shroud diameter	1.542	m
Bellmouth diameter	1.008	m
Tip clearance	0.003	m
Stagger angle	59	°
Compound calibration constant	0.9803	
Universal gas constant	287.08	
Actual rotational speed	700	rpm
Ambient pressure	1007.6	hPa
Ambient temperature	10.6	$°C$

Table C.2: Conversion of voltage data for 59° stagger angle

	Raw voltage data				Voltage data converted			
	Δp_{sett}	Δp_{bell}	T	N	Δp_{sett}	Δp_{bell}	M	N
	V	V	V	V	Pa	Pa	Nm	rpm
1	-0.004	-0.006	-0.004	-0.001	-0.531	-0.127	-0.135	-0.460
2	-0.127	4.948	1.624	8.264	-12.288	476.136	44.350	701.181
3	-0.089	4.892	1.637	8.251	-8.656	470.752	44.705	700.077
4	-0.06	4.851	1.648	8.241	-5.884	466.811	45.006	699.228
5	0.129	4.589	1.773	8.248	12.181	441.623	48.421	699.823
6	0.241	4.445	1.849	8.256	22.887	427.779	50.498	700.502
7	0.484	3.999	2.003	8.246	46.114	384.902	54.706	699.653
8	0.774	3.612	2.162	8.252	73.833	347.697	59.051	700.162
9	1.18	3.159	2.362	8.25	112.640	304.147	64.516	699.992
10	1.699	2.639	2.58	8.252	162.248	254.156	70.473	700.162
11	2.149	2.12	2.719	8.25	205.261	204.260	74.271	699.992
12	2.478	1.714	2.78	8.253	236.708	165.229	75.938	700.247
13	2.807	1.296	2.802	8.25	268.155	125.044	76.539	699.992
14	3.029	1.012	2.771	8.246	289.375	97.741	75.692	699.653
15	3.215	0.767	2.728	8.248	307.153	74.187	74.517	699.823
16	3.398	0.503	2.644	8.254	324.645	48.807	72.221	700.332
17	3.623	0.334	2.556	8.249	346.152	32.560	69.817	699.907
18	3.869	0.195	2.515	8.255	369.665	19.197	68.696	700.417
19	4.12	0.105	2.459	8.252	393.657	10.544	67.166	700.162
20	4.282	0.058	2.438	8.249	409.142	6.026	66.592	699.907
21	4.374	0.041	2.432	8.255	417.935	4.392	66.429	700.417
22	4.418	0.031	2.419	8.248	422.141	3.430	66.073	699.823
23	4.516	0.021	2.419	8.255	431.508	2.469	66.073	700.417
24	4.631	0.01	2.419	8.253	442.500	1.411	66.073	700.247
25	0.005	-0.001	-0.001	-0.001	0.329	0.354	-0.053	-0.460

Table C.3: Voltage data corrected for drift for 59° stagger angle

Data corrected for drift			
Δp_{sett} [Pa]	Δp_{bell} [Pa]	M [Nm]	N [rpm]
-12.324	476.243	44.482	701.641
-8.196	470.839	44.833	700.537
-5.460	466.877	45.131	699.688
12.569	441.669	48.543	700.282
23.239	427.806	50.616	700.962
46.430	384.909	54.821	700.113
74.113	347.683	59.162	700.622
112.885	304.113	64.624	700.452
162.457	254.102	70.577	700.622
205.434	204.187	74.372	700.452
236.845	165.135	76.035	700.707
268.256	124.930	76.633	700.452
289.440	97.607	75.782	700.113
307.183	74.034	74.604	700.282
324.639	48.633	72.305	700.792
346.110	32.366	69.897	700.367
369.587	18.983	68.774	700.877
393.543	10.311	67.240	700.622
408.992	5.772	66.663	700.367
417.750	4.118	66.495	700.877
421.920	3.136	66.137	700.282
431.251	2.155	66.133	700.877
442.207	1.078	66.130	700.707

Table C.4: Calculated performance parameters for 59° stagger angle

$\dot{m}$	ρ_{sett}	$p_{d_{\text{sett}}}$	p_{Fs}	P_{F}	Q_{sett}	η_{Fs}
kg/s	kg/m^3	Pa	Pa	W	m^3/s	%
26.852	1.237	1.138	-13.462	3121.369	21.706	-9.362
26.699	1.237	1.125	-9.322	3142.268	21.583	-6.403
26.586	1.237	1.116	-6.576	3160.233	21.493	-4.472
25.859	1.237	1.056	11.513	3413.146	20.908	7.053
25.450	1.237	1.023	22.216	3568.645	20.579	12.811
24.140	1.236	0.921	45.509	3872.588	19.525	22.945
22.943	1.236	0.832	73.282	4193.919	18.562	32.434
21.457	1.236	0.728	112.157	4593.517	17.367	42.403
19.614	1.235	0.608	161.849	5031.427	15.882	51.090
17.582	1.234	0.489	204.945	5308.558	14.243	54.988
15.812	1.234	0.396	236.450	5432.546	12.813	55.768
13.753	1.234	0.299	267.957	5474.416	11.148	54.567
12.156	1.233	0.234	289.206	5409.407	9.856	52.694
10.587	1.233	0.178	307.006	5324.304	8.585	49.503
8.581	1.233	0.117	324.522	5159.481	6.960	43.774
7.000	1.233	0.078	346.032	4979.747	5.679	39.460
5.361	1.232	0.046	369.542	4900.891	4.350	32.800
3.951	1.232	0.025	393.518	4786.590	3.207	26.363
2.956	1.232	0.014	408.978	4742.514	2.400	20.694
2.497	1.232	0.010	417.740	4733.679	2.027	17.888
2.179	1.232	0.008	421.912	4703.366	1.769	15.870
1.806	1.232	0.005	431.246	4707.106	1.467	13.436
1.277	1.232	0.003	442.205	4705.715	1.037	9.746

Table C.5: Scaled performance parameters for 59° stagger angle

Q'_{sett} [m^3/s]	p'_{Fs} [Pa]	P'_{F} [W]
23.202	-14.921	3697.970
23.107	-10.365	3740.505
23.038	-7.330	3775.703
22.392	12.813	4068.227
22.019	24.679	4241.668
20.916	50.690	4620.761
19.870	81.527	4994.639
18.595	124.885	5476.617
17.002	180.217	5997.310
15.251	228.413	6334.950
13.714	263.416	6477.868
11.937	298.827	6536.960
10.558	322.906	6470.101
9.195	342.673	6364.804
7.448	361.762	6155.401
6.081	386.290	5953.054
4.655	412.032	5847.388
3.433	439.189	5718.608
2.570	456.845	5673.006
2.169	465.995	5650.595
1.895	471.468	5628.948
1.569	481.126	5619.630
1.110	493.646	5622.668

Table C.6: Experimental data constants for 58° stagger angle

Reference density	1.2	kg/m^3
Reference rotational speed	750	rpm
Reference fan diameter	1.542	m
Shroud diameter	1.542	m
Bellmouth diameter	1.008	m
Tip clearance	0.003	m
Stagger angle	58	°
Compound calibration constant	0.9803	
Universal gas constant	287.08	
Actual rotational speed	700	rpm
Ambient pressure	1007.9	hPa
Ambient temperature	12.5	$°C$

Table C.7: Scaled performance parameters for 58° stagger angle

Q'_{sett} [m^3/s]	p'_{Fs} [Pa]	P'_{F} [W]	$\eta_{\text{Fs}}\%$
23.566	7.802	4518.528	4.069
23.564	6.008	4479.143	3.161
23.718	4.305	4463.241	2.288
22.869	27.460	4777.109	13.146
22.186	42.089	4999.553	18.678
21.355	63.546	5273.662	25.732
20.366	94.761	5666.742	34.057
18.961	140.071	6135.895	43.285
17.330	192.219	6623.218	50.295
15.650	242.104	6961.444	54.427
13.773	282.148	7100.306	54.731
12.218	310.224	7103.937	53.357
10.741	334.088	6997.754	51.280
9.343	353.842	6839.119	48.337
7.519	369.650	6621.966	41.974
6.193	392.168	6412.283	37.875
4.630	420.932	6317.413	30.852
3.423	447.817	6258.080	24.493
2.645	465.980	6245.329	19.734
2.112	475.657	6228.794	16.125
1.926	481.770	6232.219	14.890
1.514	490.803	6249.711	11.889
1.238	499.808	6282.884	9.846

Table C.8: Experimental data constants for 60° stagger angle

Reference density	1.2	kg/m^3
Reference rotational speed	750	rpm
Reference fan diameter	1.542	m
Shroud diameter	1.542	m
Bellmouth diameter	1.008	m
Tip clearance	0.003	m
Stagger angle	60	°
Compound calibration constant	0.9803	
Universal gas constant	287.08	
Actual rotational speed	700	rpm
Ambient pressure	1005.8	hPa
Ambient temperature	16.35	$°C$

Table C.9: Scaled performance parameters for 60° stagger angle

Q'_{sett} [m^3/s]	p'_{Fs} [Pa]	P'_{F} [W]	η_{Fs}%
22.633	-23.108	3186.913	-16.411
22.613	-24.147	3200.884	-17.059
22.476	-19.072	3233.801	-13.256
22.106	-4.418	3445.759	-2.834
21.456	17.735	3740.938	10.172
20.510	41.769	4077.620	21.009
19.635	66.761	4393.162	29.839
18.263	111.212	4898.502	41.462
16.772	168.176	5449.637	51.758
15.098	211.753	5750.974	55.590
13.570	249.137	5952.692	56.792
12.177	278.952	6019.756	56.430
10.541	309.986	6003.413	54.428
9.020	336.497	5901.827	51.427
7.269	355.033	5715.762	45.154
5.928	381.173	5512.271	40.992
4.665	403.893	5424.308	34.733
3.411	432.610	5283.961	27.925
2.654	451.199	5216.193	22.961
2.135	461.401	5180.472	19.014
1.753	469.589	5131.040	16.047
1.433	479.036	5116.212	13.414
1.167	486.446	5115.879	11.098

Appendix D

Experimental Instrumentation

A schematic representation of the instrumentation that was used during the experiments can be seen in Figure D.1.

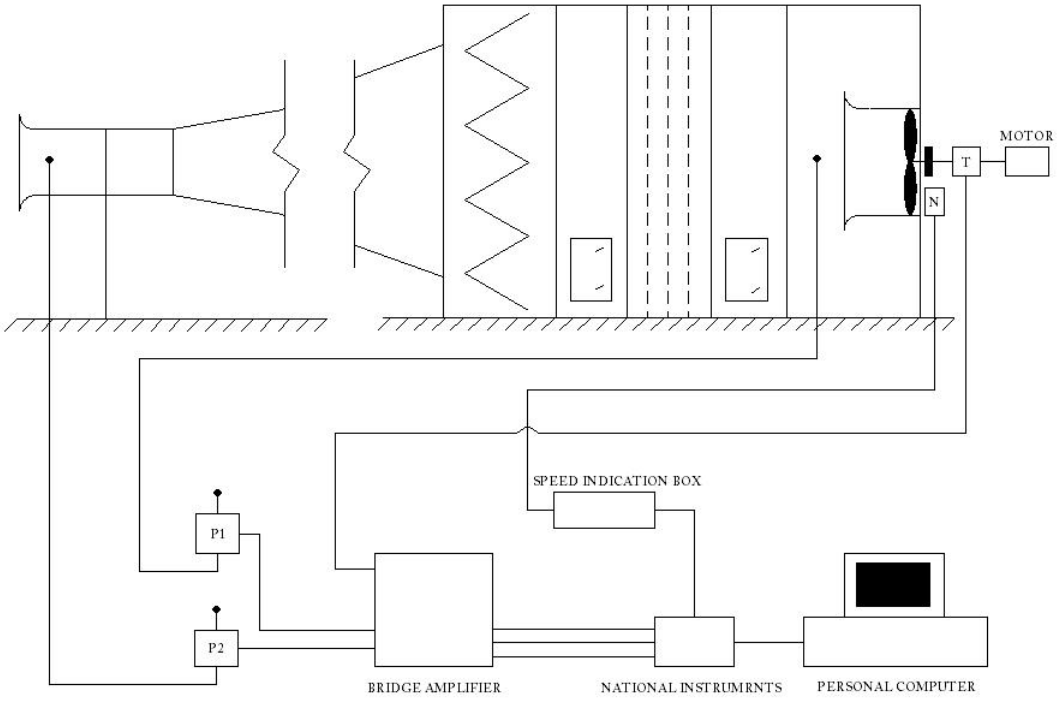

Figure D.1: Schematic layout of experimental instrumentation.

The procedure listed below was followed each time an experimental test was carried out:

1. The bridge amplifier is switched on and allowed to warm up for at least 30 minutes. While in the control room the frequency counter and personal computer is switched on. At this time the auxiliary fan and hydraulic motor's power supply is connected and the tap is turned on to supply cooling water to the hydraulic motor.

2. The fan test facility is inspected for anything that might seem out of place. Special care is taken to ensure that the fan can rotate freely and that both hatch doors of the settling chamber are closed tightly. The throttling device is placed back to its fully open position.

3. Ambient conditions are measured (see Section D.1). The LabVIEW program is started on the personal computer and zero starting readings are taken, to be used in calculating the drift when the data is processed. The drift calculations is performed following the method proposed by Stinnes (1998).

4. The auxiliary fan is switched on. Hereafter the main hydraulic motor is switched on and left to idle and warm up.

5. The rotational speed of the fan is slowly increased to the test speed by monitoring the frequency counter and keeping a careful eye on the rotating fan for any abnormalities. Once a satisfactory steady state has been reached at the test speed, a data point is captured in the LabView program.

6. The throttling device is then closed by one notch. Procedure 5 is repeated until the throttling device is completely closed.

7. A data point is taken with the throttling device at the fully closed position and the auxiliary fan switched off to investigate the pressure difference at an even lower volumetric flow rate than that of the closed position.

8. The oil supply to the hydraulic motor is gradually reduced until an idle state is achieved and the motor is switched off. The ambient pressure and temperature are recorded again.

9. In this time both the fans would have come to a standstill and the end zero values are recorded for drift calculation. All the data captured is saved in a text file on the computer.

10. All the instrumentation inside the control room is switched off and the power leads for the auxiliary fan and hydraulic motor is removed and stored away. The cooling water tap is closed.

D.1 Ambient Conditions

Ambient pressure was measured with a mercury column barometer situated in a laboratory room close to the test facility. The barometer is calibrated by the manufacturer to account for the local gravitational force and provide readings in hPa.

Ambient temperature was measured with a thermometer located next to the test facility in the shade. A substantial difference was noted between the alcohol column thermometer attached to the barometer inside the nearby laboratory and the thermometer hanging outside next to the facility. The mercury column thermometer measured higher temperatures and fluctuated only slightly during the course of the day. After carrying out numerous experiments during different times of the day it was established that testing later than an hour after sunrise provided big fluctuations in torque readings, influencing repeatability. This variation may be the result of the test facility being heated non-uniformly by direct sunlight and reflection from the windows of the adjacent buildings as well as part of the facility being under a roof while the rest is exposed. Stinnes (1998) also noted an "indeterminable variation" in a comparison of temperature measurements in different locations around the test facility. For the best test results, experiments were carried out two hours before sunrise when the atmosphere had cooled down to a constant temperature with wind still conditions. Temperature readings were taken before and after each test run and averaged.

D.2 Pressure

To acquire the static pressure from the inlet bellmouth and settling chamber two Höttinger PD1 inductive differential pressure transducers were used. These pressure transducers have a range of $-1000\,\text{Pa}$ to $1000\,\text{Pa}$.

Stinnes (1998) found Venter (1990)'s placement of the transducer adjacent to the bellmouth unfavourable and moved the transducers into the control room. The two pressure transducers were left inside the control room and kept in the same orientation when calibrated. All the plastic tubing connecting the transducers to the test facility was tested for leaks and was found air-tight.

D.3 Torque

To measure the torque a Höttinger T2 (resistive full bridge strain gauge type) torque transducer is used. The torque transducer has a nominal range of $-500\,\text{Nm}$ to $500\,\text{Nm}$.

The torque transducer is connected to the hydraulic motor and the fan shaft by two rubber couplings to account for vibration and misalignment. Two bearing blocks support the transducer in-between the rubber couplings. The friction in these couplings and bearings are described in Section E.2 and accounted for in the calibration of the torque measurements.

D.4 Speed

A magnetic speed pick-up sensor below the fan shaft is used to obtain the rotational speed of the fan by giving an input signal to the dual output frequency counter. The first output is to a digital display that is monitored to regulate the rotational speed by adjusting the supply of hydraulic oil to the fan motor. The second output is a linear voltage signal fed into the National Instruments card.

Calibration of all the instrumentation is discussed in Appendix E.

D.5 Bridge amplifier

A Höttinger KWS 3073 bridge amplifier is used to amplify the input signals from the transducers before the voltages are sent to the personal computer. The input signals are amplified over a range of $-10\,\mathrm{V}$ to $10\,\mathrm{V}$.

All signals from the bridge amplifier as well as that of the dual output frequency counter are fed to a National Instruments NI USB-6210 bus-powered multifunction data acquisition module. The signals are then sent to the personal computer via its USB port where a LabVIEW program is used to capture the data.

D.6 Blade angle setting jig

The blade stagger angle was set by a custom made jig that provided a flat platform for the SmartTool digital projector. The pressure side blade profile was laser cut into two stainless steel plates that were attached to either side of a plastic block as illustrated in Figure D.2. To determine the offset in angle from the chord line to the line tangent of the pressure surface, a blade was laid flat on a marble table with the edges supported with Presstick. The chord line was set horizontal by positioning the leading edge and trailing edge points at the same height as can be seen in Figures D.3 and D.4. The difference between the blade setting angle and the stagger angle was measured to be 4.2°, as can be seen in Figure D.5. To therefore set the blades at a stagger angle of 59° a blade setting angle of 63.2° was used. To keep the blade at a

horizontal level while the angle was being set, the shaft was locked in position by a clamping device designed by a fellow student. The clamping device is illustrated in Figure D.6.

Figure D.2: Blade stagger angle setting jig.

Figure D.3: Stagger angle jig chord leading edge.

Figure D.4: Stagger angle jig chord trailing edge.

Figure D.5: Difference between stagger angle and blade setting angle.

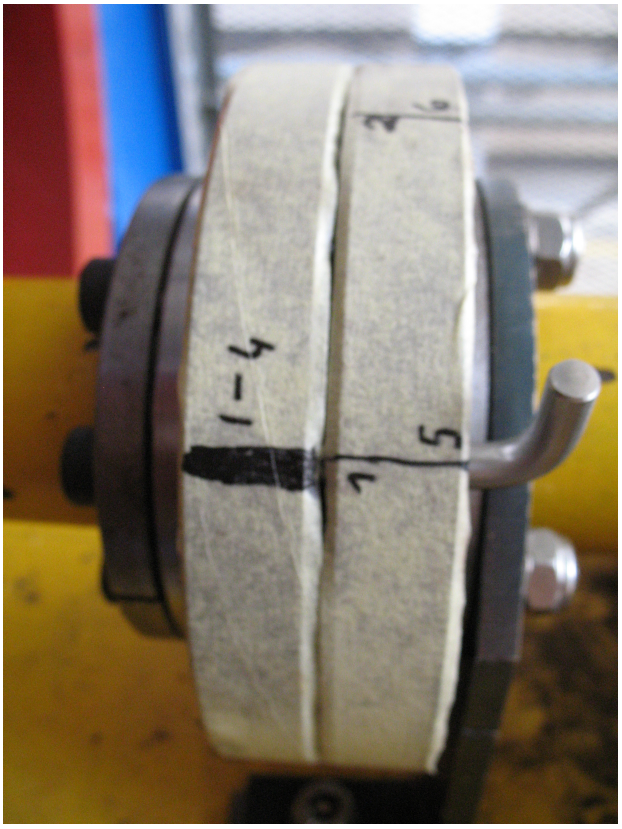

Figure D.6: Device for clamping rotor shaft.

Appendix E

Calibration of instrumentation

E.1 Pressure Calibration

The two pressure transducers were calibrated by using a Betz water column manometer. The negative pressure tappings of the pressure transducers were connected by means of a pipe system and a ball-valve to the negative column of the Betz manometer. Figure E.1 gives an illustration of the pressure calibration setup. Before the calibration was started the pressure transducers were stuck unto the table with Presstick. This prevented the pressure transducers from moving during calibration and it was left as is to keep the transducers in the same position during experiments as they were during the calibration process.

The collected data was fed into a Microsoft Excel® spreadsheet to draw up a graph of pressure versus voltage distribution. A linear trend line was fitted to the curve and the equation from the graph was used to correct the pressure readings obtained from experimental work. The calibration data can be viewed in Table E.1 with the corresponding graphs from the Microsoft Excel® spreadsheet in Figure E.2 and Figure E.3.

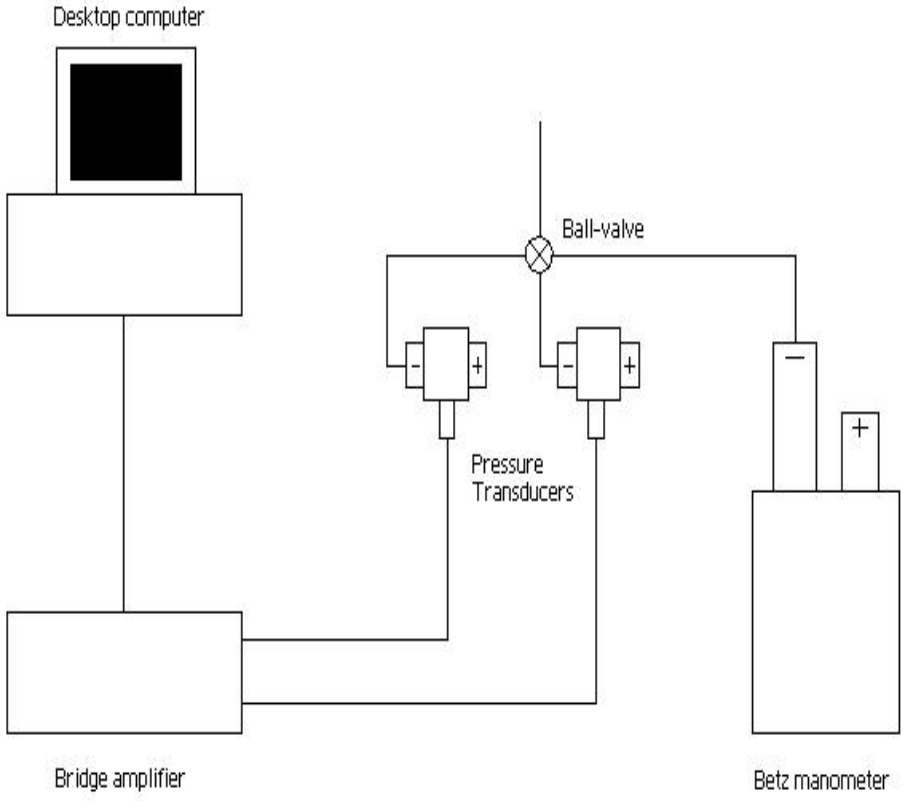

Figure E.1: Pressure calibration setup.

Table E.1: Calibration of pressure transducers

(a) Settling chamber pressure transducer

Channel 1		
Water level	Pressure	Voltage
mm	Pa	V
0	0.000	0.000
10	97.764	1.023
20	195.528	2.042
30	293.292	3.074
40	391.056	4.098
50	488.820	5.127
60	586.584	6.137
70	684.349	7.152

(b) Bellmouth pressure transducer

Channel 4		
Water level	Pressure	Voltage
mm	Pa	V
0	0.000	0.000
10	97.764	1.011
20	195.528	2.021
30	293.292	3.046
40	391.056	4.064
50	488.820	5.089
60	586.584	6.097
70	684.349	7.111

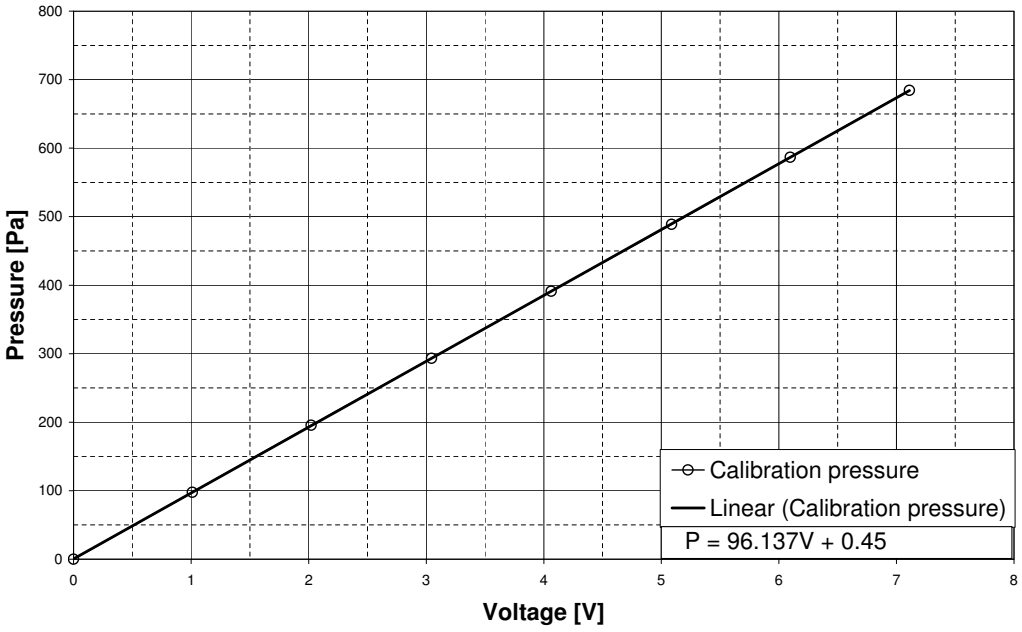

Figure E.2: Pressure calibration bellmouth.

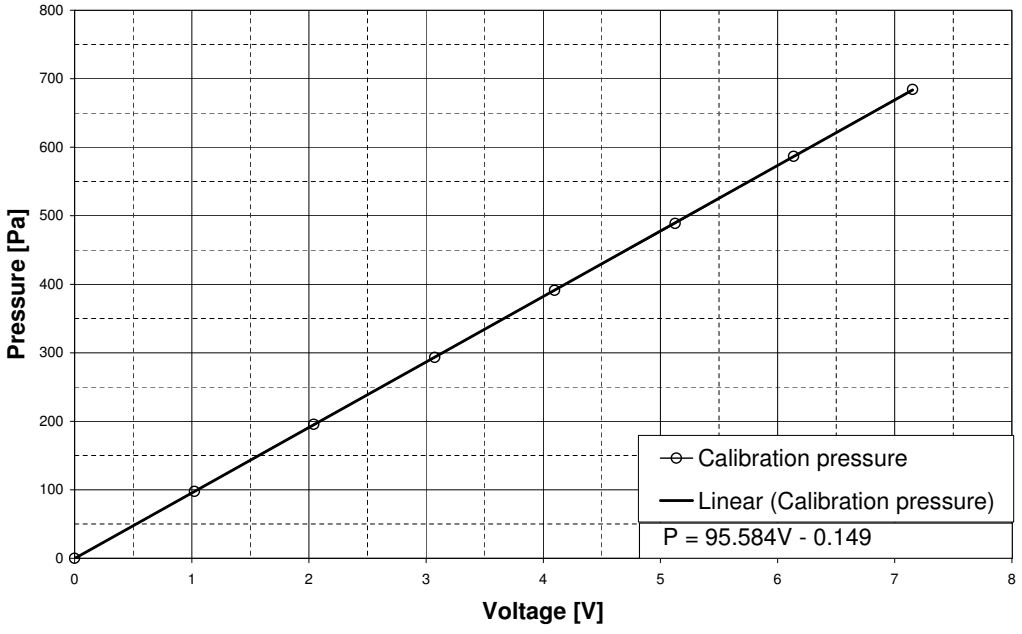

Figure E.3: Pressure calibration settling chamber.

E.2 Torque Calibration

The torque calibration was done by using a cantilever beam. To use the cantilever the fan and hub first need to be removed. Hereafter the shaft on the motor side of the torque transducer is locked in place. This enables the transducer to only measure the torque due to the deflection of the cantilever beam. The shaft is locked in place when the cantilever beam is at a horizontal level. This level is measured with a digital projector as shown in Figure E.4. Weights weighing 5.020 kg, 5.025 kg, 5.015 kg and 4.975 kg respectively were placed on the holding disk of the cantilever beam. Each time a weight is placed on the disk the shaft is rotated back to its horizontal position to account for the deformation of the shaft, torque transducer and the couplings. The corresponding voltages were taken from the bridge amplifier and recorded.

Figure E.4: Torque calibration horizontal level measurement.

The collected data was fed into a Microsoft Excel® spreadsheet to draw up a graph of torque versus voltage distribution. A linear trend line was fitted to the curve and the equation from the graph was used to calculate the torque readings obtained from experimental work. The calibration data can be viewed in Table E.2 with the corresponding graphs from the Microsoft Excel® spreadsheet in Figure E.5.

A "no-load" torque test was also carried out to establish the torque effect of the shaft bearings and any misalignment. This was done by stripping the fan blades from the hub and running the test at the design speed with the flat

Table E.2: Torque calibration data

Reading	Mass [kg]	Voltage [V]	Torque [Nm]
1	0	0	0
2	5.020	0.158	25.276
3	10.045	0.297	50.578
4	15.060	0.450	75.829
5	20.035	0.602	100.879

plate attached to the hub and without. The results of the "no-load" test can be seen in Table E.3. Start and end zero values were taken before the hub was brought up to design speed. These values were used to eliminate the drift from the bridge amplifier and produce the "corrected voltage" as can be seen in Table E.3. These corrected voltages were then adjusted with the values obtained from the calibration data. Since the fan will be tested with the flat plate installed, only the data from Table E.3b is taken into account. It can be seen that the third reading differs from the first two (which are identical) and it is therefore disregarded. Bruneau (1994) could also not find the cause for the variations in the "no-load" torques and subtracted a constant torque value of 2 Nm from all the fan performance torque readings. This value agrees favourably with the last two values obtained in Table E.3b. Stinnes (1998)

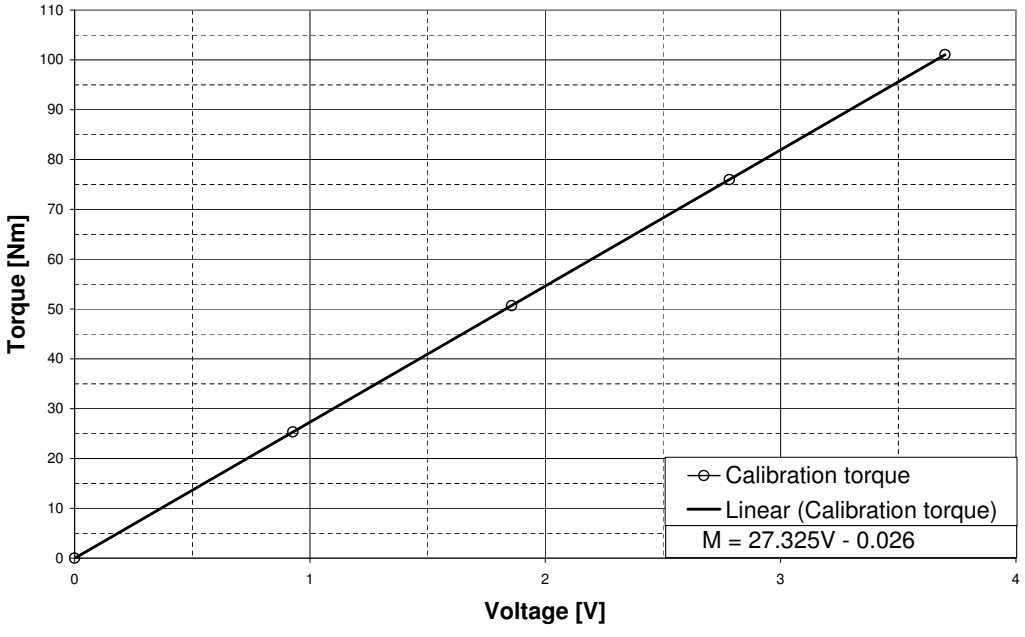

Figure E.5: Torque calibration curve.

also subtracted a constant torque value of 2 Nm.

Table E.3: "No-load" torque test without and with flat plate

(a) "No-load" torque test without flat plate

"No-load" test without flat plate			
Reading	Voltage [V]	Corrected Voltage [V]	Torque [Nm]
1	-0.003		
2	0.011	0.011	1.817
3	-0.002		
1	-0.002		
2	0.011	0.011	1.817
3	-0.002		
1	-0.001		
2	0.013	0.013	2.157
3	-0.002		

(b) "No-load" torque test with flat plate

"No-load" test with flat plate			
Reading	Voltage [V]	Corrected Voltage [V]	Torque [Nm]
1	-0.000		
2	0.009	0.009	1.477
3	-0.001		
1	0.000		
2	0.012	0.012	1.987
3	0.000		
1	0.001		
2	0.012	0.012	1.987
3	0.002		

E.3 Speed Calibration

To calibrate the speed indicator the motor was run at 100 RPM intervals and the actual speed was measured inside the plenum chamber with an Ono Sokki HT-341 digital tachometer. The tachometer was held against the rotating shaft until a constant reading was obtained. The speed indicator- and tachometer reading were recorded.

The collected data was fed into a Microsoft Excel® spreadsheet to draw up a graph of speed (from the speed indication box and the tachometer) versus voltage distribution. A linear trend line was fitted to the curve and the equation from the graph was used to correct the speed readings obtained from experimental work. The calibration data can be viewed in Table E.4 with the corresponding graphs from the Microsoft Excel® spreadsheet in Figure E.6.

Table E.4: Speed calibration data

Reading	Speed [rpm]	Voltage [V]
1	0	0
2	127	1.541
3	169	1.999
4	255	3.024
5	343	4.045
6	425	5.018
7	510	6.018
8	596	7.038
9	680	8.031
10	765	9.030

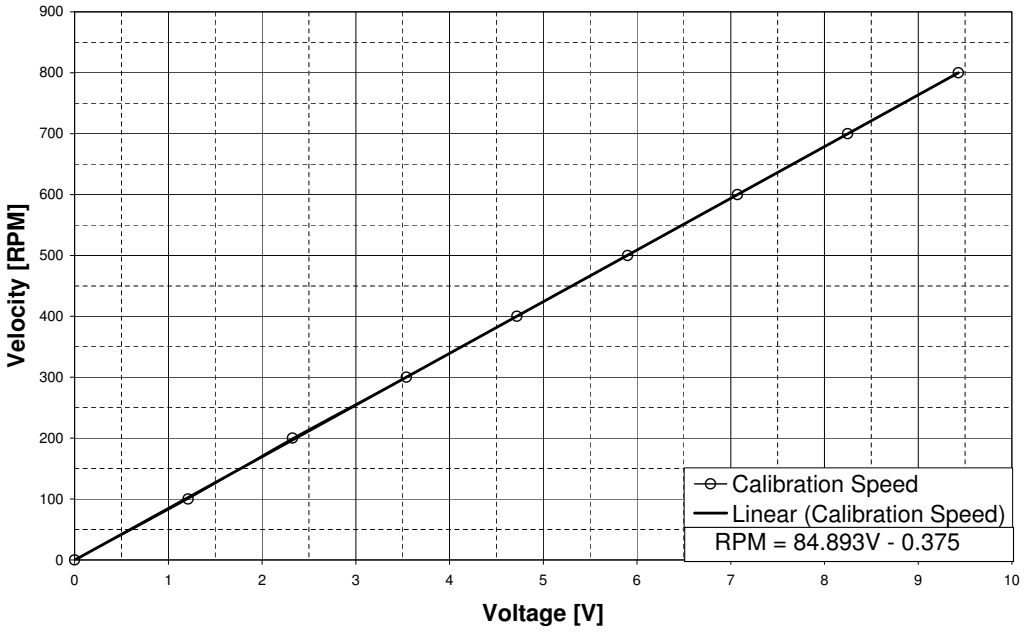

Figure E.6: Speed tachometer calibration curve.

Appendix F

Fan performance characteristics

In this appendix the fan performance characteristics are given for the three blade angles, namely 58°, 59° and 60°, without the data from Stinnes to reduce the clutter. For all three stagger angles the experimental results are compared to the data from Stinnes (1998) and Bruneau (1994). Finally the fan performance characteristics for the tests performed at a tip clearance of 1.5 mm are shown.

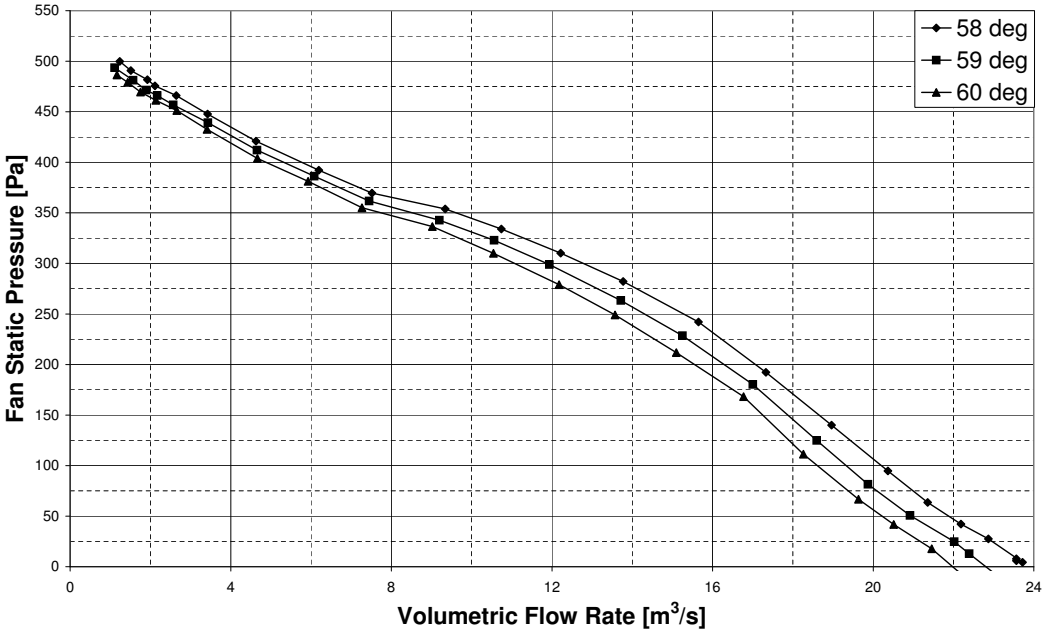

Figure F.1: Fan static pressure rise at three blade angles.

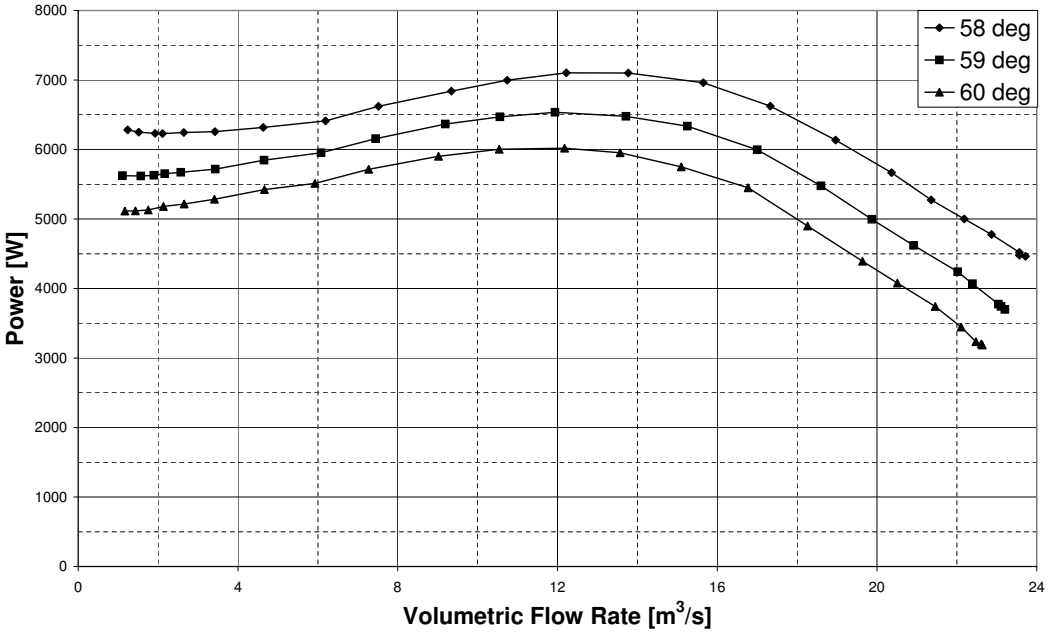

Figure F.2: Fan power at three blade angles.

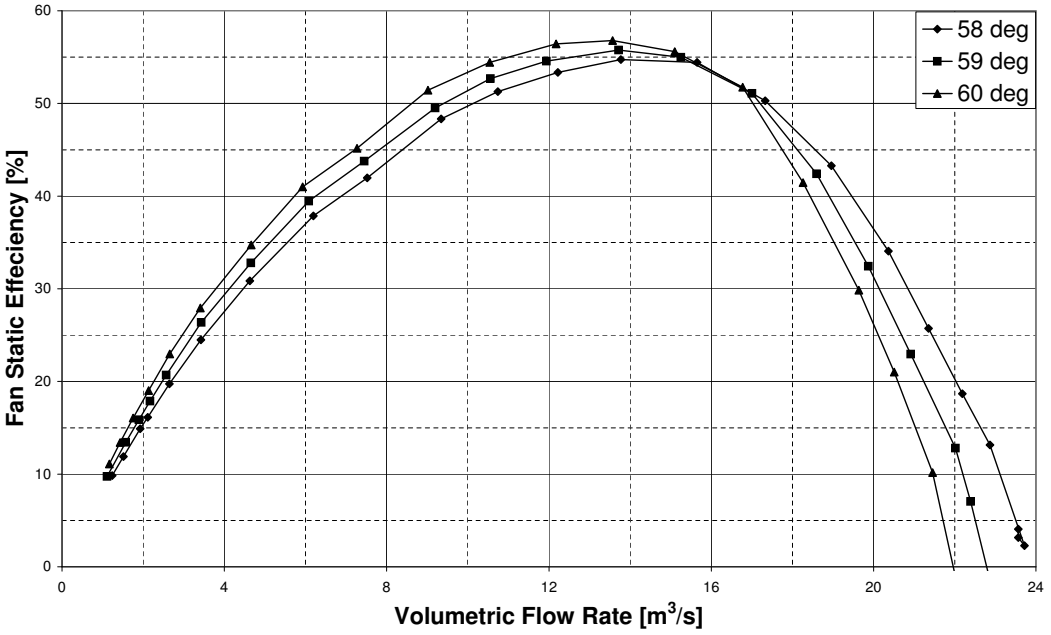

Figure F.3: Fan static efficiency at three blade angles.

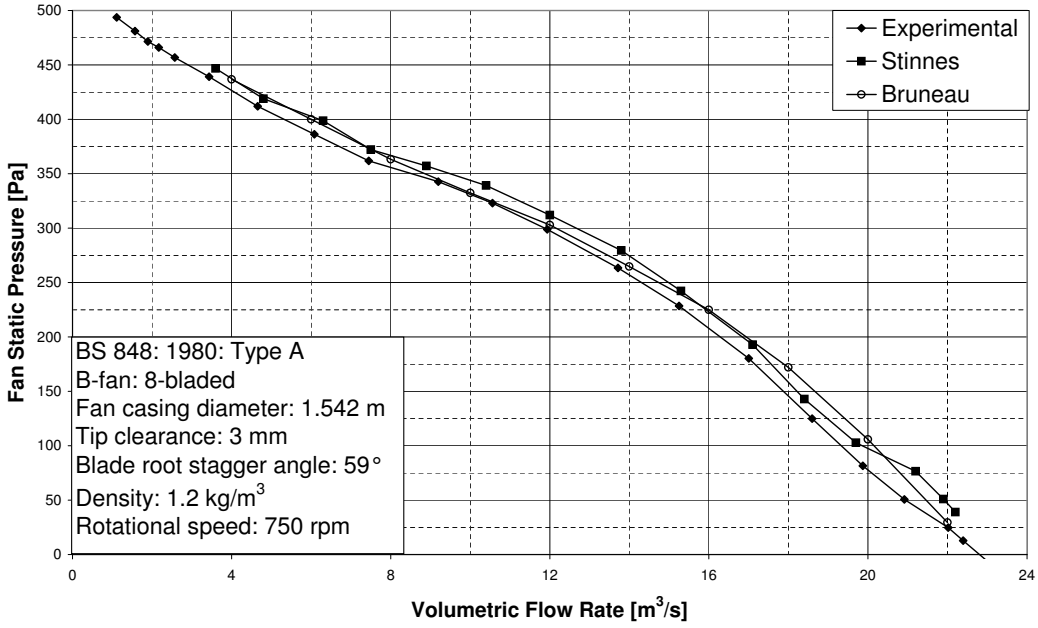

Figure F.4: Fan static pressure rise, comparison at 59°.

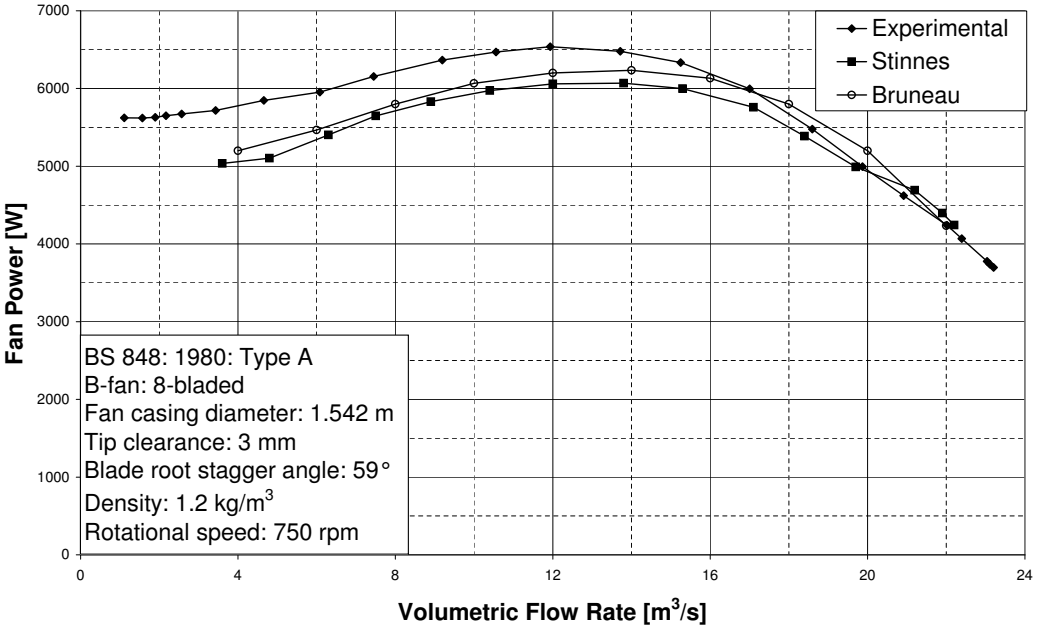

Figure F.5: Fan power, comparison at 59°.

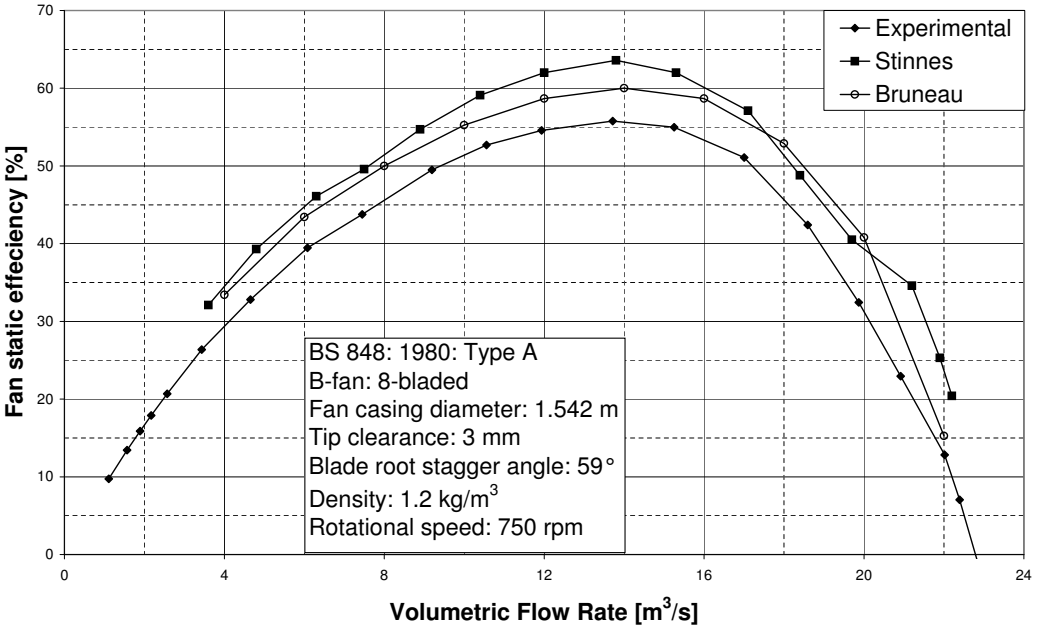

Figure F.6: Fan static efficiency, comparison at 59°.

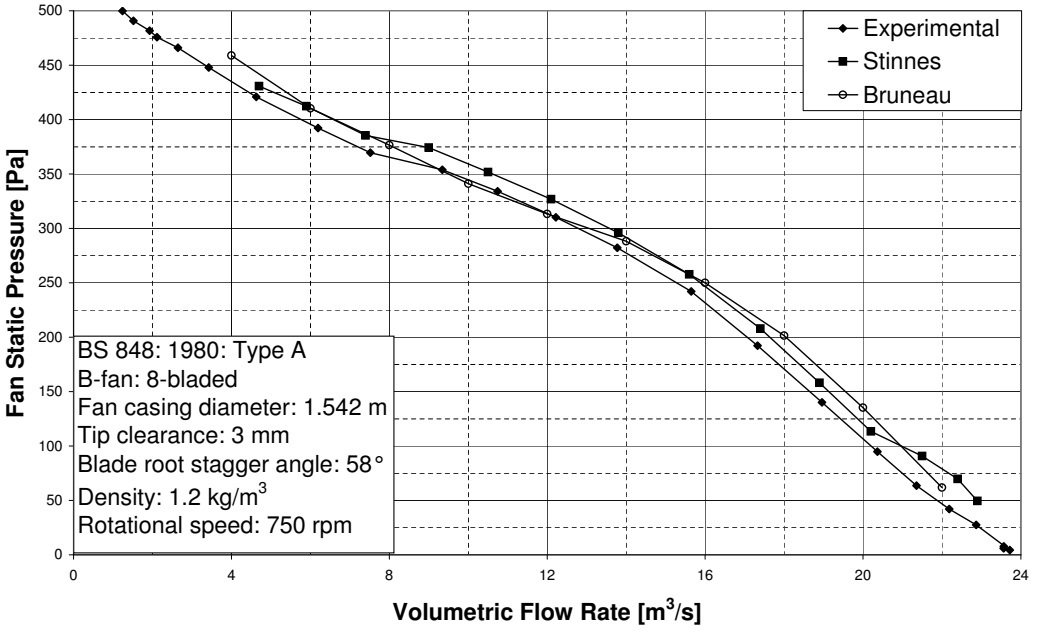

Figure F.7: Fan static pressure rise, comparison at 58°.

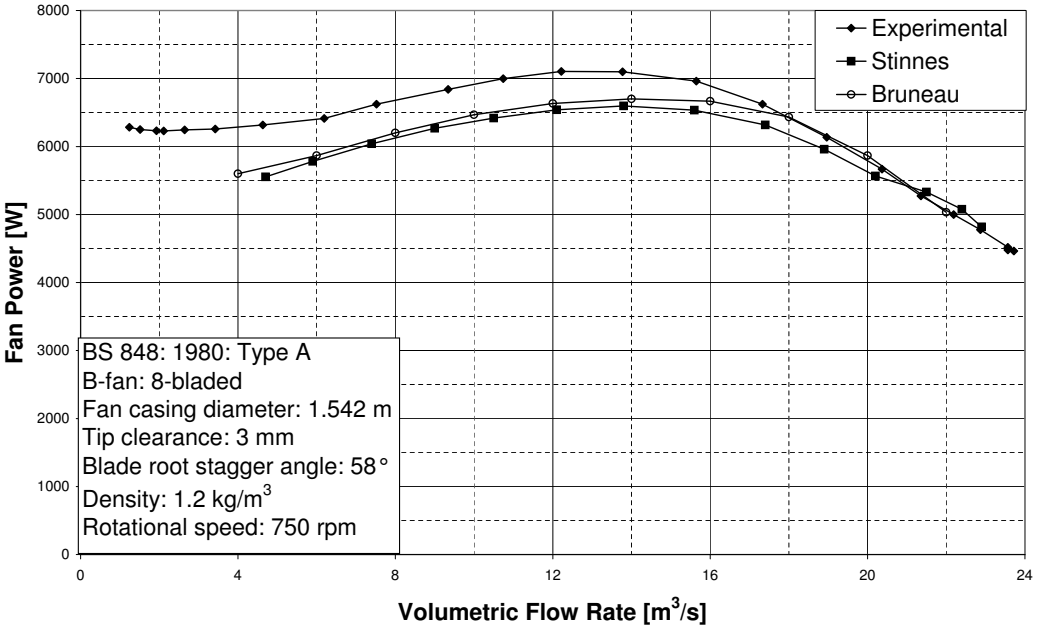

Figure F.8: Fan power, comparison at 58°.

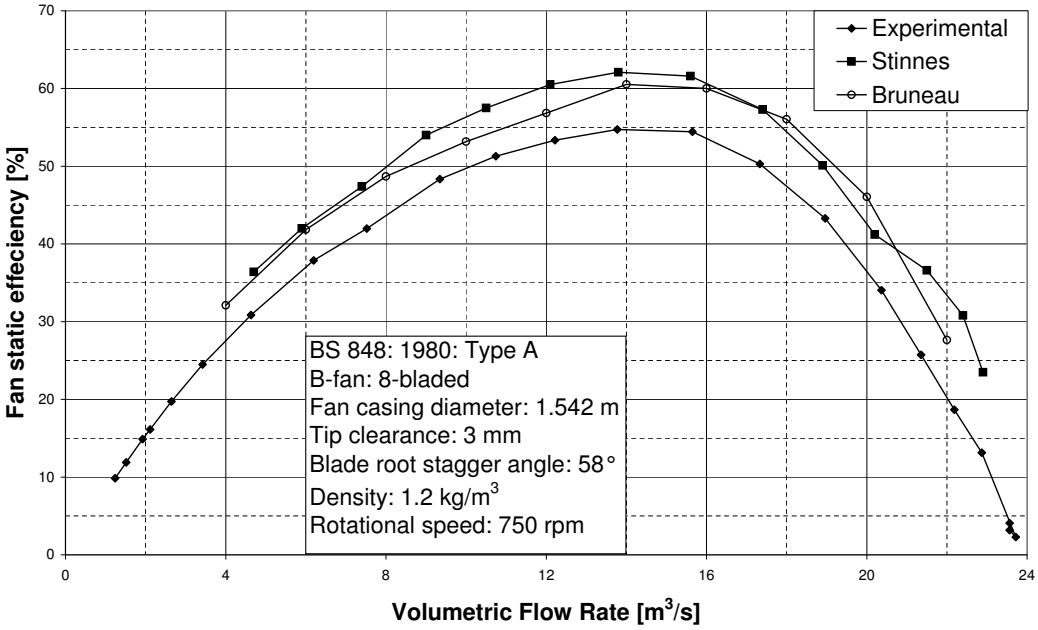

Figure F.9: Fan static efficiency, comparison at 58°.

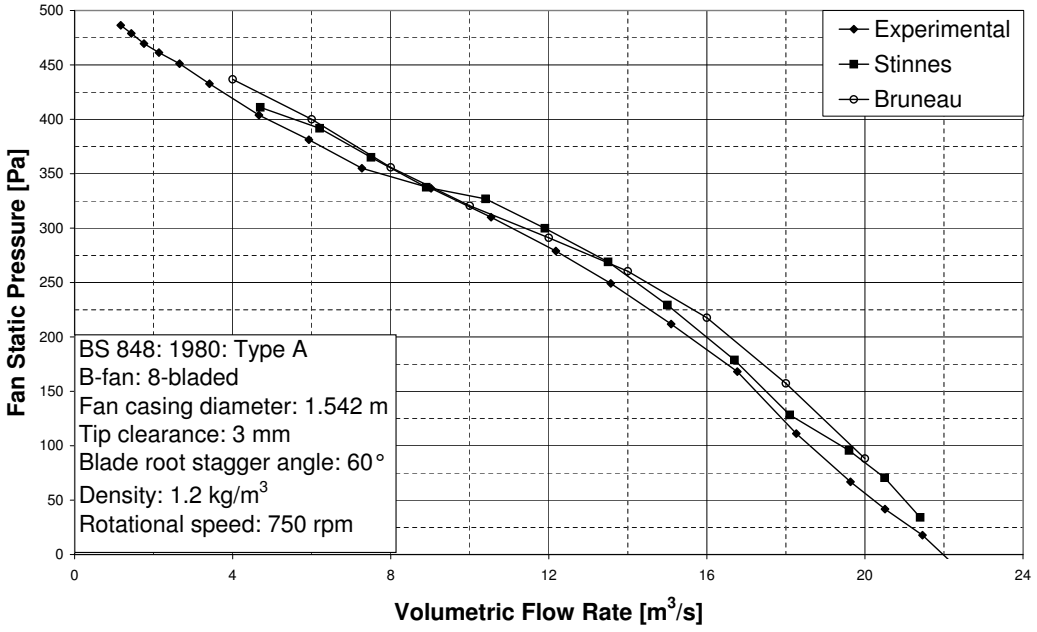

Figure F.10: Fan static pressure rise, comparison at 60°.

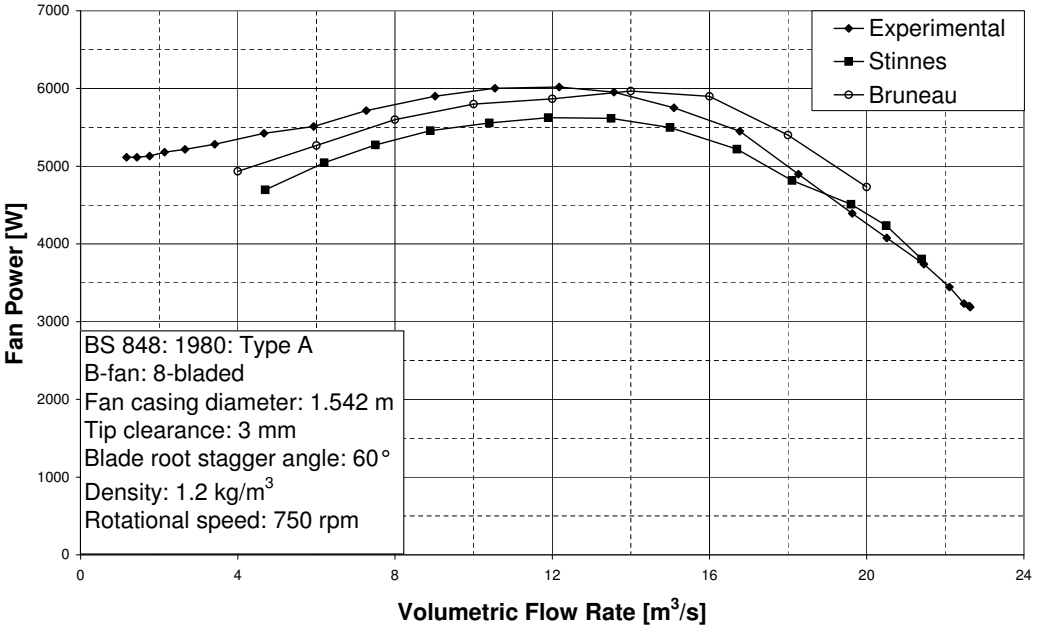

Figure F.11: Fan power, comparison at 60°.

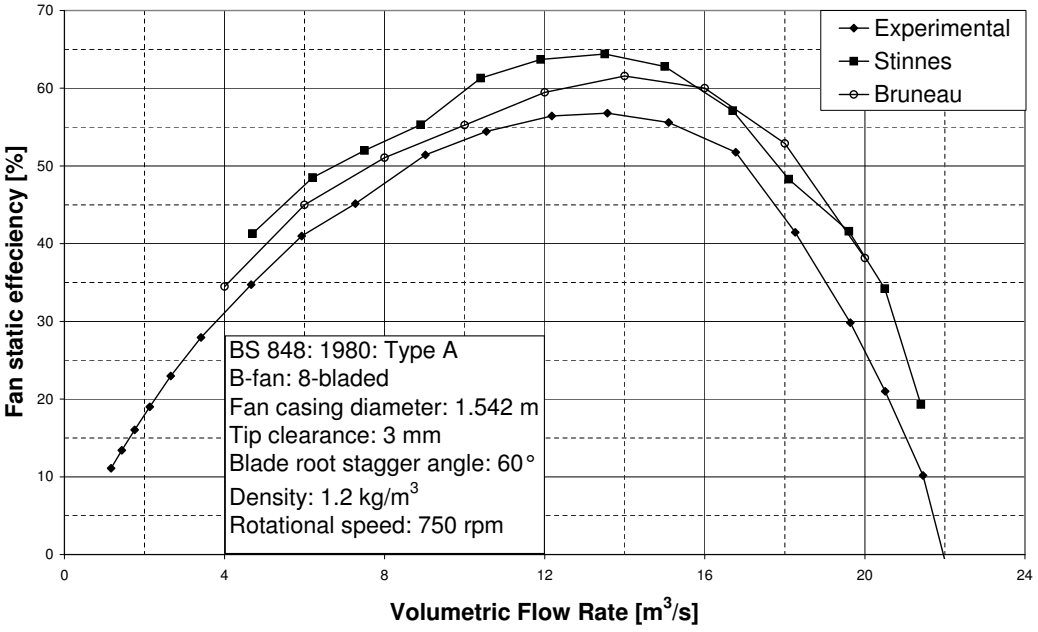

Figure F.12: Fan static efficiency, comparison at 60°.

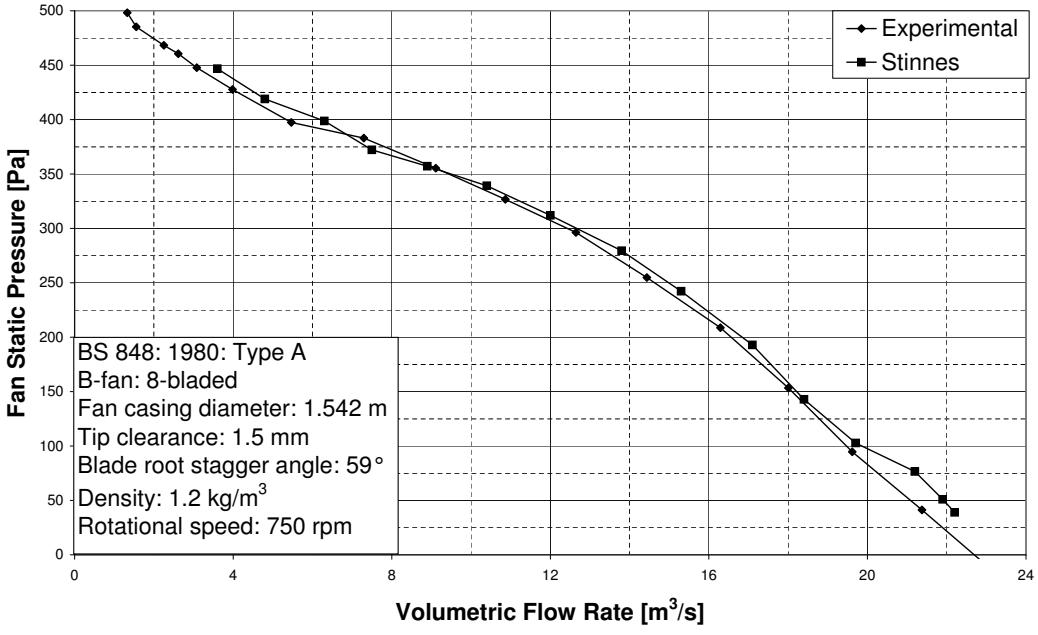

Figure F.13: Fan static pressure rise, comparison at 1.5 mm tip clearance.

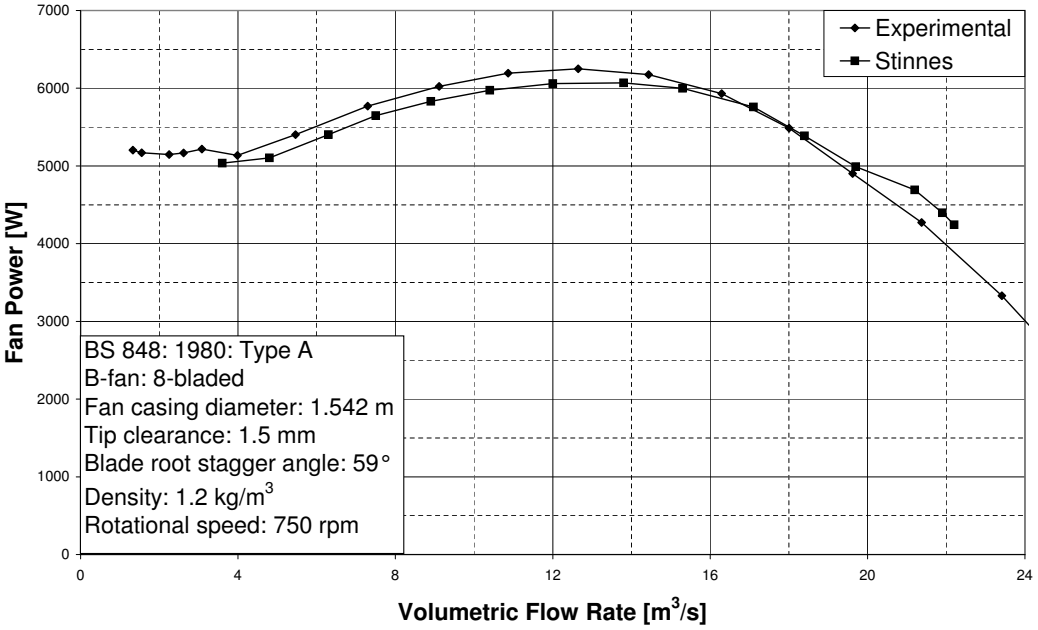

Figure F.14: Fan power, comparison at 1.5 mm tip clearance.

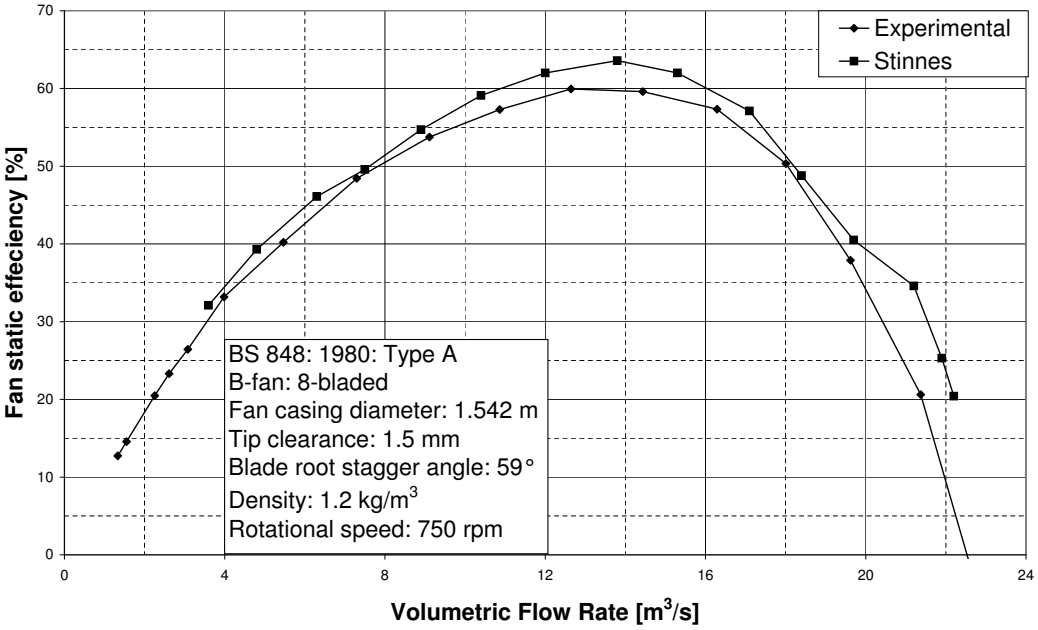

Figure F.15: Fan static efficiency, comparison at 1.5 mm tip clearance.

Appendix G

Numerical Simulation Data

The simulation data of the two CFD models are presented. The rotor-stator interface mentioned is only used to connect the blade section with the inlet- and outlet sections. All blocks are rotated as described in Section 3.4.3.

Table G.1: Numerical data for Approach-1

Stagger angle					59°
Tip clearance					3 mm
Fluid model					Perfect gas
rotor-stator interface					MPA
Outlet					Pinched
Velocity components solved in relative reference frame					Relative
Massflow rate	Static outlet	Total inlet	ΔP	Fan Power	Fan Static efficiency
[m^3/s]	[Pa]	[Pa]	[Pa]	[W]	[%]
2	101115	100585.42	529.580	4705.500	22.509
6	101102	100629.42	472.580	5458.400	51.947
10	101156	100767.71	388.290	6223.200	62.394
16	101228	101019.05	208.950	5751.400	58.128
20	101259	101186.11	72.890	4460.500	32.682

Table G.2: Numerical data for Approach-2

Stagger angle					59°
Tip clearance					3 mm
Fluid model					Perfect gas
rotor-stator interface					MPA
Outlet					Open
Velocity components solved in relative reference frame					Absolute
Massflow rate	Static outlet	Total inlet	ΔP	Fan Power	Fan Static efficiency
[m^3/s]	[Pa]	[Pa]	[Pa]	[W]	[%]
8	101325	101035.75	289.250	5128.400	45.121
10	101324.98	101018.32	306.660	5197.800	58.998
16	101324.96	101114.57	210.390	5472.600	61.511
20	101324.98	101261.71	63.270	4116.200	30.742

Appendix H

Streamline distribution diagrams

In this appendix the streamline distribution for the remaining flow rates are provided. This includes all operating points simulated for both Approach-1 and Approach-2.

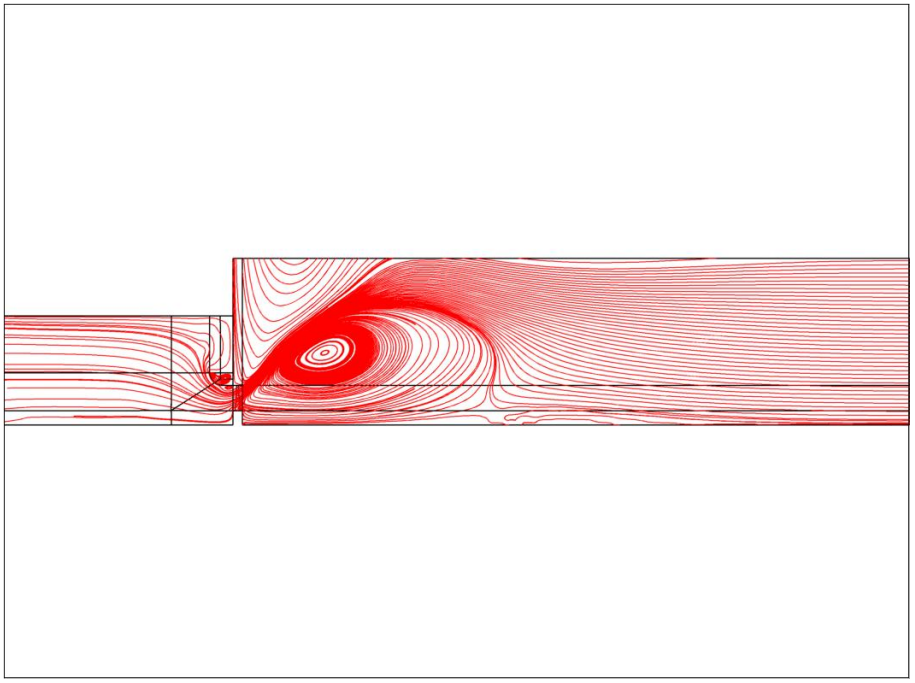

Figure H.1: Streamline distribution, $8\,\mathrm{m}^3/\mathrm{s}$, Approach-2.

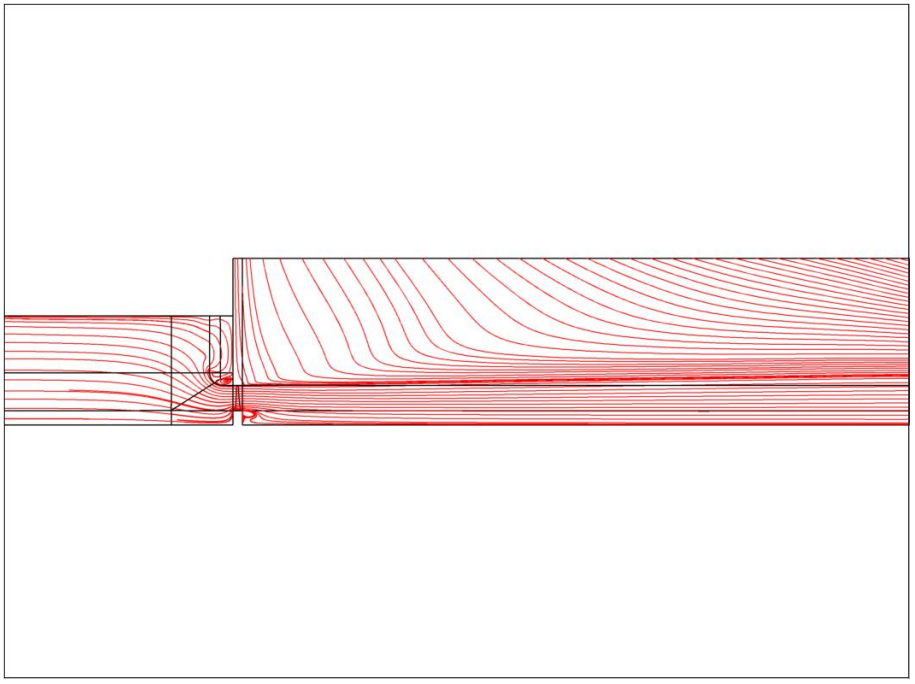

Figure H.2: Streamline distribution, 20 m^3/s, Approach-2.

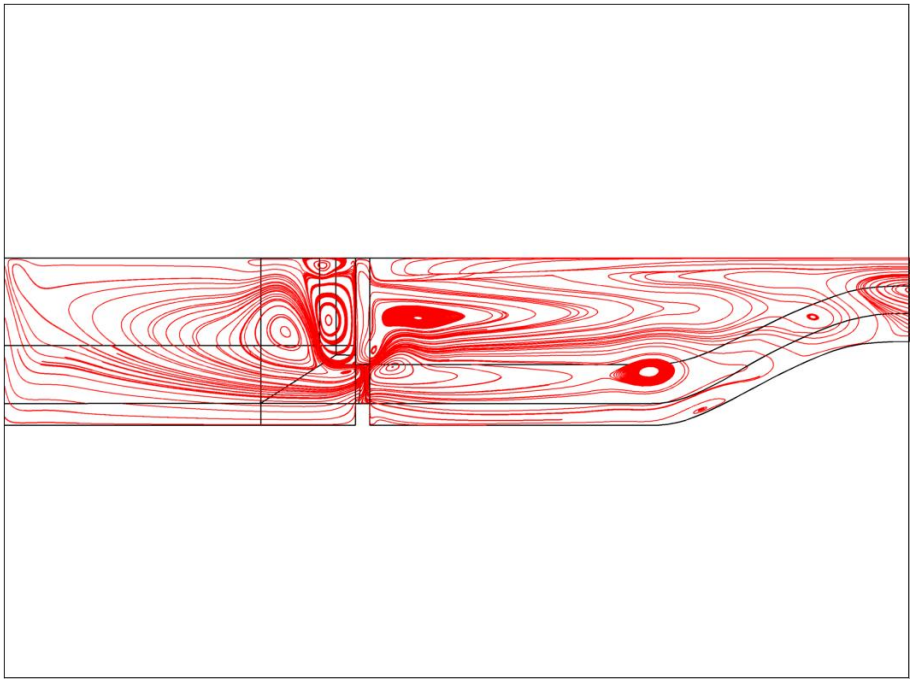

Figure H.3: Streamline distribution, 2 m^3/s, Approach-1, relative velocity solution.

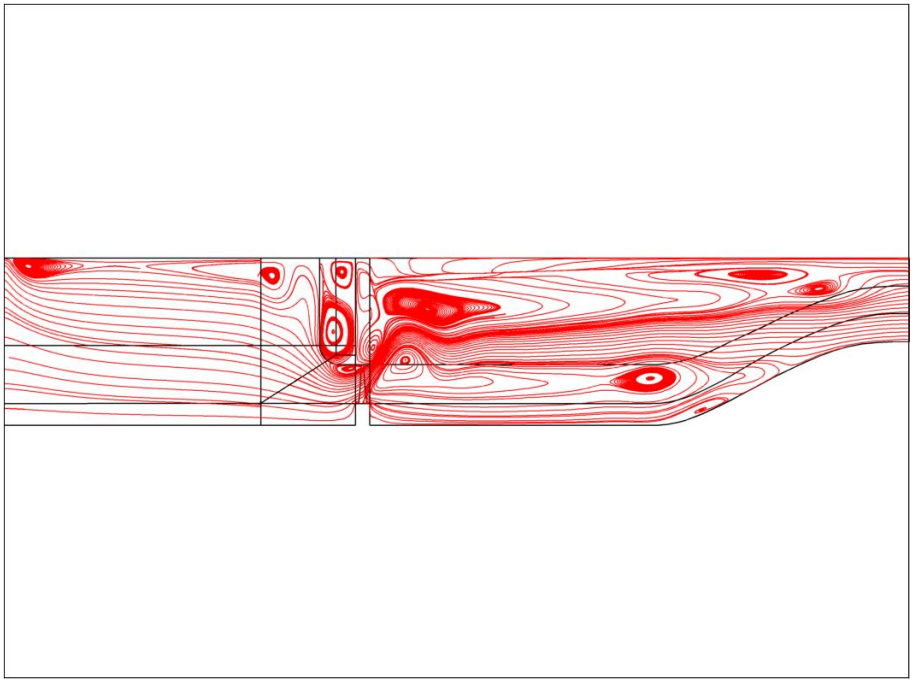

Figure H.4: Streamline distribution, $6\,m^3/s$, Approach-1, relative velocity solution.

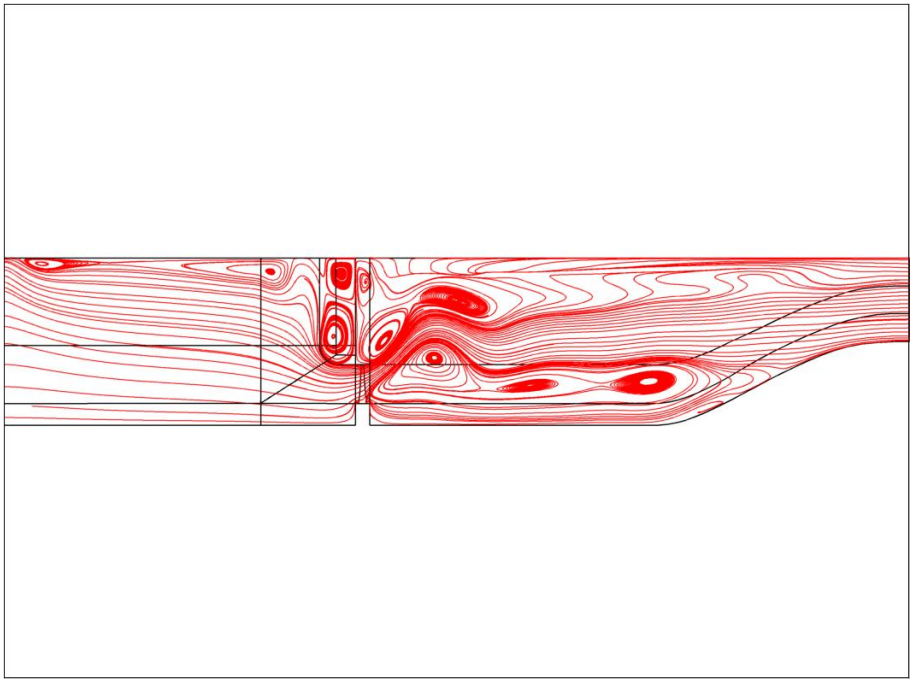

Figure H.5: Streamline distribution, $10\,m^3/s$, Approach-1, relative velocity solution.

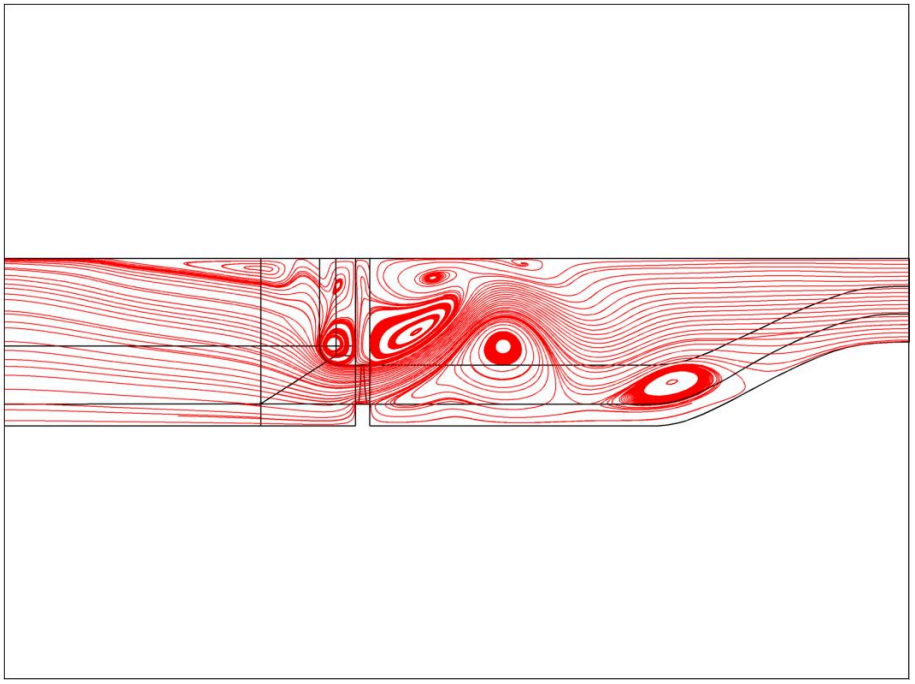

Figure H.6: Streamline distribution, $20\,m^3/s$, Approach-1, relative velocity solution.

List of References

Anderson, J. (1990). *Modern compressible flow: with historical perspective*. 2nd edn. McRaw-Hill, Inc.

Ashford, G. and Powell, K. (1996). An unstructured grid generation and adaptive solution technique for high-reynolds-number compressible flows. *27th Computational Fluid Dynamics*, vol. VKI LS 1996-06, pp. 1–84.

Bredell, J. (2005). *Numerical investigation of fan performance in a forced draft air-cooled steam condenser*. Master's thesis, Department of Mechanical Engineering, University of Stellenbosch.

Bruneau, P. (1994). *The design of a single rotor axial flow fan for a cooling tower application*. Master's thesis, Department of Mechanical Engineering, University of Stellenbosch.

Dippenaar, D. (2007). *Die sturkturele ontwerp en vervaardiging van 'n nuwe verwysingswaaier vir die groot waaier-toetstonnel*. Master's thesis, Department of Mechanical Engineering, University of Stellenbosch.

Esterhuyze, O. (2006). *The testing and evaluation of the performance of axial fans subjected to variable inlet conditions*. Master's thesis, Department of Mechanical Engineering, University of Stellenbosch.

Kelecy, F. (2000). Study demonstrates that simulation can accurately predict fan performance. *Journal Articles by Fluent Sofware Users*, vol. JA108, pp. 1–4.

Kröger, D. (1998). *Air-cooled heat exchangers and cooling towers Thermal-flow performance evaluation and design*. Department of Mechanical Engineering University of Stellenbosch.

Lötstedt, P. (1992). Propeller slip-stream model in subsonic linearized potential flow. *Journal of Aircraft*, vol. 29 (6), pp. 1098–1105.

Lötstedt, P. (1995). Accuracy of a propeller model in inviscid flow. *Journal of Aircraft*, vol. 32(6), pp. 1312–1321.

McGhee, R., Beasley, W. and Somers, D. (1977). Low-speed aerodynamic characteristics of a 13-percent-thick airfoil section. *NASA Technical Memorandum*, vol. NASA TM X-72679.

McGhee, R., Beasley, W. and Whitcomb, R. (1979). Nasa low- and medium-speed airfoil development. *NASA Technical Memorandu*, vol. NASA-TM-78709.

Meyer, C. (1996). *Plenum losses in forced draught air-cooled heat exchangers.* Master's thesis, Department of Mechanical Engineering, University of Stellenbosch.

Meyer, C. (2000). *A numerical investigation of the plenum chamber aerodynamic behaviour of mechanical draught air-cooled heat exchangers.* Ph.D. thesis, Department of Mechanical Engineering, University of Stellenbosch.

Ohad, G. and Aviv, R. (2005). Propeller performance at low advance ratio. *Journal of aircraft*, vol. 42-2.

Pelletier, D., Garon, A. and Camarero, R. (1991). Finite element method for computing turbulent propeller flow. *AIAA Journal*, vol. 29(1), pp. 68–75.

Pelletier, D. and Schetz, J. (1986). Finite element navier-stokes calculation of three-dimensional turbulent flow near a propeller. *AIAA Journal*, vol. 24(9), pp. 1409–1416.

Pericleous, K. and Patel, M. (1986). The modelling of tangential and axial agitators in chemical reactors. *PhysicoChemical Hydrodynamics*, vol. 8(2), pp. 105–123.

Ramasubramanian, M., Shiffler, D. and Jayachandran, A. (2008). A computational fluid dynamics modeling and experimental study of the mixing process for the dispersion of the synthetic fibers in wet-lay forming. *Journal of Engineered Fibers and Fabrics*, vol. 3, Issue 1.

Schetz, J., Pelletier, D. and Mallory, D. (1988). Experimental and numerical investigation of a propeller with three-dimensional inflow. *Journal of Propulsion*, vol. 4(4), pp. 341–349.

Sezer-Uzol, N. and Long, L. (2006). 3d time-accurate cfd simulations of wind turbine rotor flow fields. *AIAA 2006-0394*.

Spalart, P. and Allmaras, S. (1994). A one-equation turbulence model for aerodynamic flows. *La Recherche Aérospace*, vol. 1, pp. 5–21.

Stinnes, W. (1998). *The performance of axial fans subjected to forced cross-flow at Inlet.* Master's thesis, Department of Mechanical Engineering, University of Stellenbosch.

Thiart, G. and von Backström, T. (1993). Numerical simulation of the flow field near an axial flow fan operating under distorted inflow conditions. *Journal of Wind Engineering and Industrial Aerodynamics*, vol. 45, pp. 189–214.

Turkel, E., Radespiel, R. and Kroll, N. (1997). Assessment of preconditioning methods for mutidimensional aerodynamics. *Computers and Fluids*, vol. 26, No. 6, pp. 613–634.

Unknown Author (1980). *BS 848: Part 1: 1980, Fans for General Puposes, Part 1: Methods for testing performance.* British Standards Institution.

Unknown Author (2000). *The basics of axial flow fans.* Hudson Products Corporation.

Unknown Author (2007*a*). *User Manual AutoGrid™ v8.* NUMECA International, 5, Avenue Franklin Roosevelt 1050 Brussels Belgium.

Unknown Author (2007*b*). *User Manual FINE™/Turbo v8 (including Euranus).* NUMECA International, 5, Avenue Franklin Roosevelt 1050 Brussels Belgium.

Unknown Author (2007*c*). *User Manual IGG™ v8.* NUMECA International, 5, Avenue Franklin Roosevelt 1050 Brussels Belgium.

Van der Spuy, S., Von Backström, T. and Kröger, D. (2009). An evaluation of simplified methods for modelling the performance of axial flow fan arrays. *Unpublished Journal.*

Van Staden, M. (1996). Integrated approach to cfd modelling of air-cooled condensers. In: *1st South African Conference on Applied Mechanics (SACAM).*

Venter, S. (1990). *The effectiveness of axial flow fans in A-frame plenums.* Ph.D. thesis, Department of Mechanical Engineering, University of Stellenbosch.

Venter, S. and Kröger, D. (1992). The effect of tip clearance on the performance of an axial flow fan. *Energy Convers. Mgmt.*

Vigneron, D., Vaassen, J. and Essers, J. (2008). An implicit finite volume method for the solution of 3d low mach. *Journal of Computational and Applied Mathematics*, vol. 215 (2008), pp. 610–617.

White, F. (2006). *Viscous Fluid Flow.* McRaw-Hill, Inc.

Zhonghua, H. and, F.H., Wenping, S. and Zhide, Q. (2007). A preconditioned multigrid method for efficient simulation of three-dimensional compressible and incompressible flows. *Chinese Journal of Aeronautics*, vol. 20(2007), pp. 289–296.